

REPORT R-1721

ANTITANK WEAPON SYSTEM APPLICATION  
OF  
IMPULSE CONTROL AND SEMIACTIVE HOMING

AMCMS Code 5520.11.434

Prepared by:

*R E Donnard*

R. E. DONNARD  
Mechanical Engineer

*S J Fenton*

S. J. FENTON  
Staff Engineer  
Technical Analysis Group, Inc.\*

*A P Stoliar*

A. P. STOLIAR  
Staff Engineer  
Technical Analysis Group, Inc.\*

Reviewed by:

*H P Manning*

H. P. MANNING  
Associate Director  
Research and Development Group

Approved by:

*C C Fawcett*

C. C. FAWCETT  
Technical Director  
Research and Development Group

R. E. BASSLER, Jr.  
Lt Colonel, Ordnance Corps  
Chief  
Research and Development Group

for

GEORGE H. PIERRE, Jr.  
Colonel, Ordnance Corps  
Commanding

Research and Development Group, Frankford Arsenal  
Philadelphia, Pa.  
April 1964

## A B S T R A C T

A supporting research program was initiated at Frankford Arsenal to examine a weapon system concept, known as POLCAT, which utilizes semi-active homing and terminal projectile control. The ultimate objective of this work was to demonstrate the functional feasibility of the POLCAT system by firing projectiles from a gun and correcting their trajectories into an illuminated target by operation of projectile guidance and control elements.

This information serves to support current work being conducted by Frankford Arsenal in the development of weapon systems which utilize semi-active homing and terminal projectile control.

## TABLE OF CONTENTS

	Page
<b>1.0 <u>INTRODUCTION</u></b>	1
1.1 PROGRAM OBJECTIVE	2
1.2 SCOPE OF REPORT	3
1.3 SUMMARY	4
<b>2.0 <u>SYSTEM CONCEPT</u></b>	7
2.1 FUNCTIONAL DESCRIPTION	8
2.2 ELEMENTS OF POLCAT SYSTEM	9
<b>3.0 <u>SYSTEM DESIGN</u></b>	15
3.1 AERODYNAMICS	16
3.1.1. <u>Aerodynamic Design</u>	16
3.1.1.1 Drag	20
3.1.1.2 Normal Force and Pitching Moment	22
3.1.1.3 Roll Damping and Effectiveness	23
3.1.2 <u>Aerodynamic Test</u>	25
3.1.2.1 Description of Wind Tunnel Tests	25
3.1.2.2 Test Results	26
3.1.3 <u>Aerodynamic Performance</u>	28
3.1.3.1 Trajectory Characteristics	29
3.1.3.2 Yaw Characteristics	31
3.1.3.3 Roll Characteristics	32
3.1.4 <u>Summary</u>	33
3.2 STRUCTURES	36
3.2.1 <u>Structural Design</u>	36
3.2.1.1 Stress Analysis	38
3.2.1.2 Load Analysis	60
3.2.2 <u>Structural Test</u>	62
3.2.2.1 Air Gun Tests	62
3.2.2.2 Static Impulse Test	64
3.2.3 <u>Summary</u>	64

## TABLE OF CONTENTS

	Page
<b>3.3 CONTROL</b>	<b>71</b>
<b>3.3.1 Design</b>	<b>71</b>
3.3.1.1 Interior Ballistics Analysis	72
3.3.1.2 Control Effectiveness Analysis	79
3.3.1.3 Control Error	83
3.3.1.4 Test Fixture Design	84
3.3.1.5 Prototype Pulser	85
<b>3.3.2 Test</b>	<b>85</b>
3.3.2.1 Test Fixture Firings	87
3.3.2.2 Pulser Qualification Firings	87
<b>3.3.3 Summary</b>	<b>90</b>
 <b>3.4 GUIDANCE</b>	 <b>103</b>
<b>3.4.1 Guidance Analysis</b>	<b>107</b>
3.4.1.1 Probabilistic Criteria	109
3.4.1.2 POLCAT Detection Criteria	112
<b>3.4.2 Noise Analysis</b>	<b>117</b>
3.4.2.1 Photon Noise	117
3.4.2.2 Semiconductor Noise	119
3.4.2.3 Atmospheric Scintillation	121
3.4.2.4 Scanning Noise	122
3.4.2.5 Noise Evaluation	124
<b>3.4.3 Signal Analysis</b>	<b>126</b>
3.4.3.1 Illuminator	127
3.4.3.2 Atmospheric Attenuation	129
3.4.3.3 Target Reflectivity	131
3.4.3.4 Target Signal	132
<b>3.4.4 Seeker Design</b>	<b>134</b>
3.4.4.1 Optics and Detector	134
3.4.4.2 Electronic Processing System	137
3.4.4.3 Amplifier	139
3.4.4.4 Trigger Circuit	141
3.4.4.5 Power Supply	144
3.4.4.6 Seeker Functional Tests	144
<b>3.4.5 Seeker Field Tests</b>	<b>146</b>
3.4.5.1 Instrumentation	146
3.4.5.2 Test Results	147
<b>3.4.6 Summary</b>	<b>150</b>
 <b>4.0 CONCLUSIONS AND RECOMMENDATIONS</b>	 <b>182</b>



## LIST OF FIGURES

Figure No.	Title	Page
2.1-1	Illustration of POLCAT Concept	12
2.1-2	POLCAT Steering Law	13
2.1-3	Effect of Probability of Hit	14
3.1-1	POLCAT Test Projectile	35
3.1-2	Drag Coefficient vs. Mach Number	36
3.1-3	Normal Force and Pitching Moment Slope vs. Mach Number	37
3.1-4	Damping and Rolling Moment Derivatives vs. Mach Number	38
3.1-5	Comparison of Estimated Drag Coefficient with Test Data	39
3.1-6	Normal Force and Lift Curve Slope Coefficients vs. Mach Number	40
3.1-7	Comparison of Estimated Pitching Moment Slope Coefficient with Test Data	41
3.1-8	Effect of Nose Cant Angle on Trim Angle of Yaw	42
3.1-9	Damping-in-Roll and Rolling Effectiveness Coefficients vs. Mach Number	43
3.1-10	Velocity Variation vs. Range for POLCAT Test Projectile	44
3.1-11	Time of Flight vs. Range for POLCAT Test Projectile	45
3.1-12	Effect of Muzzle Velocity on Velocity Decay	46
3.1-13	Effect of Muzzle Velocity on Time of Flight	47
3.1-14	Steady State Yaw Due to Crosswind Velocity	48
3.1-15	Damping in Yaw	49
3.1-16	Effect of Fin Cant on Roll Rate Variation	50
3.1-17	Comparative Rolling Effectiveness Fin Cant vs. Leading Edge Bevel	51
3.1-18	Projectile Velocity at 1000 Meters Range	52
3.2-1	Assembly Drawing of Test Projectile	65
3.2-2	Model for Elastic Analysis	66
3.2-3	Estimated Tail Inertia Load vs. Time	67
3.2-4	Estimated Tail Deflection vs. Time	68
3.2-5	Comparison of Elastic and Rigid Body Response	69
3.2-6	Assembly Drawing of Seeker Head	70
3.3-1	Control Effectiveness Ratio	93
3.3-2	Miss Distance Due to Angular Control Error	94
3.3-3	Test Fixture No. 1	95
3.3-4	Test Fixture No. 1 (Exploded View)	96
3.3-5	Test Fixture No. 2	97
3.3-6	Test Fixture No. 2 (Exploded View)	98

# LIST OF FIGURES (cont'd)

3.3-7	Test Projectile with Pulser	99
3.3-8	Empirical Relationship for Pulser Design	100
3.3-9	Test Projectile after Firing	101
3.4-3	SNR as a Function of False Alarm Rate	151
3.4-4	Spectrum of Noise Current in Semiconductor	152
3.4-5	Empirical Frequency Spectrum of Light Intensity Fluctuation for Different Wind Velocities	153
3.4-6	Empirical Dependence of Amount of Twinkle on Diameter of Telescope Diaphragm	153
3.4-7	Typical Background Terrain	154
3.4-8	Terrain Background Spectral Density Function	155
3.4-9	Spectral Sterance of Xenon ArcLamp	156
3.4-10	POLCAT Illuminator	157
3.4-11	Precipitable Water Vapor per foot of Path Length	158
3.4-12	Measured Atmospheric Transmission	159
3.4-13	Reflected Power from a Tank	160
3.4-14	Power Incident on POLCAT Seeker vs. Target Distance	161
3.4-15	POLCAT Seeker	162
3.4-16	Seeker Lens	163
3.4-17	Optic-Detector Arrangement	164
3.4-18	Seeker Block Diagram	165
3.4-19	Spectral Density Function of POLCAT Signal	166
3.4-20	Peak SNR for Various Filters	167
3.4-21	Amplifier Schematic	168
3.4-22	Trigger Circuit Schematic	169
3.4-23	POLCAT Seeker Head No. 1 Response	170
3.4-24	POLCAT Seeker Head No. 4 Response	171
3.4-25	Frequency Response for POLCAT Seeker	172
3.4-26	Squib Voltage vs. Time after Signal Pulse	173
3.4-27	Instantaneous Field of View-horizontal	174
3.4-28	Instantaneous Field of View-vertical	175
3.4-29	Scanner Field of View	176
3.4-30	Typical Output Signals	177
3.4-31	Amplifier Output Signal as LOS Scans Target	178
3.4-32	LOS Angle for Firing Signal vs. Offset Angle	179

## 1.0 INTRODUCTION

In December 1960, a program was initiated at Frankford Arsenal with the purpose of demonstrating the functional performance of a weapon system concept known as POLCAT. Since this program was undertaken as a consequence of prior supporting research activities, a summary of the early POLCAT work is presented.

The POLCAT concept was originated during a study (1) that investigated the feasibility of applying post firing correction techniques to a projectile in order to increase the long range accuracy of recoilless anti-tank weapons. The application of POLCAT proposed that targets be illuminated semi-actively to establish a homing link, and that the projectile incorporate a frame fixed target seeker for guidance and impulse steering for control. The results of the initial feasibility study were deemed to be sufficiently promising such that a series of supporting research efforts were conducted to examine methods for implementing the POLCAT concept.

Analyses and tests (2) (3) established that impulse control offered an effective technique for increasing the accuracy of gun systems (provided the homing link functioned as intended) and could be developed as a practical and a reliable means for correcting projectile flight path. Studies and field tests (4) (5) were conducted to determine the requirements for target seeker design and the effects of the tactical environment on guidance performance. Further, studies (6) were made considering the application of the POLCAT concept to other weapon system requirements.

While the technical objectives of this work were limited, the nature of the results served to enhance the interest in the possible application of POLCAT to the requirements of the Infantry Heavy Assault Weapon - Long Range. It was recognized, however, that the critical questions of system feasibility remained and that a conclusive demonstration of system performance was required before a POLCAT weapon development program could be seriously considered. Accordingly, the supporting research program described in this report was initiated by Frankford Arsenal.

#### 1.1 PROGRAM OBJECTIVE

The aim of the program was to demonstrate the functional performance of the POLCAT concept by conducting a series of range firings with a POLCAT "demonstration" system. The flight test plan prescribed that a projectile be fired from a gun and its trajectory, then, be corrected into an illuminated area of a target by the integral operation of the projectile guidance and control elements. While it was not required that the firings be conducted under quasi-combat conditions or that the test projectile incorporate a warhead, the task of developing a POLCAT demonstration system was a formidable one. No flight hardware suited to the requirements of the contemplated test program had been developed by past supporting research efforts. Further, a complete understanding of the phenomena which were to significantly affect homing link design was lacking. As a consequence, the supporting research program was directed toward the generation of basic design and experimental data as well as the development of flight hardware for the demonstration.

## 1.2 SCOPE OF REPORT

The material presented herein summarizes the analyses, design studies, and tests of the POLCAT supporting research program that was conducted in the period of December 1960 to October 1962. In order to provide a more complete treatment of semi-active homing, as utilized in the POLCAT concept, these data were augmented by additional analyses and design studies that were performed during the preparation of this report.

The following section, 1.3 Summary, outlines the major achievements of the supporting research program.

Section 2.0, System Concept, describes the general operational and functional characteristics of the POLCAT concept. This section was prepared, specifically, for those readers who have had no previous exposure to POLCAT.

A complete design description and analysis of the POLCAT demonstration system is given in Section 3.0.

Based on what had been accomplished in the supporting research program, the status of the POLCAT technology is evaluated in Section 4.0.

Finally, a companion report "Design Data Supplement - POLCAT Supporting Research (Dec. 1960 - Oct. 1962)" has been prepared containing those data considered significant, but too detailed to include in this report. The Design Data Supplement contains detail design drawings, test equipment design specifications, and component test and inspection procedures.

Reports by the following organizations provided the primary data sources for this report:

Arthur D. Little, Inc. (under contract to Frankford Arsenal)

Ballistics Research Laboratories, APG

Bulova Research and Development Laboratories, Inc. (under contract to Frankford Arsenal and BRL)

Frankford Arsenal

This report and supplement were prepared by Technical Analysis Group, Inc., under Contract No. DA-36-038-AMC-969(A), in conjunction with Frankford Arsenal.

### 1.3 SUMMARY

The primary objective of the POLCAT supporting research program (December 1960 - October 1962) was not attained. The inability to demonstrate POLCAT functional performance was due to budgetary limitations rather than technical difficulties. However, a useful and substantial body of design and test data were generated. These data include (a) Aerodynamic and structural design characteristics of a 120mm test projectile, (b) design and performance characteristics of a control unit (pulser) capable of delivering an impulse of 20 lb-sec, (c) design and performance characteristics of a target seeker capable of operating after being subjected to an acceleration of 10,000 g's and (d) measurements of target reflectivity. These results have greater significance at the present time than when the program was curtailed. With the development of laser technology and the proposed development of a laser illuminator, the application of semi-active homing is once again being evaluated by

Frankford Arsenal in the LASH program. Since the LASH system concept is similar to the POLCAT concept, the ultimate significance of the POLCAT supporting research program will be determined by its usefulness to the current LASH effort.

## References

- (1) Fenton, S. J., "Feasibility Study of An Advanced Recoilless Rifle Weapon System Utilizing a Terminally-Guided Projectile," Report No. R-1425, Frankford Arsenal, Pa., December 1957. CONFIDENTIAL
- (2) Goulet, B. N., "A Preliminary Evaluation of the Delivery Accuracy of a Single-Impulse Correction Concept for Anti-tank Weapon Systems,"
- (3) Fulton, C. L., "A Reaction Thrust Generator for Projectile Guidance and Possible Missile Guidance," Memorandum Report MR-689, Frankford Arsenal, Pa., October 1958. CONFIDENTIAL
- (4) Lubin, A., "Feasibility Study: Quasi-Passive Post-Launch Fire Control Technique -- Final Report," Contract DA-30-069-ORD-2196, Bulova Research and Development Laboratories, N. Y., 15 October 1958. SECRET.
- (5) Fenton, S. J. and Stcliar, A. P., "POLCAT Guidance System," Proceedings of the Infrared Information Symposium, Vol. 7, No. 1 CONFIDENTIAL
- (6) "Feasibility Study of a Combat Vehicle Weapon System, Final Report, Part II," Contract DA-30-069-ORD-2342, Report No. C-101, Bulova Research and Development Laboratories, N. Y., 15 November 1959. CONFIDENTIAL.



## 2.0 System Concept

The POLCAT concept was conceived, and its application as an infantry antitank system evaluated, during a period when the efforts to increase the long range hitting capability of these weapons were limited to two basic developmental approaches: increasing the fire control accuracy and muzzle velocity of gun systems; and the development of command, wire guided missiles. The increased effectiveness of gun systems was accompanied by an increase in system weight and was limited in nature, since the random errors of projectile flight remain. The limitation precludes the fulfillment of high first round probability of hit requirements at long range by conventional gun systems.

While the command guided missile system offers a direct solution to the problem of accuracy at long range, it has also presented the problems of increased weapon cost and complexity.

Conceptually, all command guidance techniques possess two undesirable characteristics: 1) accuracy decreases with range, and 2) the need to relate the earth referenced coordinate system of the command transmitter to the missile referenced coordinate system of the receiver. The basic simplicity of the POLCAT concept can be attributed to the use of semi-active homing for guidance.

POLCAT utilizes a terminal correction concept that combines the capabilities of predicted fire control and self-contained projectile guidance and control.

Within this concept, the primary function of predicted fire control is to establish relatively accurate projectile trajectories. While this accuracy

is insufficient to obtain the desired hit probability at long range, it does restrict projectile miss distance enough to permit the use of simple, almost crude guidance and control components to effect terminal correction of the projectile flight path. A significant aspect of the POLCAT concept is that it is possible to apply it to all gun systems that rely on predicted fire in defeating tank type targets. The following discussions present the functional characteristics of the POLCAT concept (Section 2.1) and a definition of the basic elements that constitute a generalized POLCAT system (Section 2.2).

## 2.1 Functional Description

The terminal correction to projectile flight path is achieved by a frame fixed target seeker for guidance and a single impulse for trajectory control. Projectile spin is induced at launch, and maintained during flight. Since the target seeker is fixed to the projectile, the scanning function of the seeker is generated by offsetting its instantaneous field of view from the axis of the spinning projectile. See figure 2.1-1.

Operating as an angle measuring device, the seeker is required to determine when the angle, between the projectile longitudinal axis and the LOS (line of sight) to the target, has reached a magnitude that indicates an impending miss. This situation occurs downrange, relatively close to the target, where the LOS angle diverges rapidly if the projectile is destined to miss the target. An illustration of the variation of LOS angle for hit and miss trajectories is given in figure 2.1-2. By selecting a specific LOS angle for trajectory correction, the steering law of the projectile guidance and control system is established. If this pre-selected angle is not generated during flight, a hit on the target occurs. The guidance and

control system will function only if the projectile is destined to miss the target.

2). If the projectile is destined to miss the target, the IOC angle will increase, and at some point along the trajectory it will equal the pre-selected scan angle of the seeker. At that point the seeker senses the illuminated target in its field of view and initiates the impulse control unit (pulser). The pulser has a fixed orientation relative to the seeker, so designed, that on receiving a fire signal from the seeker, it delivers a single impulse in the desired direction, to correct projectile flight toward the target. The pulser generates a force that is impulsive in nature so that the projectile flight path change is achieved, for all practical purposes, instantaneously.

The basic function of the POLCAT guidance and control system is to convert an impending miss on a target to a hit. Thus, the effective improvement in hit probability of the weapon system is obtained by increasing its probability of hit at the longer ranges as shown in figure 2.1-3. At shorter range, where a gun with its predicted fire control system can hit a target, the frequency at which POLCAT guidance and control system will be required to function is low. This is a significant advantage of the POLCAT concept since a malfunction of the guidance and control system does not represent the loss of a round but rather the reduction in probability of hit to that of the basic gun-system.

## 2.2 ELEMENTS OF POLCAT SYSTEM

The basic elements of the POLCAT system are: the gun, the fire control system, the target illuminator, and the projectile incorporating the required

guidance and control components for terminal trajectory correction.

The gun need not be defined because its use in the POLCAT application does not require any modification in design, performance and/or use, provided the gun diameter be at least 105 mm. While the previous work has been primarily concerned with the use of recoilless rifles, the POLCAT concept can utilize closed breech guns with equal effectiveness.

Similarly, the fire control system need not be defined. Previous POLCAT systems analyses have considered the use of sub-caliber spotter rifles and conventional tank optical fire control systems. It was shown, however, that the ability of a POLCAT system to maintain high hit probability at extended ranges is dependent upon the accuracy performance of the basic gun-fire control combination.

The target illuminator irradiates the target with a narrow, modulated beam such that the reflected energy from the target is of sufficient intensity and discrete character that a reliable guidance signal is established for the projectile seeker. Previous applications of the POLCAT semi-active homing technique utilized are discharge lamps as an illuminator source. Since then, the laser illuminator has been considered to be the most practical means for generating a homing link. The narrow band spectral radiation of laser illuminators is the characteristic from which improvement in homing link performance is derived.

The POLCAT projectile is fin stabilized, relying on gun rifling to generate an initial roll rate. A near constant roll rate is maintained throughout flight by beveling or canting the projectile tail fins.

The seeker optics, detector, and electronics are located in the pro-

jectile nose. The instantaneous field of view of seeker is offset from the projectile longitudinal axis thereby establishing an annular scan pattern as the projectile spins.

The pulser is incorporated within the projectile so that its thrust axis passes through the center of gravity and normal to longitudinal axis of the projectile. The impulse required for control is generated by the burning propellant in the pulser chamber. The burning and discharge of the propellant occurs in a sufficiently short time period so that impulsive force is delivered to the projectile inducing instantaneous flight path change.

From this general description, the report now proceeds to a detailed discussion of the POLCAT concept and its implementation.

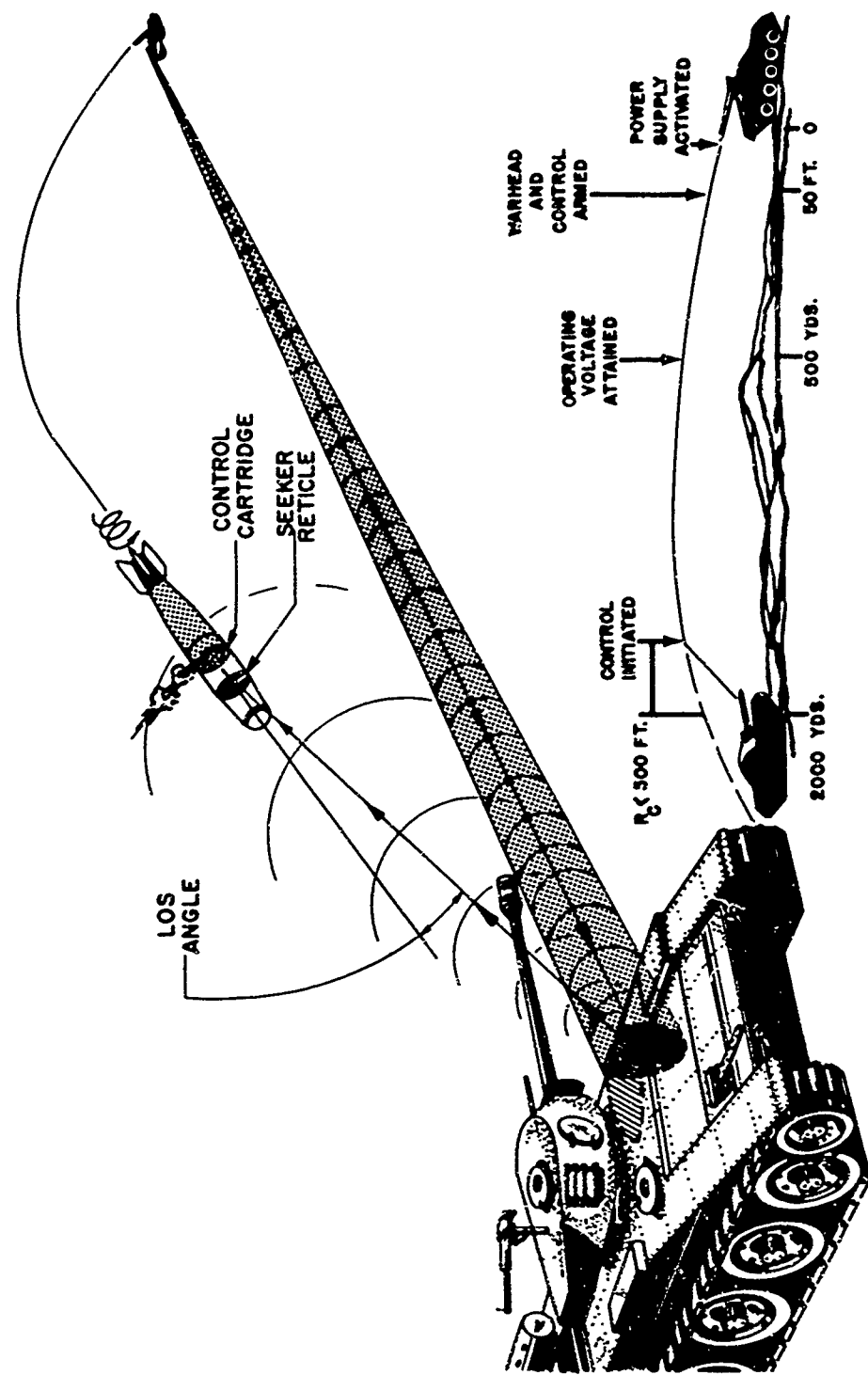
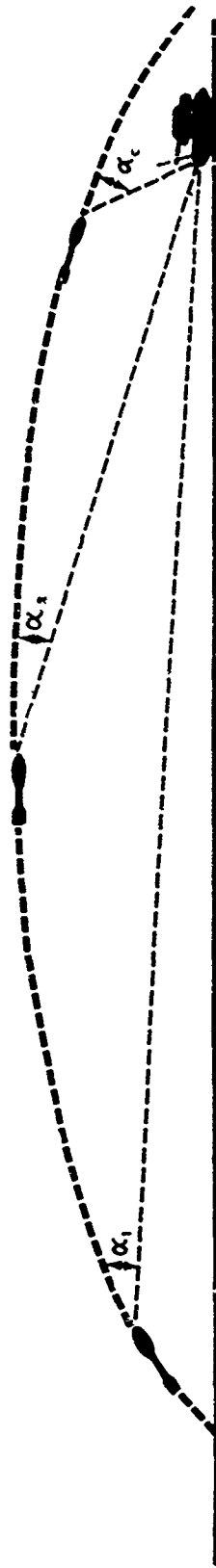


Figure 2.1-1. Illustration of POLCAT Concept

LINE-OF-SIGHT ANGLE DECREASES SLOWLY ----  $\alpha_1$  -  $\alpha_2$  ----



---UNTIL A MISS IS IMMINENT, THEN INCREASES

RAPIDLY ---  $\alpha_c$  --- AS TARGET IS APPROACHED

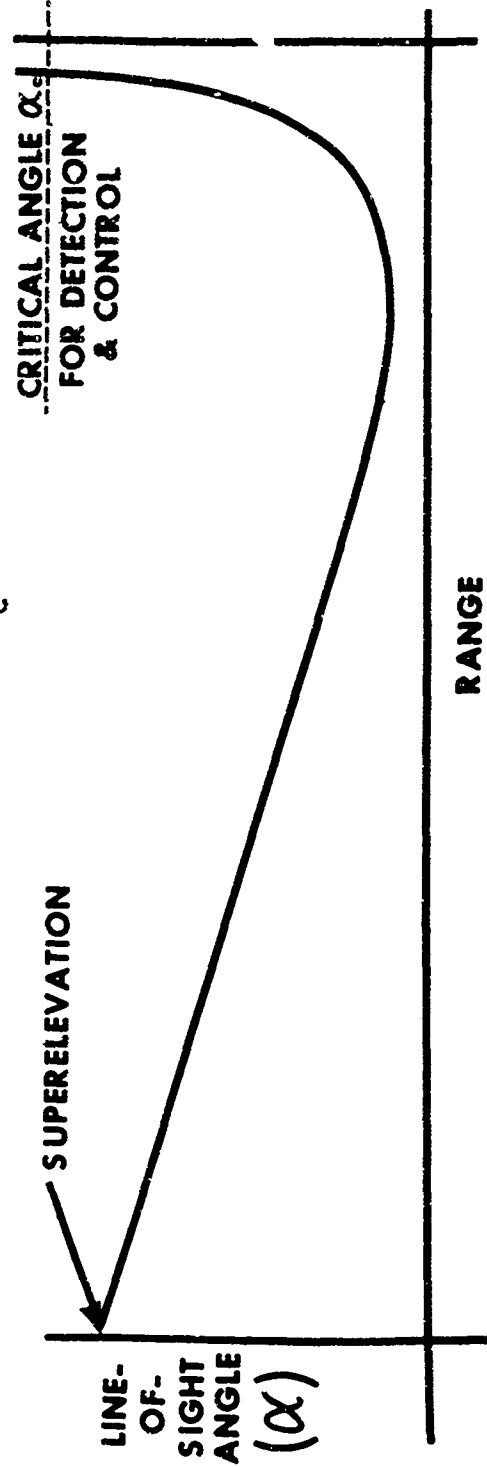
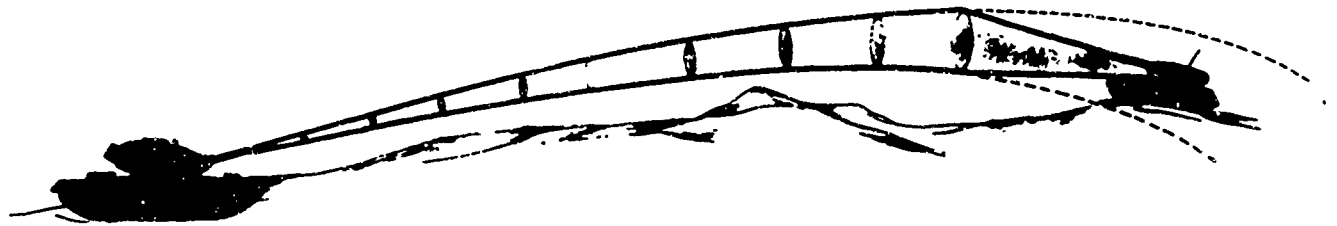


Figure 2.1-2. POLCAT Steering Law

# **POLCAT CORRECTS ONLY THOSE SHOTS DESTINED TO MISS**



**--- WITH A SINGLE, PRE-DETERMINED, INSTANTANEOUS PULSE**

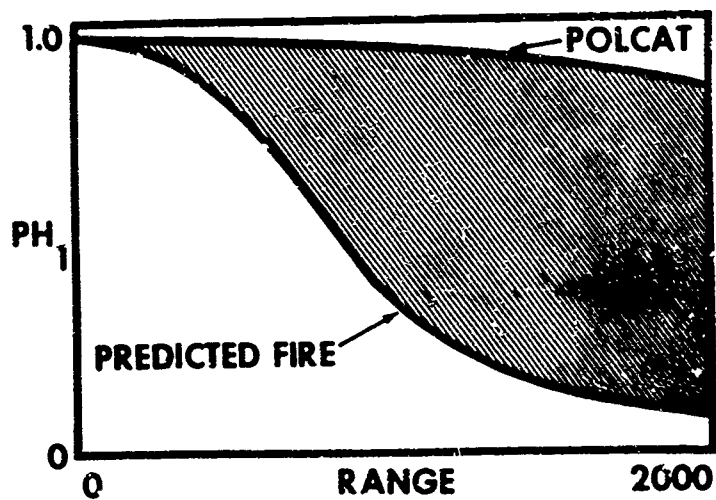
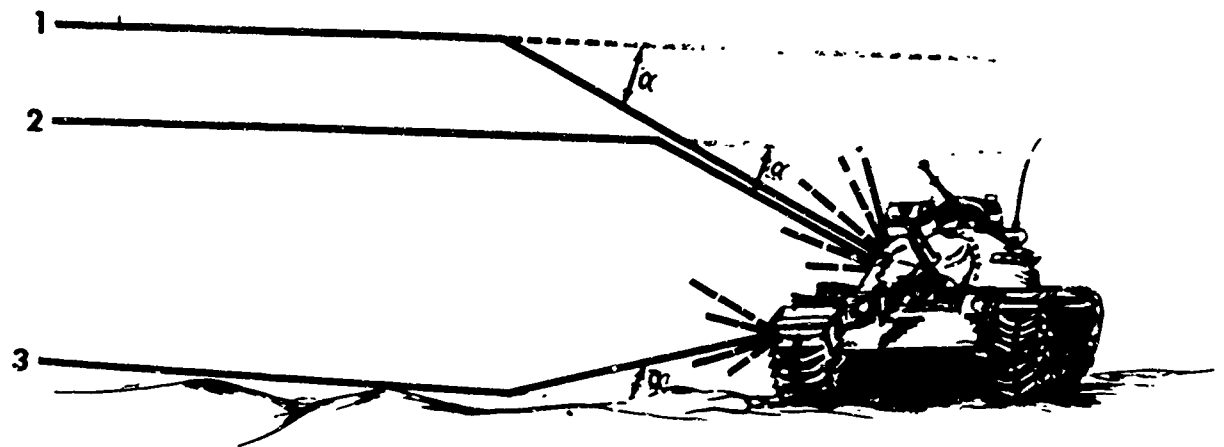


Figure 2.1-3. Effect on Probability of Hit



### 3.0 System Design

This section presents results of the program that was undertaken to develop a test system capable of demonstrating the functional performance of the POLCAT concept. A program plan was adopted which took cognizance of the limited resources available for execution of the contemplated flight tests. At the outset, it was established,

- (a) that the demonstration would not attempt to simulate tactical performance at maximum target ranges or under quasi-combat conditions;
- (b) that the existing XM89 recoilless rifle would be used for testing, and that the XM419 projectile would be modified for test purposes rather than develop a new round;
- (c) that the design goal for pulser development be limited to 25 lb-sec impulse.

Accordingly, analyses, design studies, laboratory tests, and field tests were undertaken to develop the necessary flight hardware, and to generate operational and field data essential to the successful execution of a firing program.

Section 3.1 presents the results of the aerodynamic design and test effort, and an estimate of the projectile flight characteristics.

Section 3.2 gives the structural design and analysis of the modified XM419 projectile.

Section 3.3, Control, describes the design studies and tests that were performed in the development of a 25 lb-sec pulser.

Section 3.4, Guidance, presents a thorough analysis of semi-active homing link performance. Further, it describes the designs of the seeker and illuminator, and the tests that were conducted to qualify these equipments.

### 3.1 AERODYNAMICS

The objective of the aerodynamics effort was, specifically, the development of an experimental or test projectile for use in the flight test demonstration of the POLCAT concept. While the test round would not possess the characteristics of a tactical round, it was required that all the basic elements of guidance and control essential for tactical use be incorporated within the test projectile.

The aerodynamic development effort consisted of two primary tasks: design and test. The nature and scope of tasks are described in Sections 3.1.1 and 3.1.2. Based on the results of this work, an analysis was conducted to provide an estimate of aerodynamic performance. The expected flight characteristics of test projectiles are given in Section 3.1.3.

Finally, a summary of the overall aerodynamic effort including specific recommendations for future development work is presented in Section 3.1.4.

The aerodynamic notation used throughout this section of the report is given in Table 3.1-1 which also provides equations relating aerodynamic and ballistic coefficients.

#### 3.1.1 Aerodynamic Design

The scope and the nature of the aerodynamic design effort was established early in the program when it was decided to adapt an existing projectile to the needs of the contemplated flight test demonstration rather than attempt the development of a completely new round. This decision was quite practical since the objectives of the flight demonstration could be achieved without incorporating a warhead in the test pro-

Table 3.1-1 Aerodynamic Notation

$C_D$	drag coefficient, $\frac{\text{Force}}{qS}$
$C_L$	lift coefficient, $\frac{\text{Force}}{qS}$
$C_{L_\alpha}$	variation of lift coefficient with angle of attack
$C_M$	pitching moment coefficient, $\frac{\text{Moment}}{qSd}$
$C_{M_\alpha}$	variation of pitching moment coefficient with angle of attack
$C_{M_q} + C_{M_{\dot{\alpha}}}$	pitch damping coefficient
$C_N$	normal force coefficient, $\frac{\text{Force}}{qS}$
$C_l$	rolling moment coefficient, $\frac{\text{Moment}}{qSb}$
$C_{l_p}$	roll damping coefficient
$C_{l_\delta}$	variation of rolling moment with fin cant angle
$b$	span of projectile fin
$d$	projectile diameter
$m$	projectile mass
$M$	Mach number
$q$	dynamic pressure, $1/2 \cdot V^2$
$p$	roll rate
$S$	projectile frontal area
$V$	velocity
$\alpha$	angle of attack
$\theta$	pitch angle
$\phi$	roll angle
$\delta$	fin cant angle
$\delta_b$	fin bevel angle
$\rho$	density of air

Table 3.1-1 (continued)

Since considerable reference is made to ballistic literature, the relations between the aerodynamic and ballistic coefficients of interest are listed below.

$$\begin{aligned}K_D &= (S/2d^2) C_D \\K_L &= (S/2d^2) C_{L\alpha} \\K_M &= (S/2d^2) C_M \\K_H &= (S/4d^2)(C_{Mq} + C_{M\dot{\alpha}}) \\K_A &= (S/4d^2) C_{lp}\end{aligned}$$

These equations are based on the use of projectile diameter and frontal area as characteristic length and area, respectively, for aerodynamic notation; projectile diameter and the square of the diameter as characteristic length and area, respectively, for ballistic notation.

jectile. As a consequence, an existing projectile could reasonably accommodate the elements of guidance and control after its warhead had been removed.

An aerodynamic design study of the 120mm XM419 round was subsequently undertaken to determine the nature and the consequences of the modifications required for conversion to a POLCAT test projectile. These modifications included:

- (a) the replacement of XM419 nose assembly by a seeker head;
- (b) the introduction of cant or bevel to the XM419 tail fin assembly to induce a constant projectile spin rate throughout flight.

It was recognized that modification of nose shape would establish drag characteristics considerably different from those of the XM419 round. However, no great changes or difficulties were anticipated relative to the pitch stability of the test projectile.

Any increase in projectile drag would be due primarily to the seeker optical configuration. The selection of an optical design, however, had to be based on optical performance and structural requirements as well as aerodynamic considerations. The actual optical design that was chosen did, in fact, commit the test projectile to a blunt nosed configuration; the degree of bluntness being a function of the size of the seeker aperture. The POLCAT test projectile shown in figure 3.1-1 reflects the final decision relative to a nose shape which provided the maximum possible aperture and the acceptance of higher projectile drag. This decision was made after a drag analysis had indicated that the

expected increase in drag would not be inordinately high. (This expectation later proved to be "inordinately" optimistic.)

Fulfillment of the requirement of providing constant projectile spin rate throughout flight involved problems of both aerodynamic design and tail fin fabrication. The aerodynamic design problem consisted of selecting the correct tail fin cant or bevel angle so as to maintain projectile spin rate within limits acceptable to the functioning of the guidance and control system. The question of whether a desired fin cant or bevel angle could be machined with sufficient accuracy and not distorted in the gun tube during firing was not examined extensively. However, a limited investigation favored the use of fin bevel rather than fin cant.

At the time the aerodynamic design study was initiated, the most useful experimental data available had been obtained in wind tunnel tests of the XM419 round. These data provided estimates of drag, lift, and pitch stability only. No information was immediately available relative to roll damping or rolling effectiveness. The following discussion describes the methods that were used to estimate the drag, pitch, and roll characteristics of the test projectile.

#### 3.1.1.1 Drag

The technique for estimating test projectile drag coefficient utilized the available wind tunnel data on XM419 round (1). First, an analytical drag build-up for the XM419 round was performed that matched these test results. Once a satisfactory match was achieved, the same drag build-up method was used to obtain test projectile drag coefficient. Since the only external difference between the XM419 and the test projec-

tiles was nose shape, the drag build-up only had to be modified for the nose pressure drag. In performing the drag analysis, the following conditions were assumed:

- (a) completely turbulent boundary layer.
- (b) standard NACA sea level density (for Reynolds number).
- (c) drag due to lift is negligible in angle of attack range of interest.

The drag build-up accounted for skin friction drag, nose pressure drag, afterbody pressure or boattail drag, tail fin pressure drag, and base drag of the tail boom and fins.

Skin friction drag was calculated using the average skin friction coefficients given by the extended Frankl and Voishel analysis for a turbulent boundary layer (2). In the computation of skin friction, the entire body length, including the boom, was used as the characteristic length of the body whereas the mean aerodynamic chord of the tail was used as the characteristic length for the fin.

The nose pressure drag coefficient of the XM419 round was estimated analytically by applying transonic similarity techniques (3) to free flight, test data (4). Nose pressure drag coefficients at the higher supersonic Mach numbers were obtained from the Taylor-Maccoll conical flow equation. The nose pressure drag coefficient of the blunt nosed test projectile was estimated directly from experimental data (5).

The afterbody pressure drag coefficient was obtained from wind-tunnel data in the subsonic and transonic range (6) and by the second-order theory of Van Dyke at supersonic Mach numbers (7).

The estimation of tail fin pressure drag coefficient was obtained by an analytical method that applied transonic similarity techniques to the determination of the pressure distribution over non-lifting airfoils (3).

The base drag coefficients for the tail boom and fins were obtained from existing compilations of test data (8-11).

The variation with Mach number of the total drag coefficient of the test projectile considering the sources of drag described above is presented in figure 3.1-2. The experimental data for nose pressure drag, afterbody pressure drag, and base pressure drag, used in the drag build-up, are given in the Design Data Supplement.

#### 3.1.1.2 Normal Force and Pitching Moment

Estimates were made of the normal force slope coefficient and the pitching moment slope coefficient of the test projectile using the same general procedure that was followed in the estimating drag coefficient. Experimental data were utilized to estimate the normal force and center-of-pressure of the tail assembly, boattail, and nose of the XM419 round (1), (12), (13). The experimental data were extended by appropriate similarity techniques to obtain an estimate of the change in normal force and center-of-pressure location caused by the blunt nose of the POLCAT test projectile.

The estimated variation of normal force slope coefficient and pitching moment slope coefficient with Mach number is given in figure 3.1-3.

For the purposes of the subsequent performance analysis, an estimate of the coefficient of damping-in-pitch was made from experimental



data (14-18). A value of  $(C_{M_q} + C_{M_{\dot{\alpha}}})$  of 2.0 per degree, constant over the Mach range, was selected. This estimate cannot be considered reliable in view of the lack of test data directly applicable to the test projectile.

### 3.1.1.3 Roll Damping and Rolling Effectiveness

Since test data of roll characteristics of the XM419 round were not available, an extensive design study was conducted to determine the roll damping moment and rolling moment due to tail fin cant of the test projectile. The study of these characteristics included the application of existing theory and the correlation of experimental data.

The theoretical estimate of roll damping moment coefficient ( $C_{l_p}$ ) was obtained using subsonic and supersonic thin airfoil theory (19-21). The estimate based on test data (22,23) was obtained after these data were normalized with respect to transonic similarity parameters to account for the effects of aspect ratio, thickness, sweepback and aeroelasticity. The results of the analysis are given in figure 3.1-4. In view of the limitations associated with the theoretical determination, it was decided that the value based on the test data be used in the analysis of test projectile roll performance. The estimated value of -.139 for  $C_{l_p}$  applies to a pair of tail fins where damping moment is expressed as,

$$L_p = C_{l_p}(qS_f b)(pb/2V)$$

where  $n$  = number of fin pairs,  $S_f$  = area of a fin pair ( $ft^2$ ),  $b$  = span of fin pair ( $ft$ ), and  $p$  = roll rate ( $rad/sec$ ).

In the case of the XM419 round or the test projectile, the span of

a fin pair (b) equals projectile body diameter (d) and the number of pairs of tail fins (n) equals 3. The table below gives the effect of number of fins on damping coefficient as determined from test data (22, 23).

n	$C_{1p}$ (/rad)
2	-.139
3	-.129
4	-.119
6	-.099

The estimated value of total damping coefficient ( $C_{1p}'$ ) based on projectile frontal area (S) is -.277 (/rad).

$$C_{1p}' = n C_{1p} (S_f/S)$$

The rolling moment coefficient ( $C_{1\delta}$ ) was estimated by determining the lift curve slope coefficient of a tail fin pair and, then, converting to rolling moment coefficient. The estimated values based on theory (24) and test data (25-27) are shown in figure 3.1-4. In the subsequent performance analysis, the estimate of rolling moment coefficient based on test data is used.

Rolling moment due to fin cant is defined below.

$$L_\delta = n_\delta (C_{1\delta} \delta) (q S_f b)$$

where:

$n_\delta$  = number of canted fin pairs

$\delta$  = fin cant angle (rad)

Using this notation, the steady state roll rate is expressed as,

$$p = (n_\delta/n) (C_{1\delta}/C_{1p}) (2V/b) \delta$$

### 3.1.2 Aerodynamic Test

The plan for qualifying the design of the POLCAT test projectile defined a series of wind tunnel, spark range, and field tests which would assure fulfillment of the aerodynamic requirements during the flight test demonstration of the POLCAT concept. At the time the plan was formulated, it was recognized that the full test program could not be accomplished within the available resources of the overall program. An aerodynamic test program was undertaken that was consistent with the immediate objectives of the program; namely, to obtain initial test verification of aerodynamic design effort described in the previous section. Thus, the wind tunnel tests that are described in this report represent only the initial phase of the aerodynamic test program that was contemplated.

Based on the test projectile design that had been established, wind tunnel models were constructed and two series of tests were conducted to determine drag, lift, pitching moment, and rolling moment characteristics.

#### 3.1.2.1 Description of Wind Tunnel Tests

Supersonic tests were conducted in the Supersonic Wind Tunnel Number 3 at the Ballistics Research Laboratories, Aberdeen Proving Ground. Data were obtained at Mach numbers of 1.36, 1.58, and 1.78 using a one-third scale model. Maximum body diameter of the model was 1.71 inches and its axial moment of inertia was  $0.81 \text{ lb-in}^2$ . Despite the reduced scale, reflected shock wave impingement was encountered when testing at Mach number equal 1.36. Hence, some doubt exists as to the accuracy of

data obtained at this condition. Static tests were conducted of the model with three nose sections providing nose cant angles of 0, 2.0, and 3.5 degrees. Measurements were taken of normal and axial forces, pitching moment, and base pressure. After the static tests were completed, a series of tests were conducted with the model mounted on a spinning sting to determine roll damping characteristics and rolling effectiveness induced by beveling the leading edge of all the tail fins. Data were obtained with a 15 degree bevel, a 45 degree bevel, and a 90 degree bevel.

Transonic tests were conducted in the 8-foot transonic pressure tunnel at NASA Langley Research Center. Data were obtained in the Mach number range of 0.7 to 1.2 using a full scale model. Static force and moment measurements were made at a stagnation pressure of 1 atmosphere and a stagnation temperature of 120° F. Roll damping measurements were made at a stagnation pressure of 1/4 atmosphere. Static tests were conducted with nose cant angles of 0, 2.0, and 3.5 degrees. Spin dynamics tests were conducted with the uncanted nose and with the leading edges of the fins beveled at 15, 30, and 45 degrees.

#### 3.1.2.2 Test Results

The results of the transonic and supersonic tests were consistent and exhibited a smooth transition between data from the two tunnels. In addition to presenting the combined results of the two test series, the test data are compared with the estimated aerodynamic coefficients described in the preceding section. The comparison is significant in reviewing the Aerodynamic Performance, Section 3.1.3, in that the performance analyses utilized the estimated values of the aerodynamic coef-

ficients. The test data were not available at the time the analyses were performed.

Drag measurements at zero angle of attack indicated that the test projectile demonstrates an early transonic drag rise and extremely high supersonic drag as shown in figure 3.1-5. These effects have been attributed, primarily, to the blunt nose and, to a lesser extent, to transonic separation on the projectile afterbody. If the estimated drag coefficient is interpreted as an aerodynamic requirement, then, the blunt nose of the test projectile design must be modified for drag reduction.

The variation with Mach number of normal force slope coefficient and pitching moment slope coefficient is presented in figures 3.1-6, and 3.1-7. The discontinuity in these data occurring between Mach numbers .90 and .95 is believed to be caused by boundary layer separation on the boattail section. The data indicate that the test projectile possesses a high degree of stability particularly at subsonic velocity; this being a usual characteristic of blunt nosed projectiles.

Measurements were made to determine the effect of nose cant on projectile lift and pitching moment. The angle of zero lift and the angle of zero moment were determined at transonic and supersonic Mach numbers for nose cant angles of 2.0 and 3.5 degrees. Since displacement of the lift curve would not have a significant effect on projectile flight for nose cant angles of interest, only the zero pitching moment angle is shown in figure 3.1-8. Nose cant can be considered in the same manner as any type of aerodynamic malalignment wherein aerodynamic balance of trim is achieved by projectile yaw. The test data show a static trim

angle of less than 1.0 degrees. Since the primary purpose of inducing spin in fin stabilized projectiles and rockets is to eliminate the effects of aerodynamic misalignment, the magnitude of the zero moment angle will be substantially reduced at the roll rates contemplated for the test projectile. Therefore, it is unlikely that nose cant alone would establish a trim angle large enough to affect seeker operation provided that roll resonance is not induced. (It is to be noted that the ratio of projectile roll rate to pitch frequency will probably exceed 2.0).

Measurements were made of the projectile roll damping characteristics and the rolling effectiveness of leading edge fin bevel. The results of these tests are shown in figure 3.1-9. The roll damping data, obtained without fin bevel, indicates that the rolling damping coefficient is constant with Mach number. Some degree of uncertainty exists with rolling effectiveness data because the effects of friction could not be accurately accounted for. It was found that the frictional torques in the bearings were not reproducible from test to test.

### 3.1.3 Aerodynamic Performance

The successful implementation of the POLCAT concept requires that a number of fundamental relationships between the aerodynamic properties of the projectile and the operating characteristics of the control system and the guidance system must be maintained. Without fully analyzing the nature and the consequences of these relationships, the critical aerodynamic performance items were investigated.

- 1) time of flight
- 2) projectile yaw
- 3) roll rate

The goal of POLCAT aerodynamic design is to minimize, insofar as possible, each of these factors. A following performance analysis was conducted and the results evaluated relative to this goal.

A summary of the aerodynamic coefficients used to determine the flight performance of the POLCAT test projectile is given in Table 3.1-2. While a major discrepancy exists between the estimated values and the wind tunnel values for drag coefficient, the subsequent performance results based on the estimated drag coefficient can be treated as goal or requirement for any future aerodynamic design effort to reduce test projectile drag.

The performance analysis also considered a larger caliber POLCAT projectile since interest has been directed toward the possible development of a 152mm POLCAT system. The known mass and dimensional characteristics of the test projectile and the estimated characteristics of a 152mm POLCAT round are given in Table 3.1-3. The estimated values of the aerodynamic coefficients were used in analyzing the performance of the 152mm projectile since the wind tunnel results were not available when the analysis was performed.

#### 3.1.3.1 Trajectory Characteristics

The variation of velocity with range was determined for the POLCAT test projectile based on estimated and test values for drag coefficient and are presented in figure 3.1-10. In addition, the velocity variation of the XM419 round is given to demonstrate the improbability of maintaining supersonic velocity at long range with a muzzle velocity of 1800 ft/sec. Given that the POLCAT system must operate at this muzzle velocity,

Table 3.1-2

## Summary of Estimated Aerodynamic Coefficients

	M .8	M 1.3
$C_D$	.225 (.600)	.590 (1.19)
$C_{N\alpha}$	.057 (.046)	.065 (.060)
$C_{M\alpha}$	-.095 (-1.53)	-.101 (-.100)
$C_{M\alpha} + C_{Mq}$	2.0	2.0
$C_{lp}$	-.277 (-.210)	-.277 (-.210)
$C_{l\delta}$	.460	.509

The values in parentheses are wind tunnel test data.

Table 3.1-3

## Projectile Characteristics

	120mm Test Projectile	Proposed 152mm Round
m (slugs)	.61	1.24
S (ft <sup>2</sup> )	.122	.196
d (ft)	.39	.50
$I_x$ (slug-ft <sup>2</sup> )	.009	.024
$I_y$ (slug-ft <sup>2</sup> )	.306	.665



and that it is not possible to design a POLCAT projectile with less drag than the XM419 round, then, the aerodynamic design must provide adequate transonic flying qualities. This requirement is fulfilled to some degree with the blunt nosed test projectile which is capable of maintaining pitch stability in the transonic regime.

The time of flight of the test projectile is shown in figure 3.1-11 where time of flight is given also for a vacuum trajectory as a function of range. These data are presented since many POLCAT system errors are a function of time of flight. The guidance performance (false alarm rate) of the POLCAT demonstration system is dependent upon time of flight. Further, the tactical application of the POLCAT concept requires that time of flight be minimized in order to maintain system performance against moving targets.

The effect of muzzle velocity on velocity variation with range and on time of flight was examined in a trajectory study of the 152mm POLCAT projectile. The results, presented in figures 3.1-12 and 3.1-13, indicate how effectively increased muzzle velocity can be used to fulfill time of flight or downrange velocity requirements.

#### 3.1.3.2 Yaw Characteristics

An analysis was performed to determine the effect of initial disturbances and crosswind on projectile yaw characteristics. The estimated aerodynamic coefficients given in Table 3.1-2 were used in the investigation of the projectile dynamic behavior. The initial disturbance was characterized by an angle of yaw of 1 degree; this value being based on test firings of the XM89 system (29). (See Design Data Supplement for

test values.) An expected value for crosswind of 10 ft/sec was selected based on available meteorological data (30).

The steady state yaw due to crosswind is shown in figure 3.1-14. Once again the advantage of high velocity is apparent. The transient of yaw is not indicated since it is negligible downrange where effects of crosswind are more serious. The assumed damping-in-pitch coefficient and the induced spin rate which is considerably greater than the pitch frequency provide the necessary conditions for the rapid damping of any transient motion. This is illustrated in figure 3.1-15 where the response of the projectile to initial disturbance is shown for various values of muzzle velocity. The actual periodic variation of yaw angle is not given. Instead, the envelope of the yaw amplitudes are plotted.

Other phenomena such as mass asymmetry, projectile malalignments (nose or tail cant), and yaw of repose have not been considered in the analysis since it is unlikely that their contribution to total projectile yaw is significant. However, based on the results obtained in the analysis, it appears that the design of the seeker and the choice of scanning angle must be predicated on operating with yaw angles of at least  $1/2$  degree; 1 degree under less favorable conditions.

### 3.1.3.3 Roll Characteristics

The effect of tail fin cant on the test projectile roll rate was investigated using the estimated values of the aerodynamic coefficients given in Table 3.1-2. A muzzle velocity of 1800 ft/sec was assumed and initial spin rates of 15 RPS and 20 RPS were examined. The results for the initial spin rate of 20 RPS are shown in figure 3.1-16 where project-

the pitch frequency is also given. The results indicate that canting tail fins does not appear to be a practical technique for controlling roll rate because small changes in cant angle induce large changes in roll rate history. (0.2 degree change in cant angle induces a change in roll rate of 15 RPS.) Since roll rate proved to be so sensitive to fin cant angle, it was of interest to compare the relative effectiveness of fin cant to leading edge fin bevel. The cant and bevel angles that provide equal rolling effectiveness were determined by combining the estimated and the test values of the rolling derivatives. (See figure 3.1-5)

$$\delta = \frac{\delta_b}{2} \frac{C_{l_p}}{C_{l_\delta \text{ est}}} \frac{C_{l_{\delta_b}}}{C_{l_p \text{ test}}}$$

#### 3.1.4 Summary

At this point, the POLCAT test projectile is evaluated relative to its expected performance as a flight test round.

- (1) The blunt nose induces extremely high drag resulting in long time of flight and rapid velocity decay. However, it is unlikely that drag reduction can provide supersonic velocities out to a range of 1000 meters unless muzzle velocity is increased. See figure 3.1-18.
- (2) The test projectile possesses adequate pitch stability throughout flight. For

- (2) cont'd. the expected initial disturbances, the projectile yaw will be sufficiently low for ranges beyond 500 meters to permit functioning of the guidance and control system. However, yaw due to crosswind imposes a severe operating condition for the seeker which can only be mitigated by increasing muzzle velocity. It might be noted that the pitch damping of the projectile has not been thoroughly investigated and this could ultimately be a serious design deficiency.
- (3) The requirement for establishing constant roll rate for guidance and control system operation precludes problems associated with roll resonance. Beveling the leading edges of the tail fins appears to provide a satisfactory roll rate time history. The required bevel angle cannot be determined without additional aerodynamic tests.

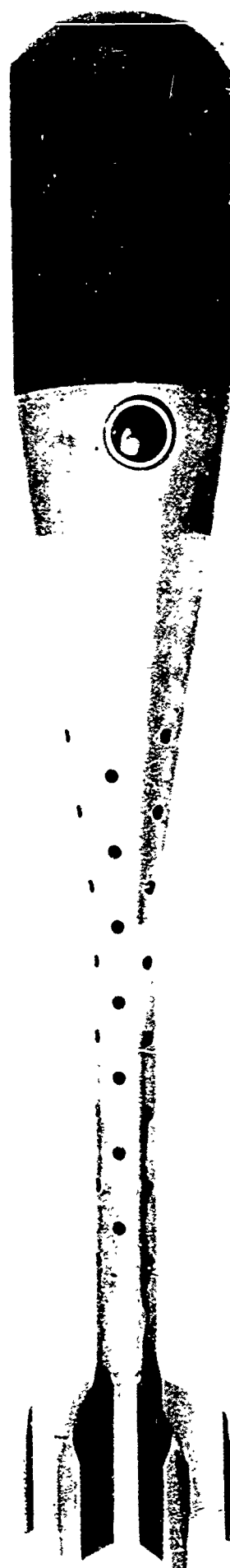


Figure 3.1-1. POLCAT Test Projectile

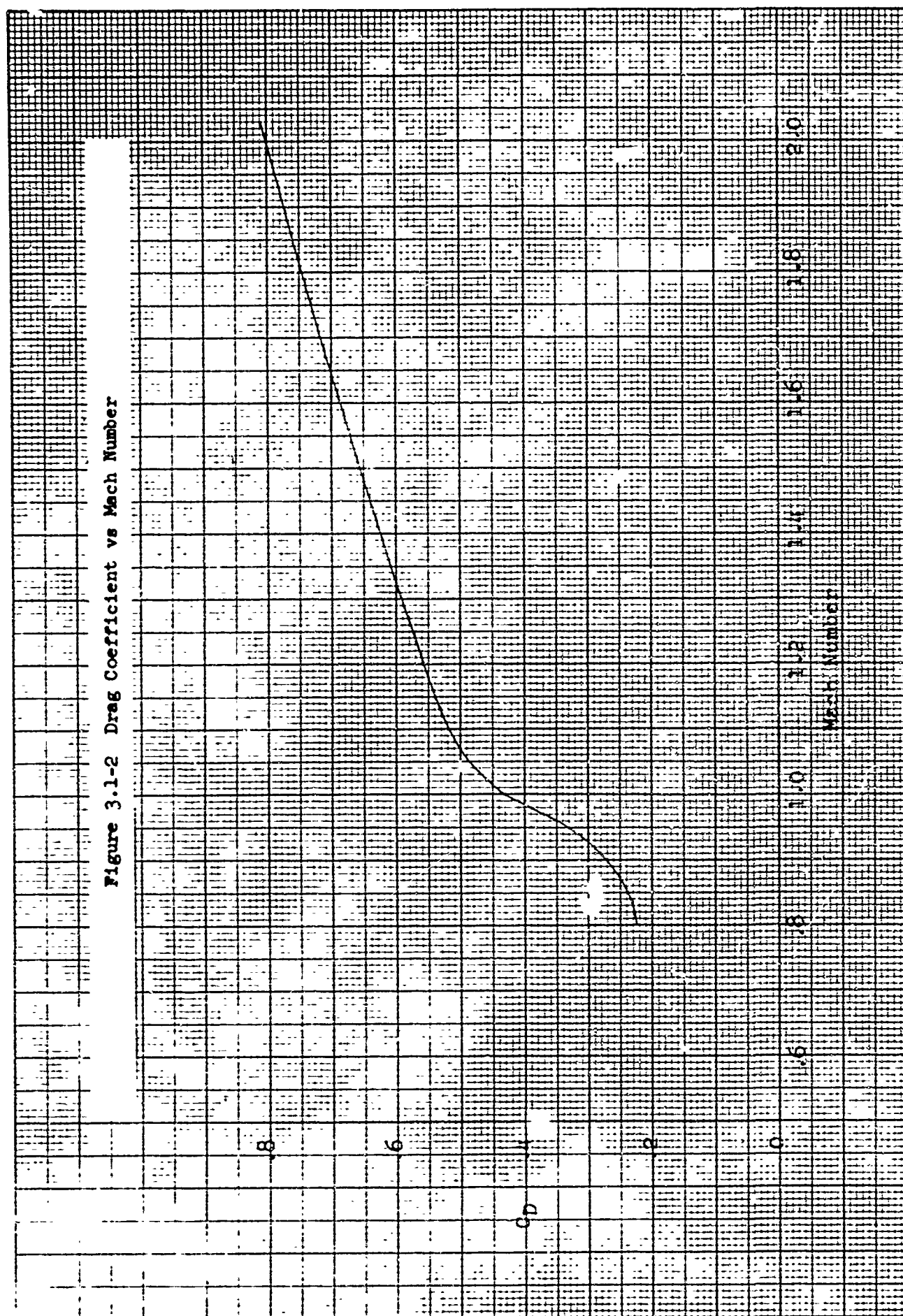


Figure 3.1-3 Normal Force and Pitching  
Moment Slope Vs Mach Number

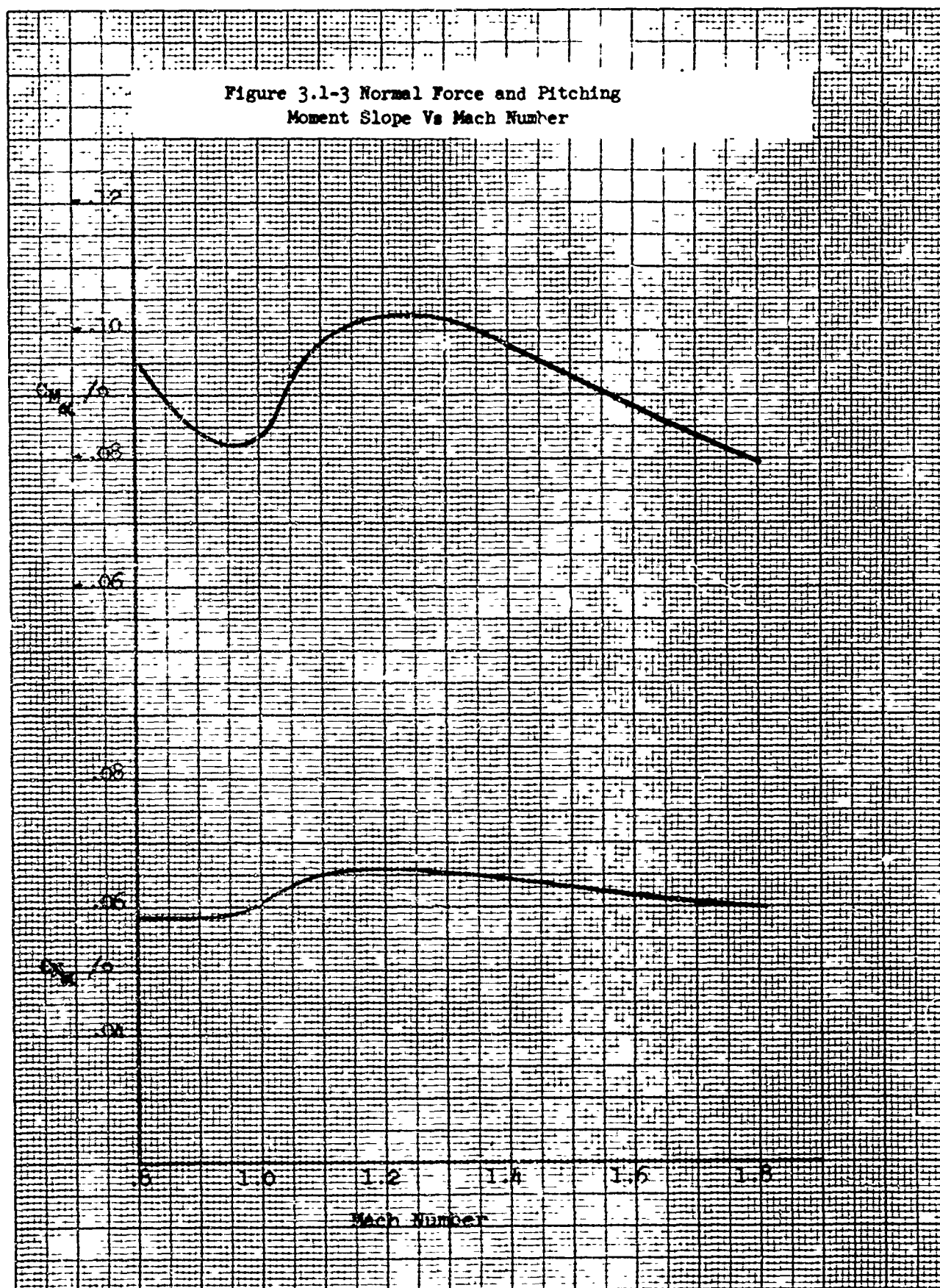


Figure 3.1-4 Damping and Rolling Moment  
Derivatives vs Mach Number

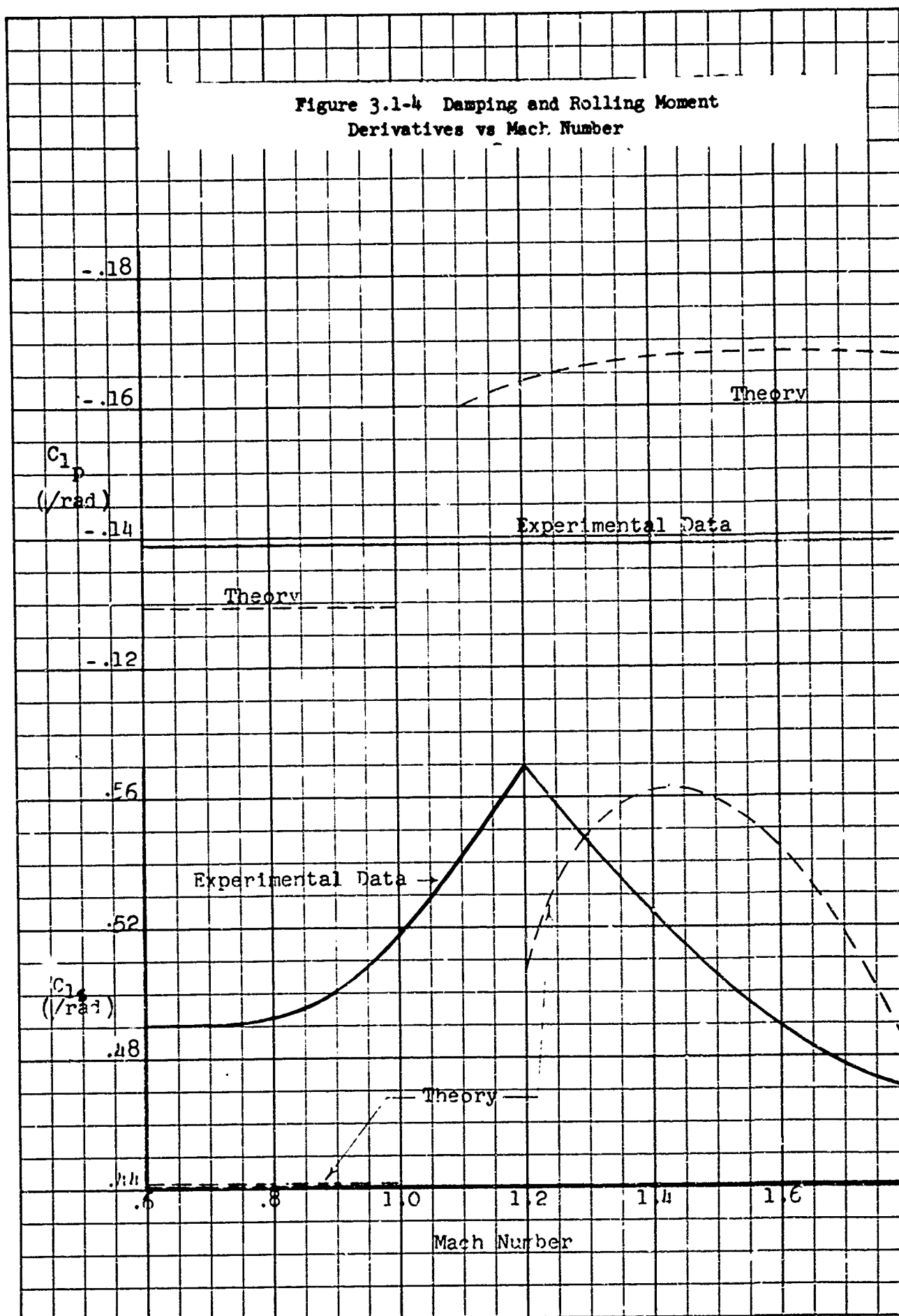




Figure 3.1-5 Comparison of Estimated Drag Coefficient with Test Data

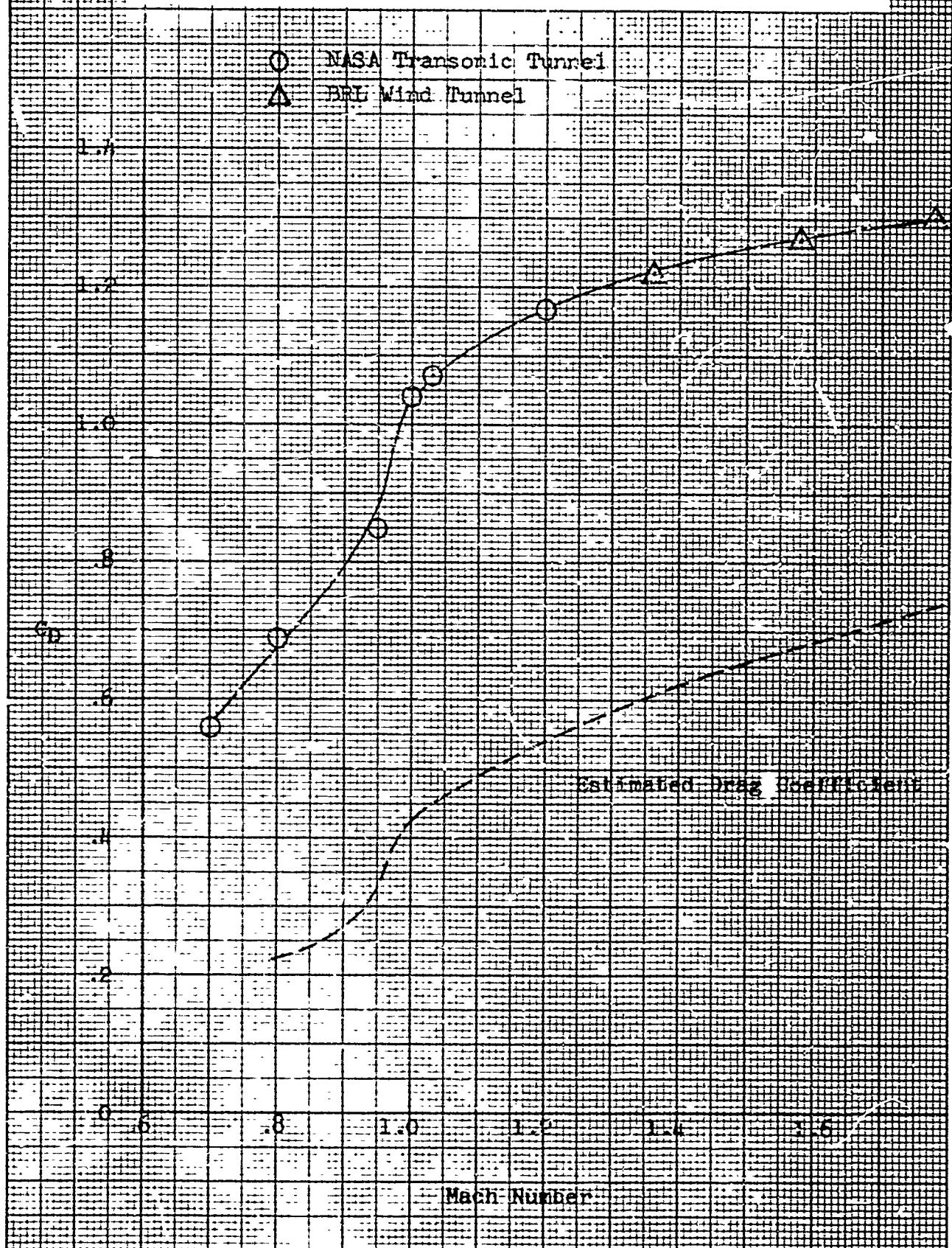


Figure 3.1-6 Normal Force and Lift Curve  
Slope Coefficients vs Mach Number

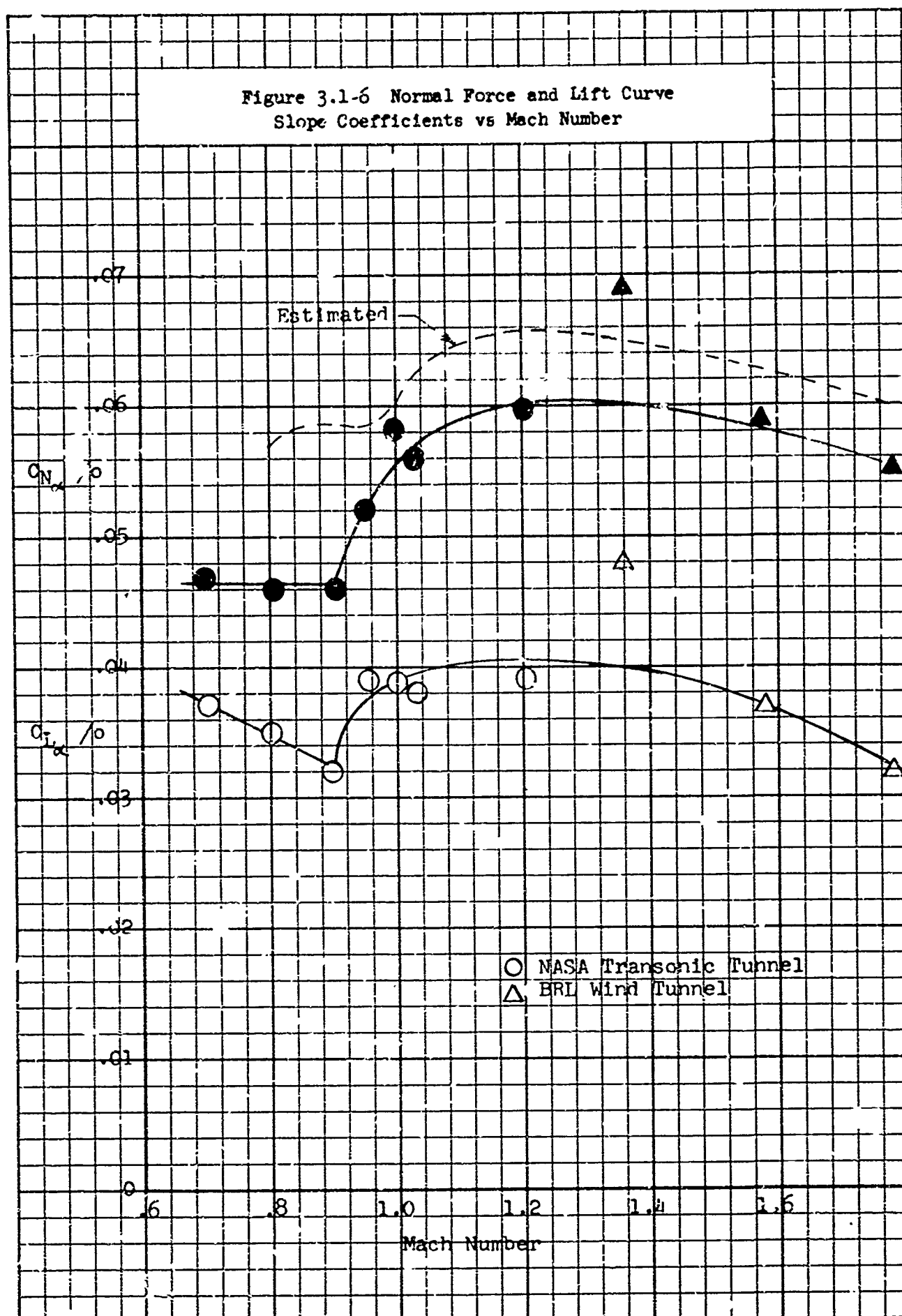


Figure 3.1-7 Comparison of Estimated Pitching Moment Slope Coefficient with Test Data

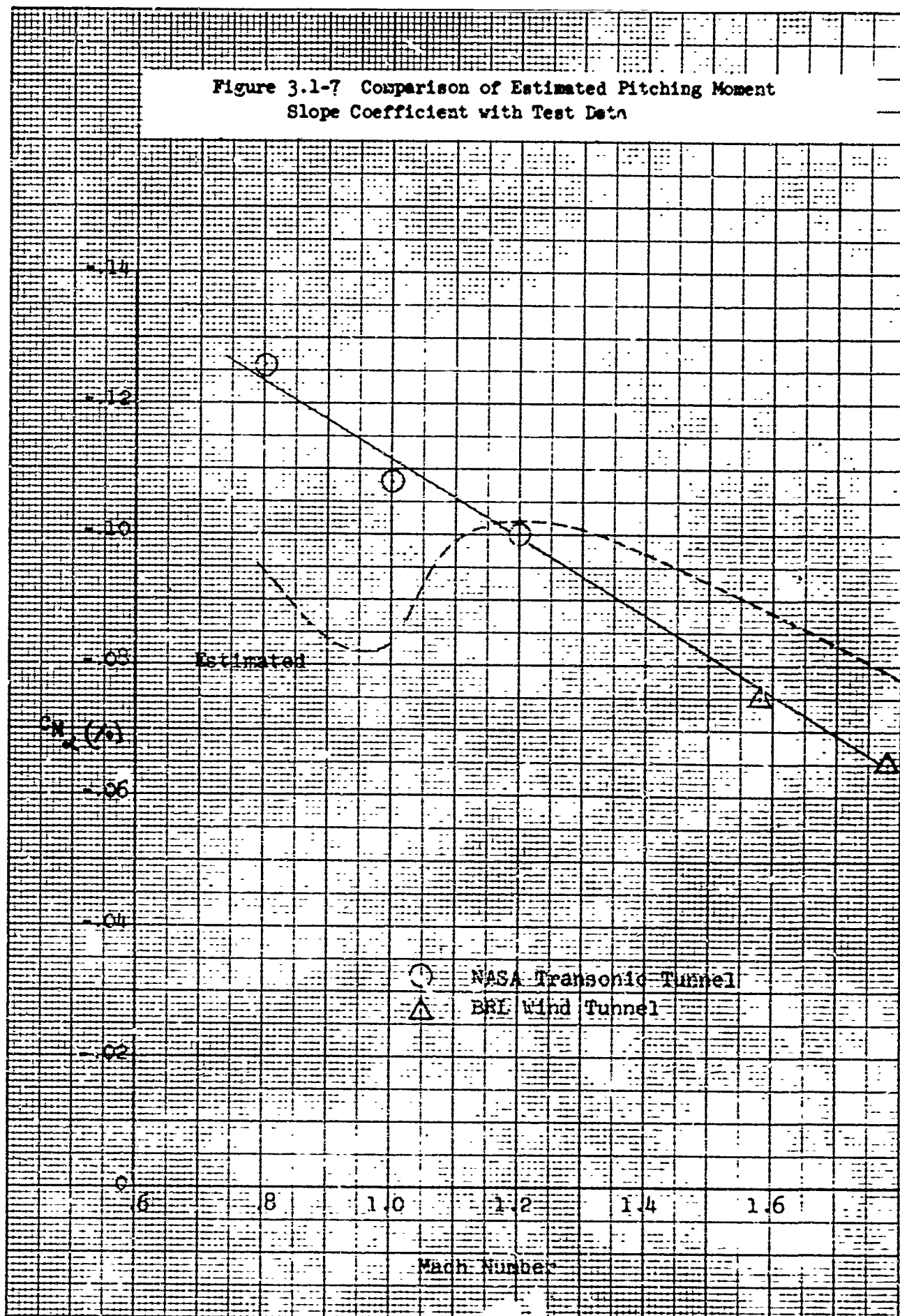


Figure 3.1-8 Effect of Nose Cant Angle on Trim Angle of Yaw

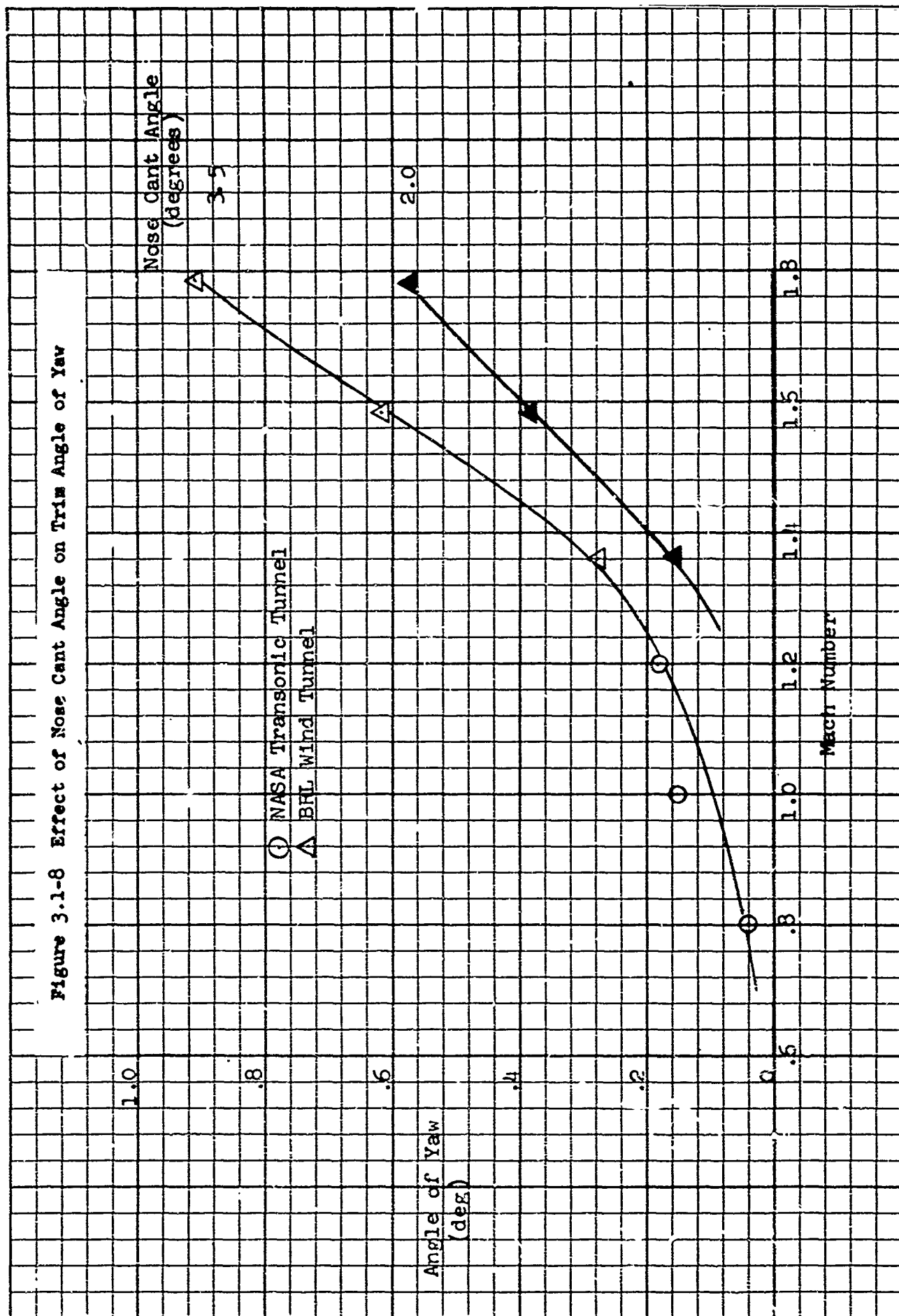


Figure 3.1-9 Damping-in-Roll and Rolling Effectiveness Coefficients vs Mach Number

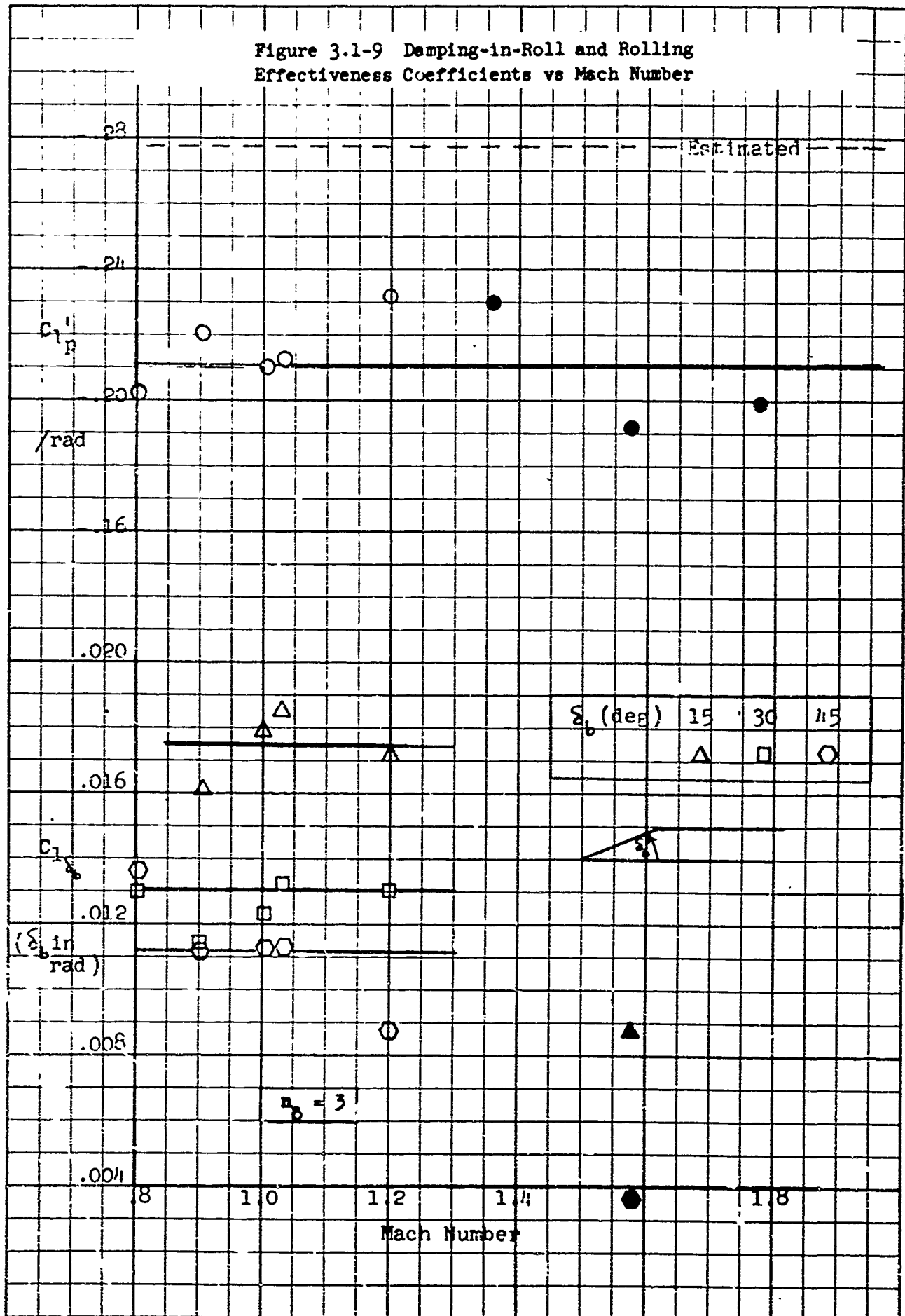


Figure 3.1-10 Velocity Variation vs Range  
for POLCAT Test Projectile

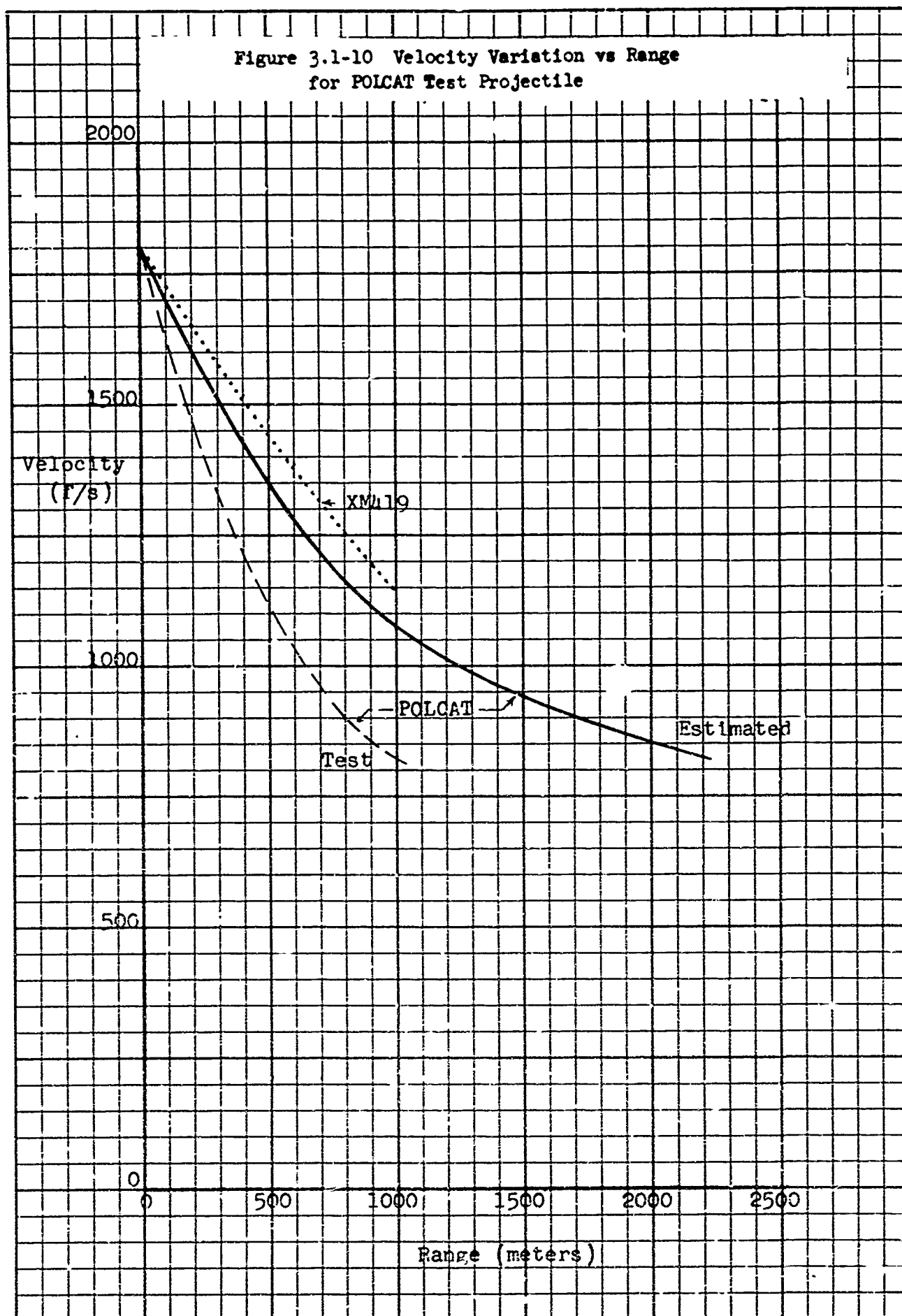


Figure 3.1-11 Time of Flight vs Range  
for POLCAT Test Projectile

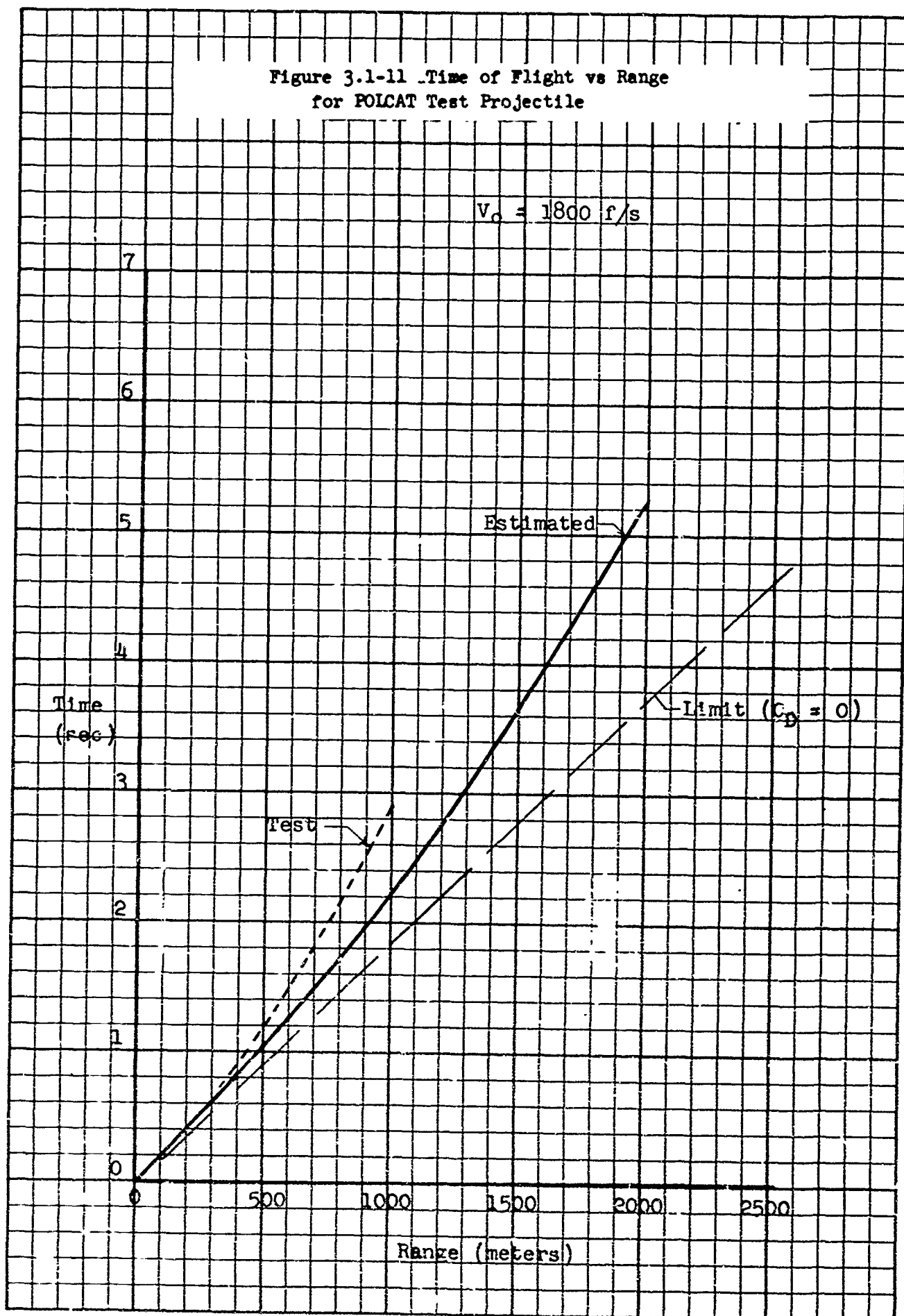


Figure 3.1-12 Effect of Muzzle  
Velocity on Velocity Decay

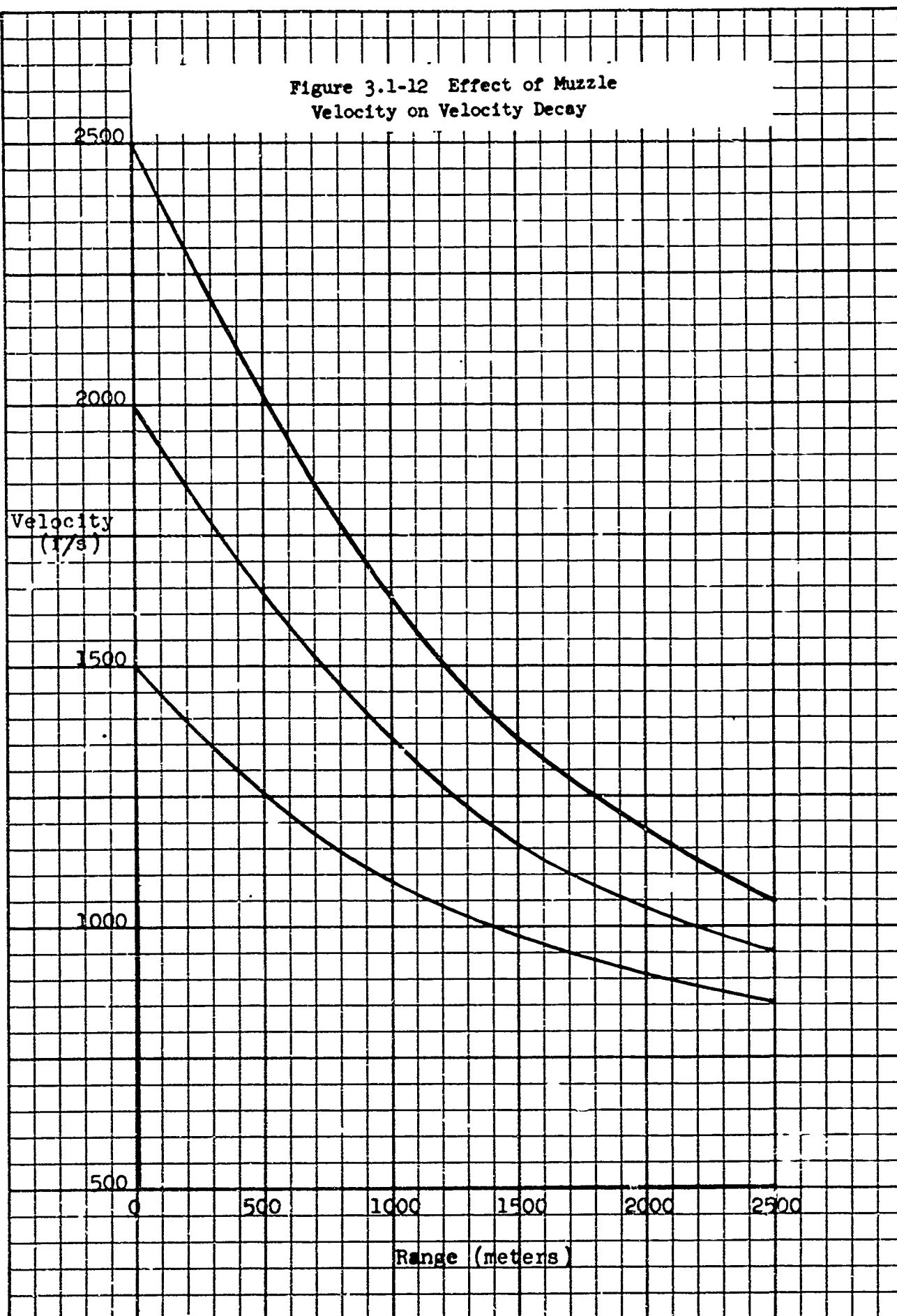




Figure 3.1-13 Effect of Muzzle Velocity on Time of Flight

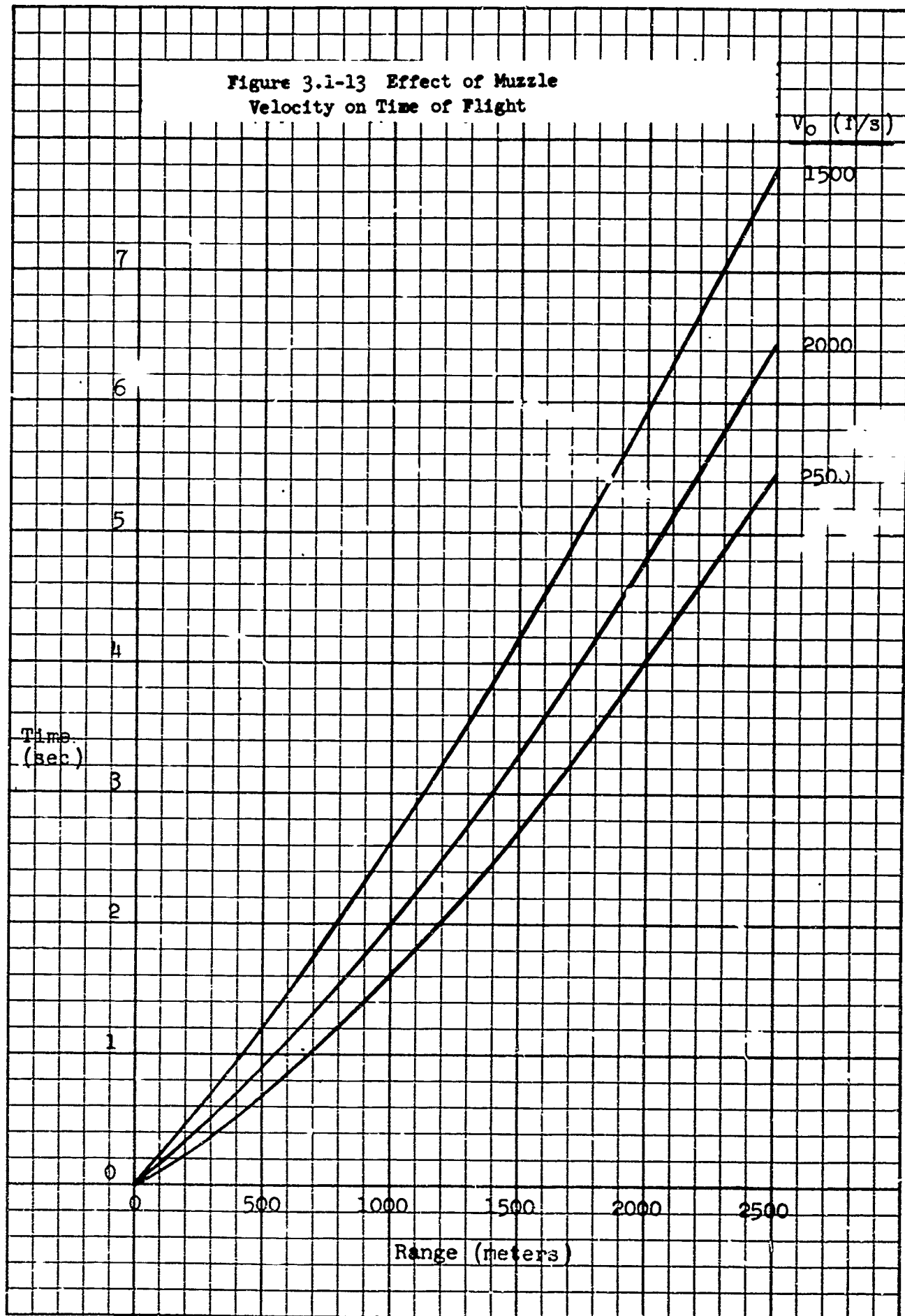


Figure 3.1-14 Steady State Yaw Due to Crosswind

Velocity of Crosswind: 10 f/s

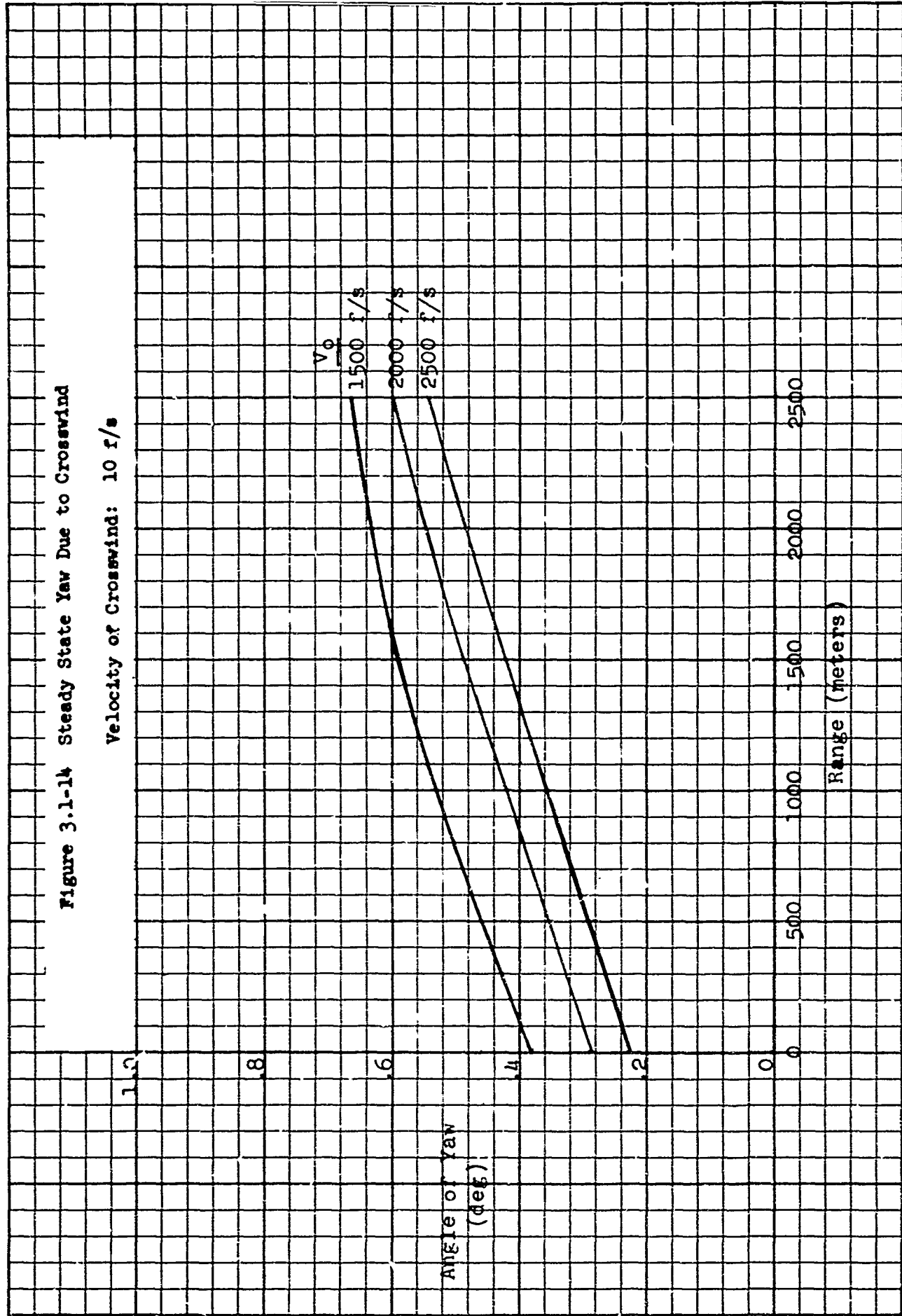


Figure 3.1-15 Damping in Yaw

Initial Yaw Angle:  $1^\circ$   
Roll Rate: 20 RPS

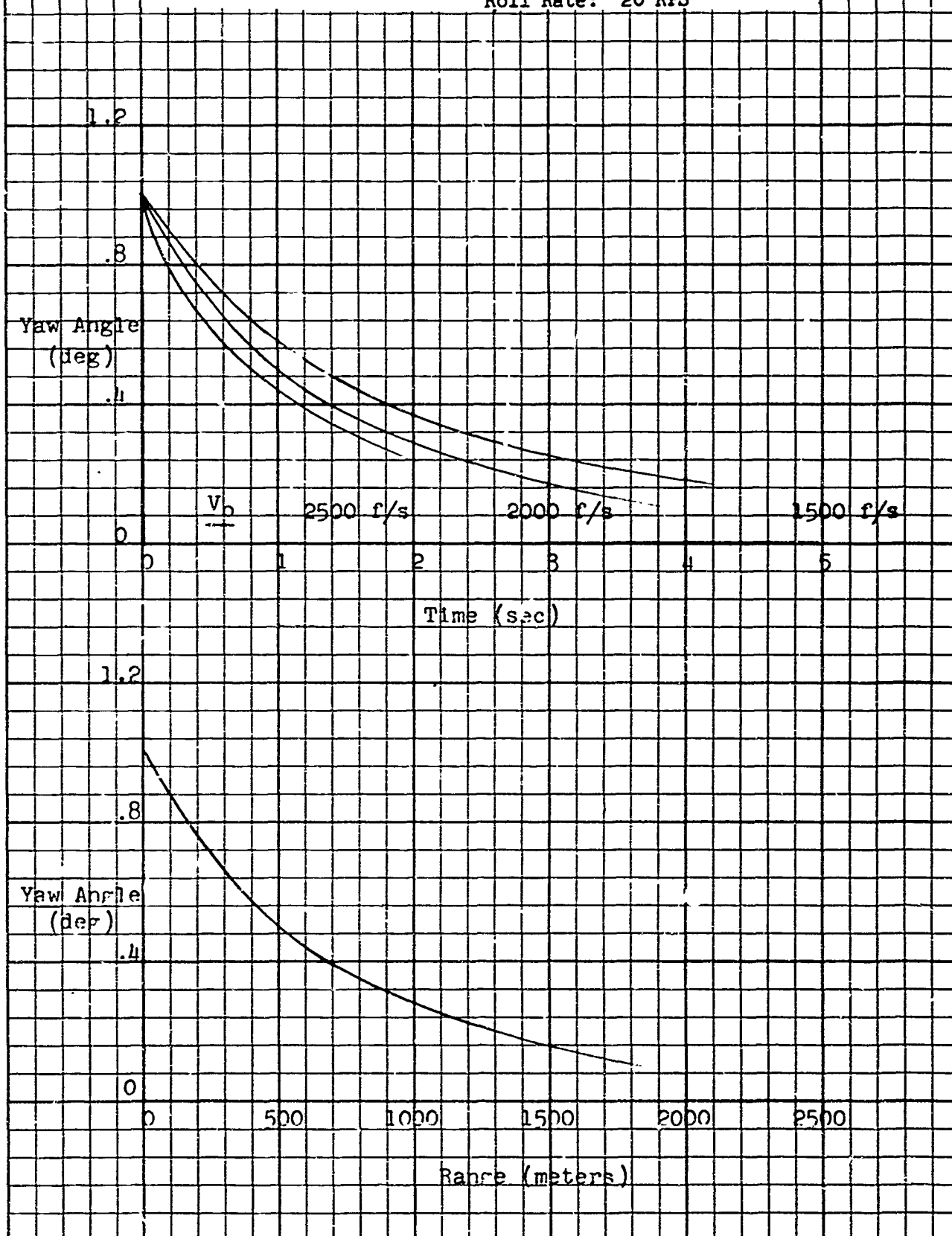


Figure 3.1-16 Effect of Fin Cant on Roll Rate Variation

Muzzle Velocity: 1800  $\text{m/s}$   
Initial Roll Rate: 20  $\text{CR/S}$

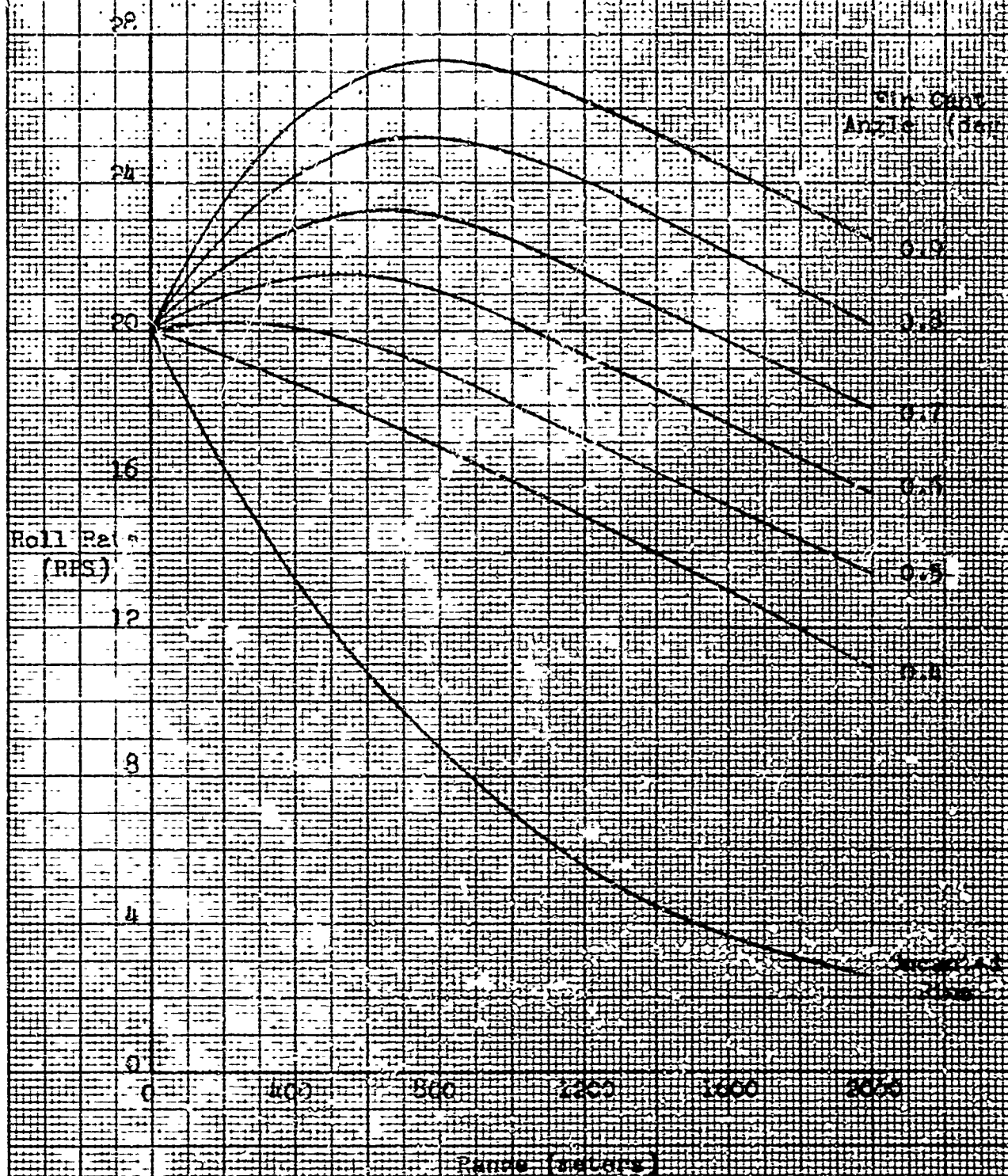


Figure 3.1-17 Comparative Rolling Effectiveness  
Fin Cant vs Leading Edge Bevel

All fin leading edges beveled  
One pair of fins canted

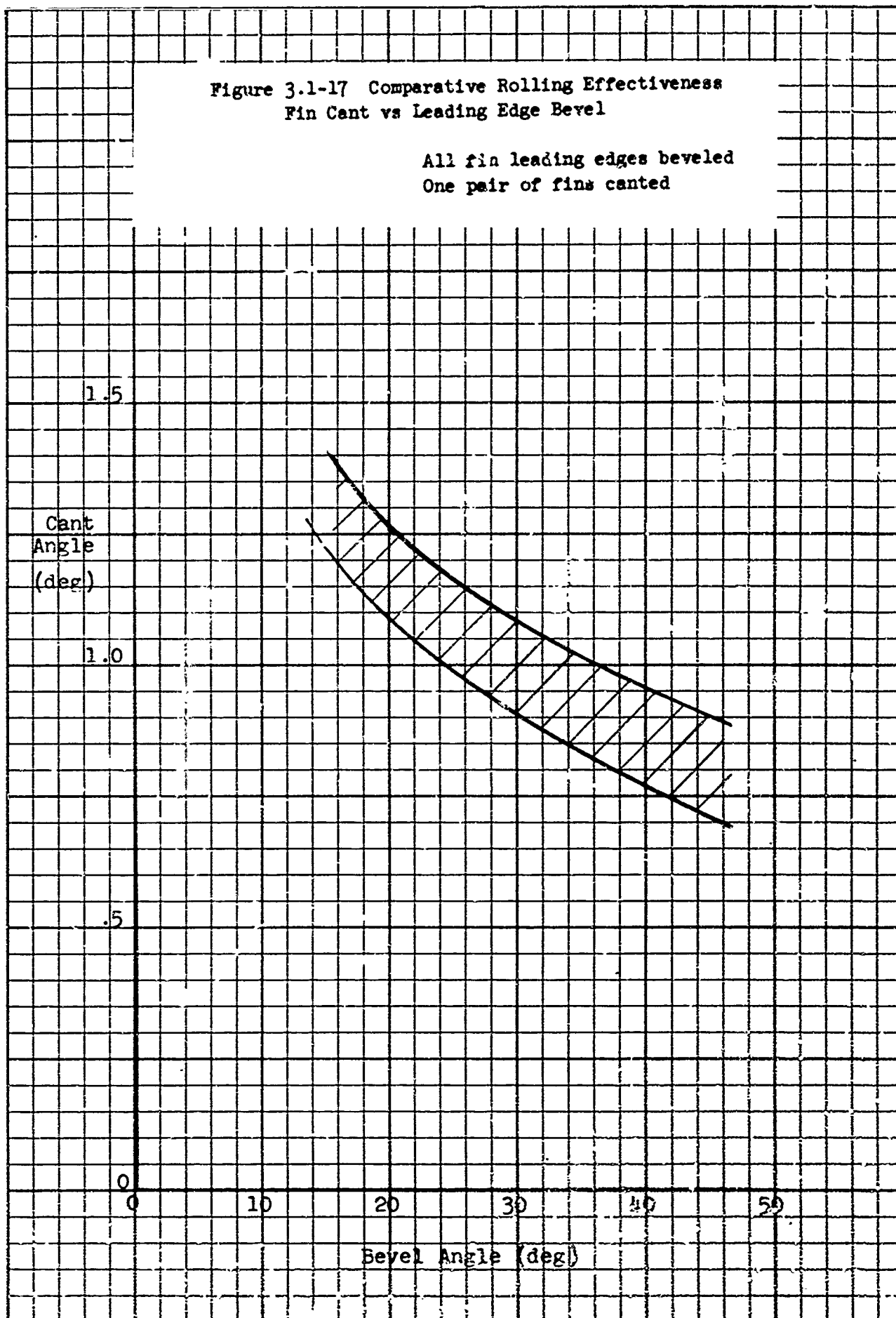
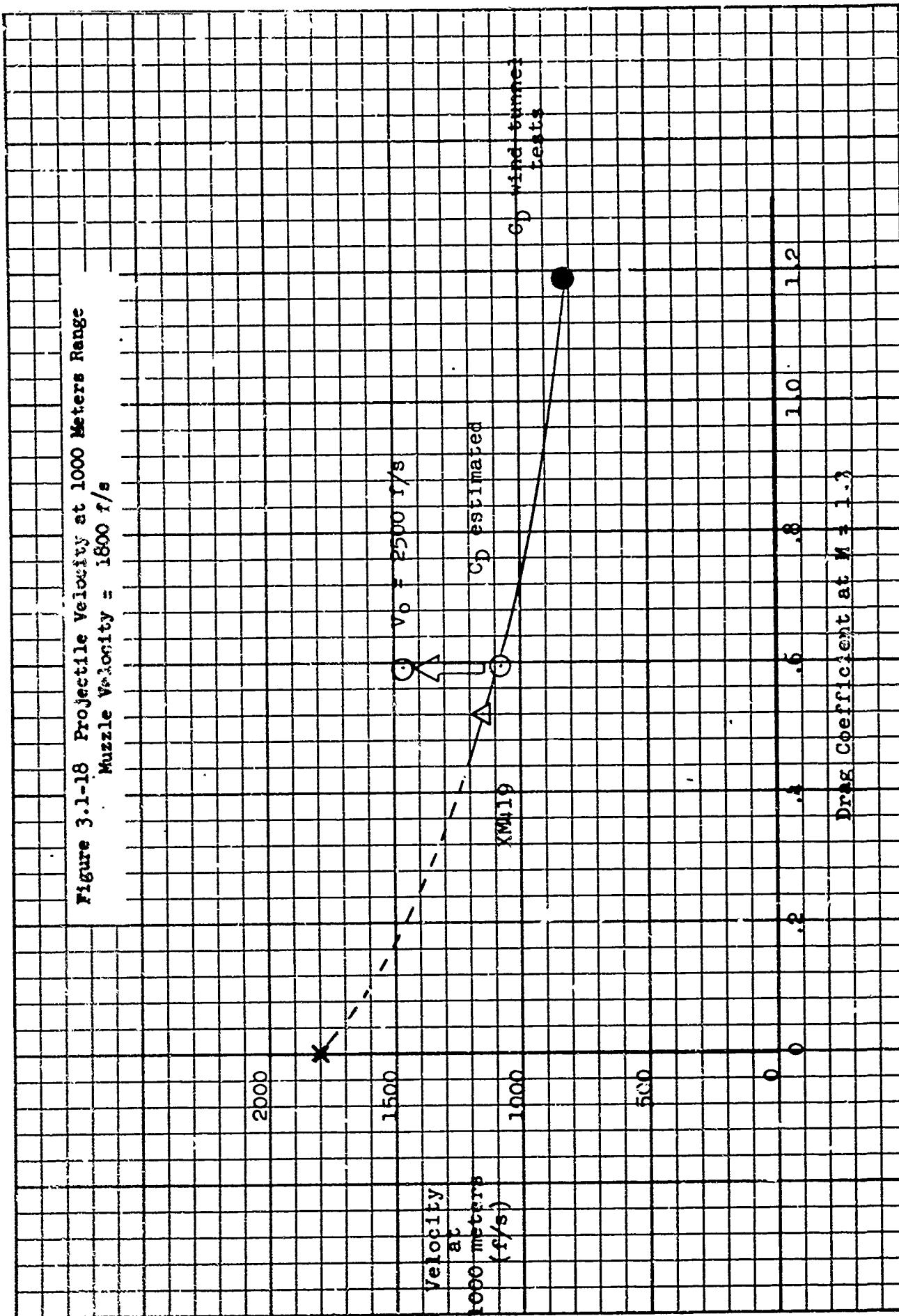


Figure 3.1-18 Projectile Velocity at 1000 Meters Range  
Muzzle Velocity = 1800 f/s



### Aerodynamic References

1. Arthur D. Little, Inc.: An Investigation of Projectile Stability of the XM419 Weapon System. Contract No. DA-19-020-507-ORD-5317, 1 February 1961 (Confidential).
2. Rubesin, M. W., Maydew, R. C., Varga, S.A.: An Analytical and Experimental Investigation of Skin Friction of Turbulent Boundary Layer on a Flat Plate at Supersonic Speeds. NACA TN 2305.
3. Spreiter, J. R., Alksene, A.: Theoretical Prediction of Pressure Distributions on Non-lifting Airfoils at High Subsonic Speeds. NACA TN 3096.
4. Stoney, W. E., Jr.: Transonic Drag Measurement of Eight Body-Nose Shapes. NACA RM KL7L53.
5. Wallskog, H. A., Hart, R. G.: Investigation of the Drag of Blunt-Nosed Bodies of Revolution in Free Flight at Mach Numbers from 0.6 to 2.3. NACA RM L53D14a, (Confidential).
6. Sihan, F. V., Cabbage, J. M., Jr.: Drag of Conical and Circular-Arc Boattail Afterbodies at Mach Numbers from 0.6 to 1.3. NACA RM L56K22 (Confidential).
7. Jack, J. R.: Theoretical Pressure Distribution and Wave Drag for Conical Boattails. NACA TN 2972.
8. Cleary, J. W., Stevens, G. L.: The Effects at Transonic Speeds of Thickening the Trailing Edge of a Wing with a 4-Percent-Thick Circular-Arc Airfoil. NACA RM 5LJ11.
9. Cabbage, J. M., Jr.: Jet Effects on Base and Afterbody Pressures of a Cylindrical Afterbody at Transonic Speeds. NACA RM L56C21
10. Van Hise, Vernon: Investigation of Variation in Base Pressure over the Reynolds Number Range in which Wake Transition Occurs for Nonlifting Bodies of Revolution at Mach Numbers from 1.62 to 2.62. NACA TN 3942, 1957.
11. Love, Eugene S.: Base Pressure at Supersonic Speeds on Two-Dimensional Airfoils and on Bodies of Revolution With and Without Fins Having Turbulent Boundary Layers. NACA TN 3819, 1957.
12. Krieger, R. H.: Wind Tunnel Tests on the T131 105mm Heat Projectile. BRL TN 565 (Confidential).
13. Krieger, R. H.: Wind Tunnel Tests on the T153 120mm Heat Projectile. BRL TN 724 (Confidential).

14. Karpov, B. G.: Aerodynamic and Flight Characteristics of the 90mm Fin Stabilized Shell, Heat, T108. ERL MR696.
15. Moore, John A.: Experimental Determination of Damping in Pitch of Swept and Delta Wings at Supersonic Mach Numbers. NACA RM L57G10a.
16. Tobak, Murray, Reese, David E., Jr., Beam, Benjamin H.: Experimental Damping in Pitch of  $45^\circ$  Triangular Wings. NACA RM A50J26.
17. Brown, Clarence A., Jr.: Flight Investigation at Low Angles of Attack to Determine the Longitudinal Stability and Control Characteristics of a Cruciform Canard Missile Configuration with a Low-Aspect-Ratio Wing and Blunt Nose at Mach Numbers from 1.2 to 2.1. NACA RM L55K16.
18. Clements, James E.: A Theoretical Analysis of a Simple Aerodynamic Device to Improve the Longitudinal Damping of a Cruciform Missile Configuration at Supersonic Speeds. NACA RM L55H31.
19. Toll, Thomas A., Queijo, M. J.: Approximate Relations and Charts for Low-Speed Stability Derivatives of Swept Wings. NACA TN 1581, 1948.
20. Malvestuto, Frank S., Jr.; Margolis, Kenneth, Ribner, Herbert S.: Theoretical Lift and Damping in Roll at Supersonic Speeds of Thin Sweptback Tapered Wings with Streamwise Tips, Subsonic Leading Edges and Supersonic Trailing Edges. NACA TR 97C, 1950.
21. Harmon, Sidney M., Jeffreys, Isabella: Theoretical Lift and Damping in Roll of Thin Wings with Arbitrary Sweep and Taper at Supersonic Speeds. NACA TN 2114, 1950.
22. Stone, David G.: A Collection of Data for Zero-Lift Damping in Roll of Wing-Body Combinations as Determined with Rocket Powered Models Equipped with Roll-Torque Nozzles. NACA TN 3955, 1957.
23. McDevitt, John B.: A Correlation by Means of Transonic Similarity Rules of Experimentally Determined Characteristics of a Series of Symmetrical and Cambered Wings of Rectangular Planform. NACA TN 1253, 1955.
24. Harmon, Sidney M., Jeffreys, Isabella: Theoretical Lift and Damping in Roll of Thin Wings with Arbitrary Sweep and Taper at Supersonic Speeds. NACA TN 2114, 1950.
25. Emerson, Horace F.: Wind-Tunnel Investigation of the Effect of Clipping the Tips of Triangular Wings of Different Thickness, Camber, and Aspect Ratio-Transonic Bump Method. NACA RM A53L03.



26. Krieger, R. H.: Wind Tunnel Tests of the T131 105mm Heat Projectile. BRL TN 565, 1951.
27. Krieger, R. H.: Wind Tunnel Tests of the T153 120mm Heat Projectile. BRL TN 724, 1952.
28. Arthur D. Little, Inc.: Analysis of Aerodynamic Characteristics of the LASH Projectile. Contract No. DA 19-020-ORD-5317, 1963.
29. U. S. Army Development and Proof Services, Aberdeen Proving Ground: Twelfth Memorandum Report on Engineering Test of 120mm Recoilless Rifle, XM105E1 with Cartridge, HEAT, XM452.
30. U. S. Department of Commerce: Local Climatological Data. 1958.

## 3.2 STRUCTURES

A design and test effort was conducted to establish the required structural modifications for converting the XM419 round to a test projectile incorporating a seeker head and a pulser and capable of sustaining the loads imposed at launch and by impulse control.

The structural design of the test projectile is described in Section

3.2.1 The tests that were conducted to qualify the design are described in Section 3.2.2. A summary of the overall effort is given in Section 3.2.3.

### 3.2.1. Structural Design

The decision to develop a POLCAT test projectile from the XM419 round and to utilize the XM89 gun for the planned demonstration firings clearly defined the critical considerations of structural design.

(a) The aft assemblies of the XM419 round (aft body adapter, tail boom adapter, and tail) were retained in the test projectile design, these assemblies were capable of sustaining the axial loads at firing; an acceleration of 10,000 g. It remained, then, to determine the ability of these structural elements to sustain the transverse loads imposed by impulse control.

(b) The seeker optical and electronic components, and structural housing had to be designed for both the axial loads of initial acceleration and the transverse loads of control.

(c) In order to obtain adequate muzzle velocity within the performance ratings of the XM89 gun, the design of the seeker head and the pulser, and the subsequent modifications to the XM419 round had to be achieved such that the weight of the test projectile did not exceed 18 pounds.

(d) The arrangement and installation of the seeker and the pulser components had to provide for locating the pulser nozzle at the center of gravity of the test projectile.

The test projectile design that was established for these requirements is shown in figure 3.2-1. The weight of the projectile is 19.4 pounds and the length is 32.8 inches. A projectile weight and balance summary is given below.

Item	Weight (lb)	Distance from Nose (in)
Seeker head	9.32	3.6
Pulser	5.29	9.1
Boom adapter	4.03	16.0
Tail	<u>.71</u>	31.9
Total Weight	19.35	

C. G. 8.7 inches from nose

The load analysis that was performed (Section 3.2.1.2) used the following distribution of weight to simulate the test projectile.

	Weight (lb)	Distance from Nose (in)
Nose	5.9	1.5
Center Body	9.0	9.4
Tail	1.9	34.5

#### 3.2.1.2. Stress Analysis

Stress analyses were performed at critical stations along the aft body adapter, the tail boom adapter, and tail to determine the structural integrity of these assemblies under transverse impulsive loading. An overshoot factor of 1.5 was used. It was determined that these XM419 assemblies could be used if impulse was limited to approximately 20 lb-sec. If the magnitude of impulse for control were increased to 40 lb-sec, then, the outside diameter of the tail boom would have to be increased from 1.375 to 1.62 inches at the forward end and allowed to taper to 1.375 inches at the aft end.

The seeker head assembly shown in figure 3.2-6 was analyzed for a longitudinal load factor of 10,000 g and a lateral load factor 855 g imposed at the time of control with an overshoot factor of 1.5. Computations indicated the design to be adequate for both the transverse and axial loadings. The results are given in Table 3.2-1.

The design of the support structure was conceived specifically to minimize the bearing pressure on the optical element during axial loading. This was achieved by, first, providing a large bearing surface and, then placing a groove at the periphery of the structure, below the bearing surface. The purpose of the groove is to prevent a condition of edge support of the optical element by establishing a structural cross-section that eliminates deformation of the inner portion of the bearing surface under

Table 3.2-1 Summary of Stress Analysis

Assembly (See Figure 3.2-1)	LOAD		Factor of Safety
	Transverse	Avial	
	Moment (in-lb)	Shear (lb) Comp. (lb)	
Screw Head			
Section A-A		8,500	+ .78
Section B-B		112,500	+1.50
Station 0.5		162,000	+ .24
Station 0.5	40,500	10,500	+5.0
Boom Adaptor			
Station 15.0	55,100	6,500	+3.1
Station 22.5	21,800	2,000	+ .04

Assumptions:

- (a) axial load = 10,000 lb
- (b) transverse load = 855 lb (21 lb-sec impulse)
- (c) ultimate/limit = 1.25
- (d) overshoot factor = 1.5

axial load.

It is to be noted that the scan angle of the seeker is offset from the longitudinal axis of the projectile by the inclination from the normal of the bearing surface of the support structure (see Figure 3.2-6).

#### 3.2.1.2 Load Analysis

The purpose of this task was to investigate the structural behavior of the test projectile under a transverse impulsive load. The usual procedure of analysis is to assume the projectile is a rigid body and determine the inertia mass distribution on the body that will put it in equilibrium with the external applied system of loads. These loads are, then, multiplied by a dynamic overshoot factor between 1.0 and 2.0, depending upon the rigidity of the body and the time duration of the externally applied load, to determine an equivalent static load. In the actual stress analysis that was performed, an overshoot factor of 1.5 was assumed. This represents an upper bound if the applied impulse is assumed to be triangular. Therefore, the specific objective of this task was to obtain a reasonably close approximation of the dynamic overshoot factor in order to verify the assumed margins of safety. In order to determine the overshoot factor, it was necessary to assume an elastic model and compare the maximum inertia loads with those obtained for the rigid model. Consequently, the transient structural, as well as rigid body response, to a transverse

impulse was determined. The test projectile, because of its variable section properties, is best described mathematically by a series of partial differential equations having variable coefficients, but because of the complexity of this type of analysis, a simpler mathematical model was formulated. The model assumed was a three mass system connected by two springs as shown in figure 3.2-2. A transverse impulse was assumed at the center mass ( $m_1$ ). The structural response of the configuration was estimated by determining  $x_1(t)$ ,  $x_2(t)$ ,  $x_3(t)$  and  $\theta(t)$ . However, only  $x_2(t)$  and  $x_3(t)$  are required to describe the elastic deformation. The general equations describing these quantities are given in Table 3.2-2. In the derivation of the equations, structural damping was neglected since only the initial transient was considered critical and structural damping would have relatively little effect on the first peak of the transient structural response.

Based on these equations, the tail inertia load was determined for an impulse of 20 lb-sec and a duration of .005 seconds. The values for the masses, lengths, and spring constants used in the analyses are given in figure 3.2-2. The maximum inertia load for the elastic model occurs at .003 seconds, whereas, for the rigid model, the maximum occurs at .0025 seconds (time of peak impulsive force). The tail inertia load and the deflection of the tail as functions of time are given in figures 3.2-3 and 3.2-4.

The dynamic overshoot factor was calculated to be 1.378. The response of the elastic body and the rigid body with an eccentricity of 0.36 inches between the transverse impulse and the center of gravity is shown in figure 3.2-5. This analysis established that the eccentricity had a negligible effect on structural deformation.

### 3.2.2 Structural Test

A program of structural testing was planned for the qualification of the test projectile prior to demonstration firings that consisted of air gun tests, static impulse firings, and range firings with dummy seekers. The limitations of the overall program precluded the execution of this plan. As a consequence, the testing that was conducted represents a relatively small portion of the test effort required for qualification of a test projectile.

Air gun tests were performed to investigate the structural integrity of the seeker head under the axial loading of gun launching. The impulse test firing (only one was conducted) was performed to determine if the test projectile could sustain the transverse impulse loading of control.

#### 3.2.2.1 Air Gun Tests

Tests were conducted at the air gun facility, Frankford Arsenal in which the acceleration was at least 10,000 g. The seeker housing was modified in order to adapt it to the air gun fixture.



Initially, the seeker electronics including power supply were tested. In the first test, the electronics package was severely damaged; the cause of failure, however, was attributed to incorrect assembly prior to insertion in the air gun. Subsequent tests were performed in which the electronics package successfully survived air gunning. This was established by performing functional tests (see Guidance, Section 3.4) with the test samples before and after air gun tests.

The optical element was damaged in three tests that were conducted. In each case, the damage was in the form of fractures along the periphery of the optical head. It was concluded that the bonding material (EK 910) used around the periphery of the optical element created a rigid lock to the supporting band of the seeker housing and caused the glass to fracture under load. To examine this possibility, the method of installing the optical element was modified. A groove was machined in the supporting band. On installation, the optical element was positively seated on a .005 inch teflon spacer and polysulfide base adhesive EC 801 with accelerator ED 1063, Spec MIL-5-11031A, was injected into the machined groove of the supporting band. The assembly was placed into an oven for curing the adhesive (165°F) with the seating pressure being continuously applied. With this modification, an optical head was subjected to two successive air gun tests without sustaining damage.

#### 3.2.2.2 Static Impulse Test

Suspending a test projectile and firing the pulser provides a direct technique for measuring the pulser performance as well as determining the ability of the airframe to withstand the transverse impulse loading. The only test performed was unsuccessful when a pulser, designed to deliver 24 lb-sec of impulse, shattered the aft body adapter in the region of the nozzle. As a consequence, no test data were obtained as to the structural behavior of the test projectile when subjected to this type of impulse loading.

#### 3.2.3 Summary

The test projectile structural design that was developed partially fulfills the given design requirements. The structure is adequate for the expected axial loading of 10,000 g at launch and for the transverse load of inflight control if pulser performance is limited to 20-25 lb-sec impulse. The projectile center of gravity is located 8.7 inches aft of the nose. The pulser nozzle centerline is within 0.1 inches of the center of gravity, as required. The design is slightly overweight (19.4 lbs), however, the target design weight of 18 pounds could be achieved by a design modification. One possibility that had been examined was incorporating the pulser in the seeker head section. This would place the nozzle in the cylindrical portion of the projectile forward of the stop band.

Although the test effort was extremely limited in scope, the results were significant; namely, the POLCAT seeker head with optics, detector, and electronics can function properly after air gunning at 10,000 g.

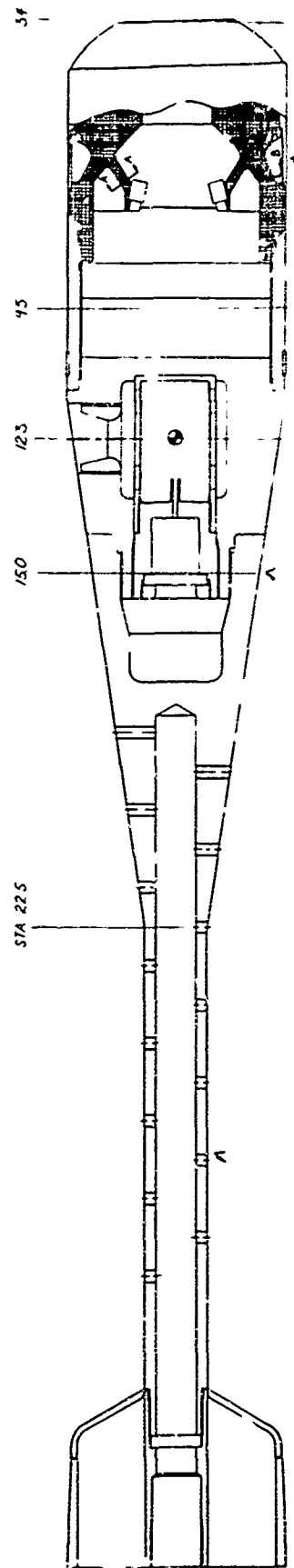


Figure 3.2-1. Assembly Drawing of Test Projectile

Figure 3.2-2 Model for Elastic Analysis

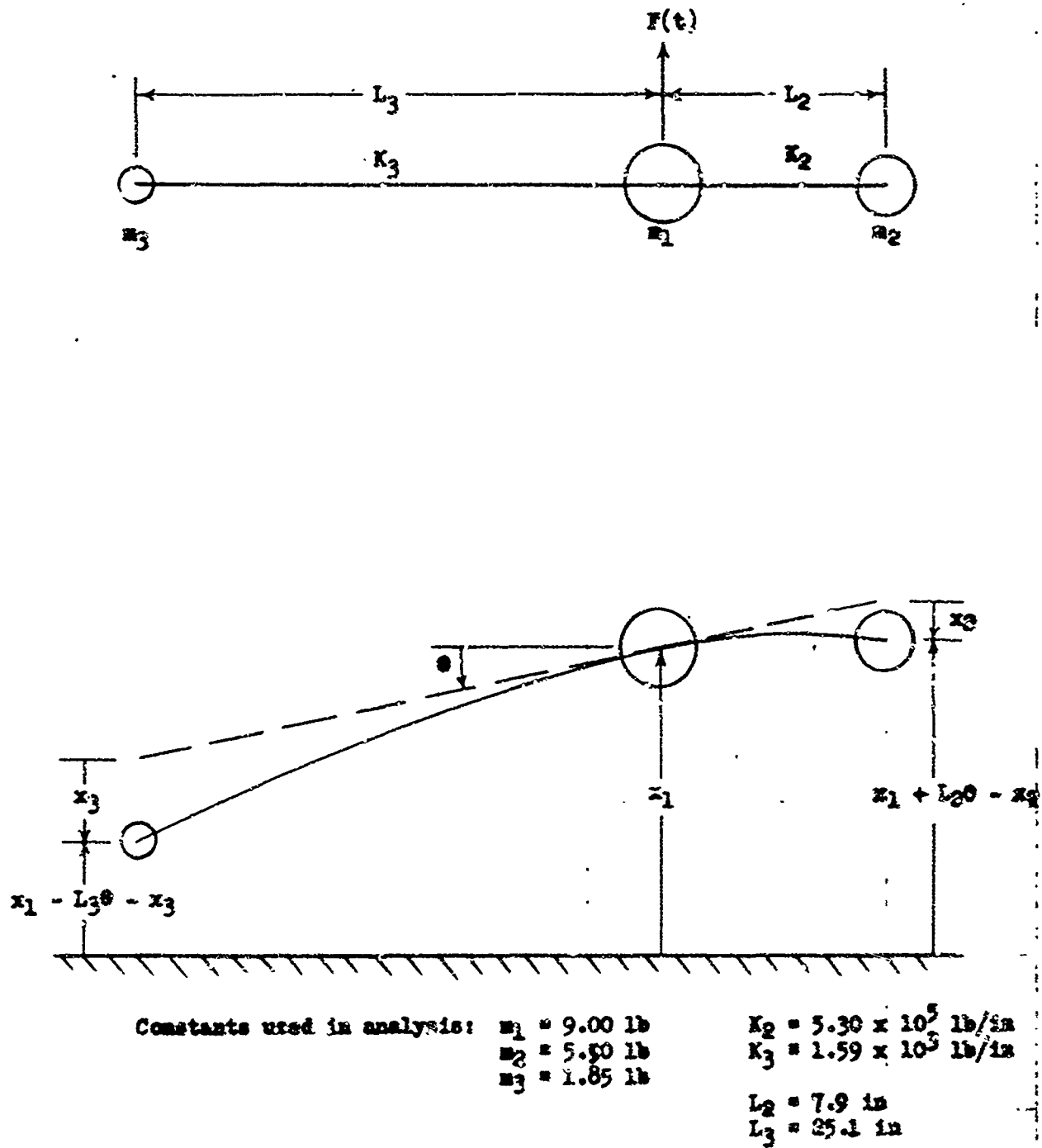


Figure 3.2-3 Estimated Tail Inertia Load vs Time  
Impulse: 20 lb-sec

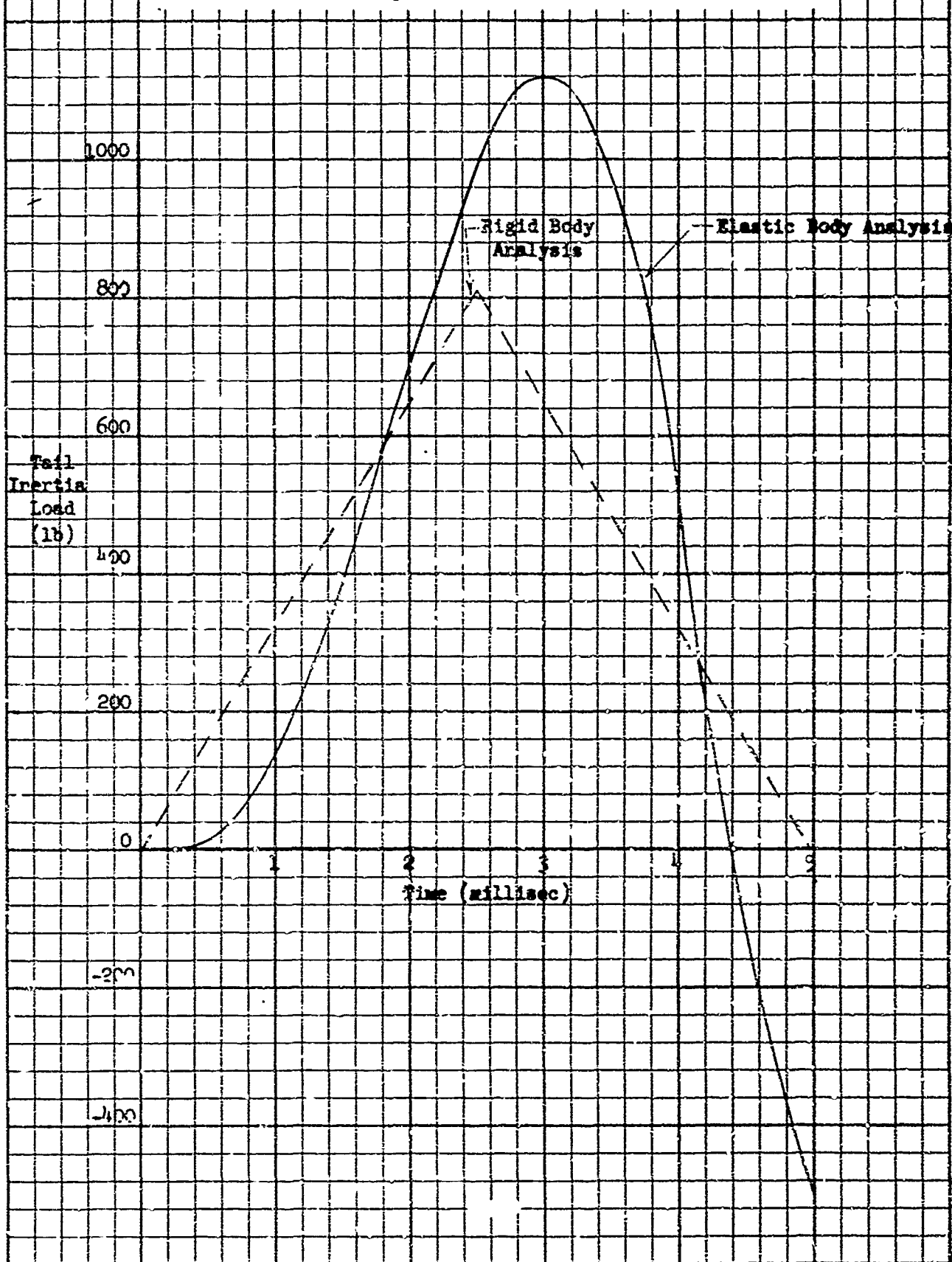


Figure 3.2-4 Estimated Tail Deflection vs Time  
Impulse: 20 lb-sec

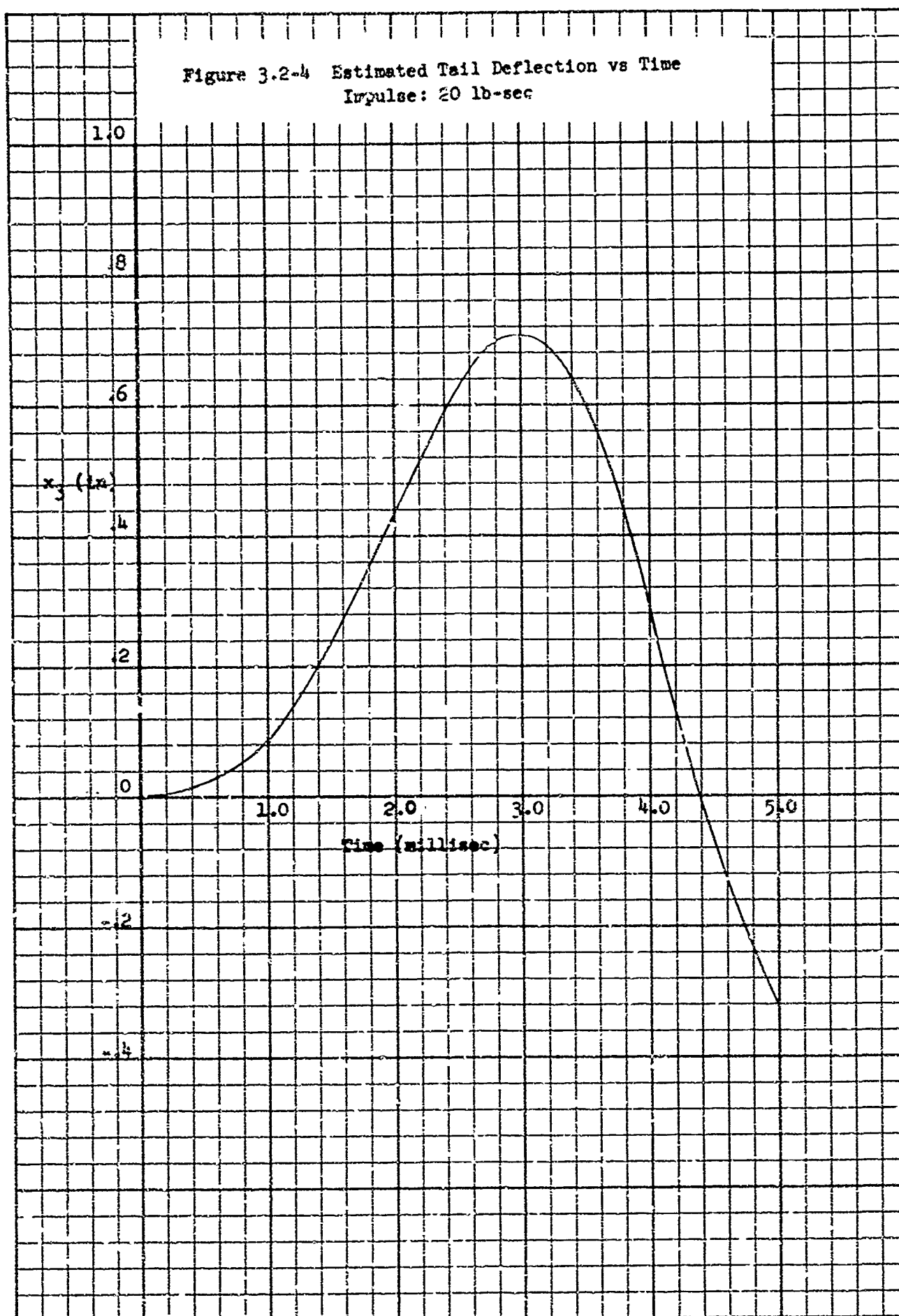
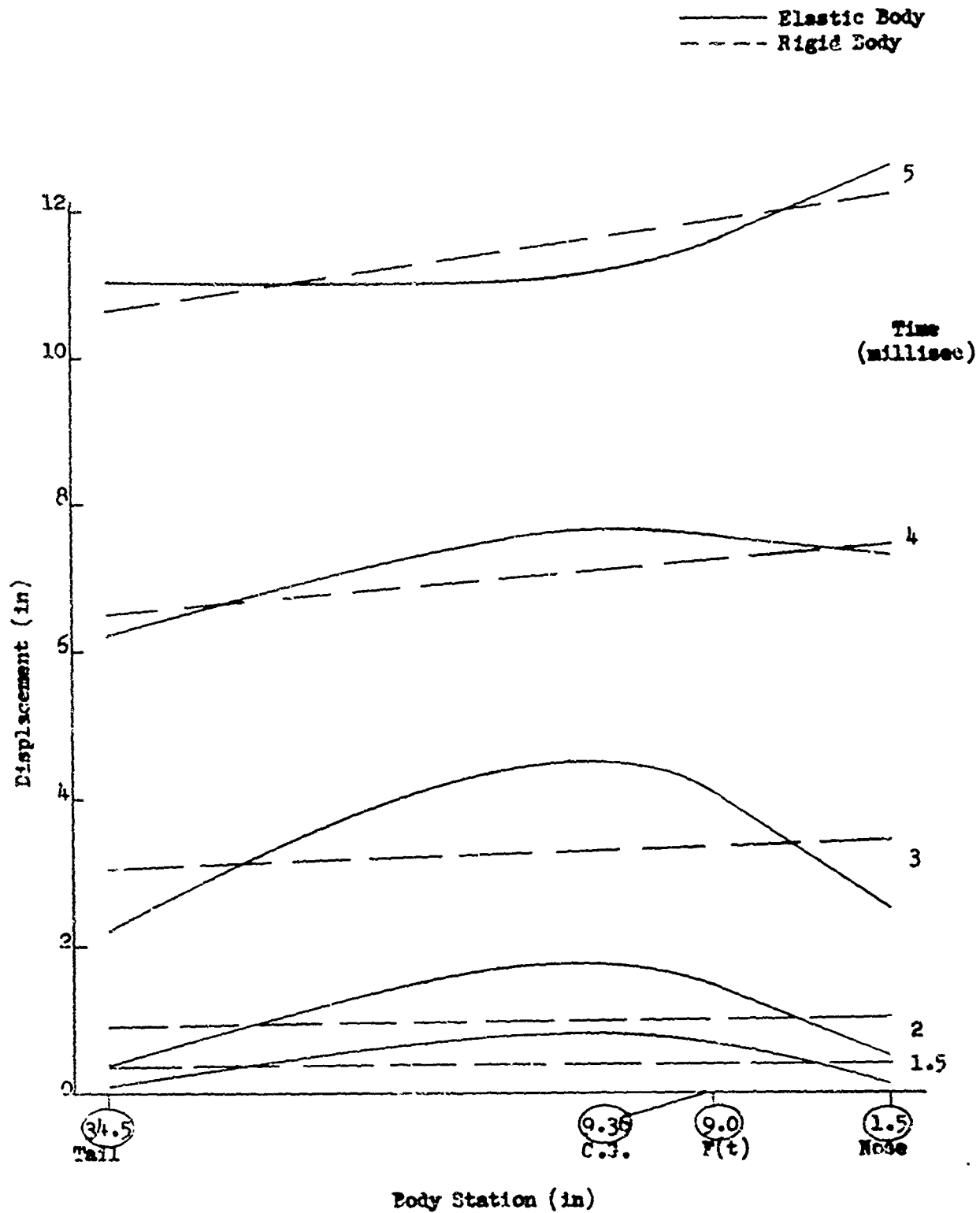


Figure 3.2-5 Comparison of Elastic  
and Rigid Body Response  
Impulse: 20 lb-sec



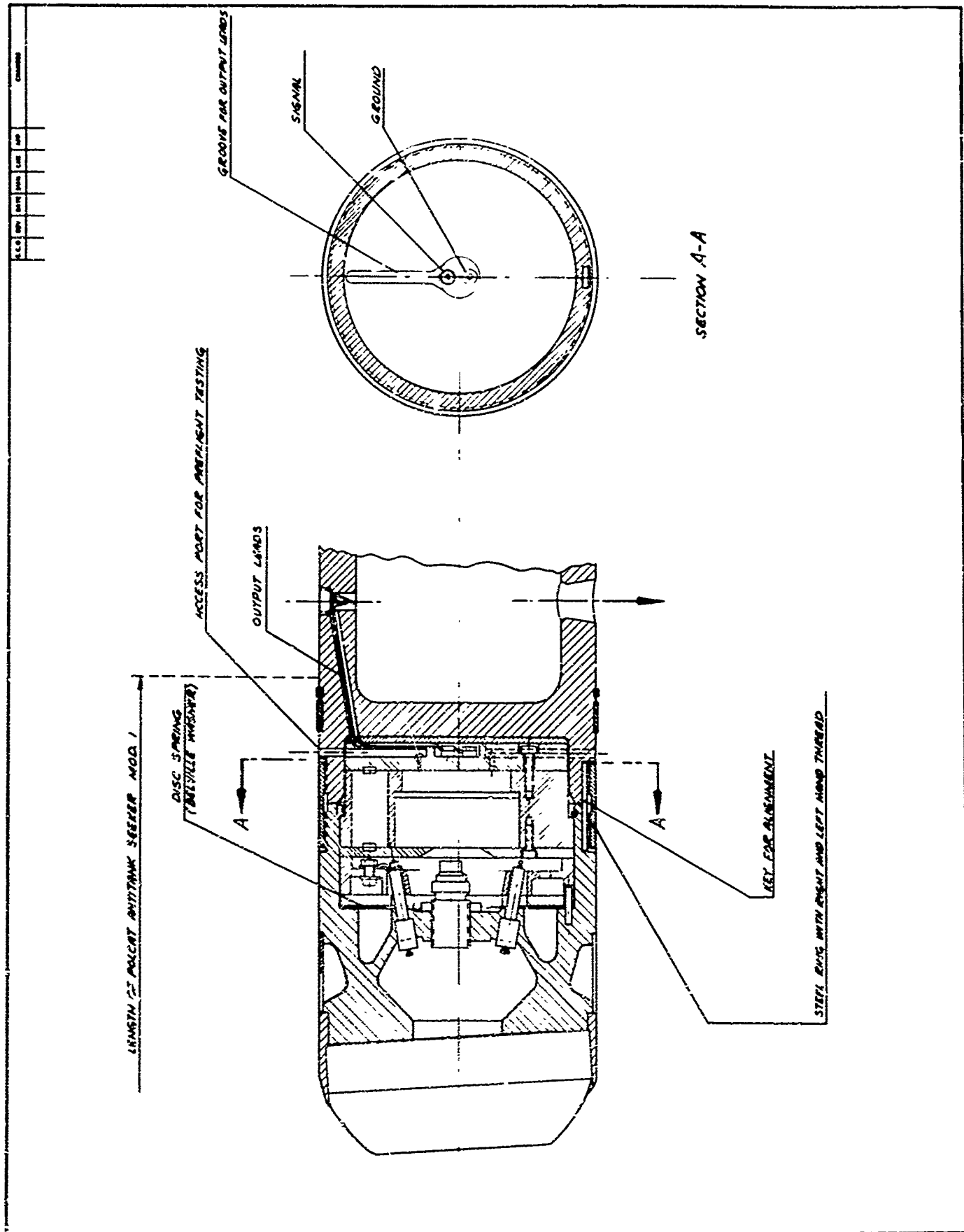


Figure 3.2-6. Assembly Drawing of Seeker Head



### 3.3 CONTROL

The conspicuous feature of the impulse control development was the need to produce a lightweight, reliable pulser unit without the benefit of a well established technology. While the feasibility of utilizing impulse control for projectile flight correction had been previously demonstrated by flight test (1), the success of this earlier effort had been achieved with hardware that delivered relatively low impulse (7.0 lb-sec). As a consequence, a substantial test effort was undertaken to extend the technology by generating basic design and performance data for higher impulse. These data, then, were applied to the development of a pulser capable of fulfilling the specific control requirements of the contemplated flight test demonstration.

The nature and the scope of impulse control development that was conducted is presented as follows; the design effort is described in Section 3.3.1, the test effort in Section 3.3.2, and a summary of results is given in Section 3.3.3.

#### 3.3.1 Design

The limited nature of available experimental data and existing theory had two significant effects on the development plan that was formulated. First, the magnitude of impulse was selected to meet minimum requirements for control of the test projectile during a demonstration firing, recognizing that in a tactical application, larger impulse would be required. Second, an effort to develop and to verify pulser design technology was executed prior to the fabrication of a pulser unit designed to fulfill the requirements of the flight test demonstration.

Consistent with this plan, the following design tasks were undertaken.

- (a) Theoretical analyses were made to establish the range of required design characteristics that would provide desired impulse performance.
- (b) Based on the results of the theoretical analyses, two test fixtures were designed for testing to determine the influence of the critical design parameters on performance.
- (c) The prototype pulser was designed based on the experimental data obtained from test fixture firings.

The following sections describe the specific tasks of the design effort; the internal ballistics study, the control effectiveness analysis, the test fixture design, and the prototype pulser design.

#### 3.3.1.1 Interior Ballistics Analysis

This initial task, undertaken as part of the impulse control development effort, was the analysis of the pulser interior ballistics. The purpose of this study was to establish preliminary design parameters such as chamber volume, propellant weight, and orifice area for the desired control performance characteristics (total impulse, discharge time and peak pressure). At the outset, it was recognized that the ballistics of a pulser were not in all respects representative of those systems for which available theory (2) (3) had been developed. However, the results of the analysis were to be used in the design of test fixtures rather than the design of a prototype pulser. Final pulser

design was to be based on the experimental data obtained from the firings of the test fixtures.

The analysis of pulser performance consisted of estimating the conditions during burning and, then, after burning. The notation used in the equations describing the interior ballistics is given in Table 3.3-1. The assumptions associated with these equations are as follows:

- (1) Constant temperature of gases during burning (this establishes that impetus ( $\lambda$ ) and discharge coefficient ( $K_c$ ) are constant during this period of time).
- (2) Burning rate is proportional to pressure,  $r = BP$  (B may be chosen so that the area under the linear burning rate curve equals that under the exponential burning rate curve,  $r = BP^n$ ).
- (3) The gas flow through the nozzle which converges and, then, diverges, can be treated by the classical one dimensional approach.
- (4) Heat and friction losses are neglected.
- (5) The velocity of the gases in the chamber is zero and no pressure or temperature gradients exist in the chamber.
- (6) Gas discharge through the nozzle is an ideal, adiabatic expansion.
- (7) Mass flow is maximum; sonic velocity exists at the nozzle throat.

Based on these assumptions, expressions were derived for peak chamber

Table 3.3-1 Interior Ballistics Notation

$A_t$	nozzle throat area ( $\text{in}^2$ )
$A_e$	nozzle exit area ( $\text{in}^2$ )
$B$	linear burning rate coefficient ( $\frac{\text{in}/\text{sec}}{\text{lb}/\text{in}^2}$ )
$B'$	exponential burning rate coefficient ( $\frac{\text{in}/\text{sec}}{(\text{lb}/\text{in}^2)^n}$ )
$C$	propellant weight (lb)
$K_c$	sonic discharge coefficient, $\left[ \frac{g_0}{\lambda} \left( \frac{2}{\gamma+1} \right)^{\frac{\gamma+1}{\gamma-1}} \right]^{1/2}$ , ( $\text{sec}^{-1}$ )
$m$	weight of discharged gas (lb)
$N$	weight of propellant burnt (lb)
$p$	chamber pressure ( $\text{lb}/\text{in}^2$ )
$r$	burning rate ( $\text{in}/\text{sec}-\text{psi}$ )
$S$	propellant surface area ( $\text{in}^2$ )
$t_b$	time to peak pressure (sec)
$t_p$	time to pressure decay of .20 of peak pressure (sec)
$V_0$	initial chamber volume ( $\text{in}^3$ )
$V_b$	chamber volume at all-burnt condition ( $\text{in}^3$ )
$W_b$	propellant web (in)
$\phi$	percent charge burnt
$\gamma$	ratio of specific heats
$\psi$	percent discharge of burnt propellant
$\delta$	propellant density ( $\text{lb}/\text{in}^3$ )
$\eta$	covolume ( $\text{in}^3/\text{lb}$ )
$\lambda$	effective mean impetus ( $\text{ft-lb}/\text{lb}$ )

pressure, discharge time, and impulse. The derivations are given in Table 3.3-2.

Using the equations that were developed, the performance of the pulser described below was calculated.

$$A_t = .5 \text{ in}^2$$

$$A_c = .785 \text{ in}^2$$

$$C = 800 \text{ grains (MP SP .016" web propellant)}$$

$$V_c = 0 \text{ in}^3$$

The estimated pulser performance is given below and compared with the experimental results that were obtained during the test firings.

	Estimated	Test
Peak Pressure (psi)	23,800	17,000
Time to Peak Pressure (ms)	3.5 - 6.0	.8 - 1.0
Time from Peak to .2 Peak Pressure (ms)	1.00	1.40
Impulse (lb-sec)	26	24

The difference between the estimated and test values of peak pressure probably results from the assumption, used in calculating peak pressure, that all the propellant burns in the chamber. It is known from current recoilless gun technology that a considerable portion of the unburnt propellant leaves the nozzle before the projectile leaves the gun (5). This results in a decrease in peak pressure and, also, a degressive burning effect which decreases the time to peak pressure. It is likely that a similar effect occurs in the pulser. In addition, time to peak pressure was shown to be significantly affected by the initial

Table 3.3-2 Derivation of Performance Parameters

Peak Pressure

The equation of state for gas in the chamber is,

$$P \left[ V_0 - C(1 - \phi)/\delta - N\eta \right] = 12 N\lambda \quad (1)$$

For a single perforated propellant grain, the burning surface is constant (neglecting end burning) so that the rate of gas generated is only a function of pressure given by,

$$C \, d\phi/dt = \delta S r = \delta S B P \quad (2)$$

Since for single perforated grains,

$$\delta S = 2C/W_b \quad (2a)$$

the percent of propellant burnt can be expressed as,

$$\phi = 2B/W_b \int_0^t P \, dt \quad (3)$$

The gas discharged during burning is given by,

$$m = K_c A_t \int_0^t P \, dt \quad (4)$$

The flow factor, representing that fraction of the gas generated which is discharged, is defined as,

$$f = m/C\phi = K_c A_t W_b / 2BC \quad (5)$$

Using this equation, the gas remaining in the chamber at any time during burning can be expressed as,

$$N = (1 - f)\phi/C \quad (6)$$

Substituting equation 6 into equation 1 gives the chamber pressure as,

$$P = \frac{12 C\lambda(1 - f)\phi}{\left[ V_0 - (C/\delta)(1 - \phi) - C(1 - f)\phi \right]} \quad (7)$$

This expression indicates that pressure increases as  $\phi$  increases, reaching a maximum when all the propellant is burnt ( $\phi = 1$ ). Peak pressure, then, is given by,

$$P_m = 12 C\lambda(1 - f)/V_B \quad (8)$$

Table 3.3-2 (continued)

where  $V_B$  is the effective chamber volume at all-burnt

$$V_B = V_0 - C(1 - \psi) \quad (9)$$

### Discharge Time

The discharge time is considered to consist of two intervals; the time from the start of burning to the all-burnt condition ( $t_b$ ) and the time from all-burnt to a chosen condition of reduced pressure ( $t_f - t_b$ ).

The time to all-burnt ( $t_b$ ) is estimated by assuming the free volume to be constant where, from equation 1, the instantaneous free volume is given by,

$$V_f = V_0 - (C/8)(1 - \phi) - N\eta \quad (10)$$

A constant free volume is set by letting  $\bar{\phi} = 1/2$  represent an average value of  $\phi$  and for an average  $N = 1/2(1 - \psi)\bar{\phi}C$ . With  $\bar{\phi}$  equal to 1/2 (typical value for high-low guns,  $N$  can be given as,

$$\bar{N} = C/8 \quad (11)$$

The free volume becomes,

$$V_f = V_0 - (C/25) - \eta C/8 \quad (12)$$

and the equation of state can be expressed as,

$$P = 12 C \phi \lambda (1 - \psi) / V_f \quad (13)$$

Differentiating equation 13,

$$dP/dt = 12 C \lambda (1 - \psi) / V_f d\phi/dt \quad (14)$$

or,

$$dP/P = 24 C \lambda \psi (1 - \psi) / V_f W_b dt \quad (14a)$$

Integrating equation 14a between the limits  $P_0$  to  $P_B$  and 0 to  $t_b$ , where  $P_0$  is the pressure generated by the igniter, the time to all-burnt is given by,

Table 3.3-2 (continued)

$$t_b = \frac{V_f W_b \ln(P_B/P_0)}{2h C \lambda B(1 - \psi)} \quad (15)$$

In deriving the time from all-burnt to equilibrium, equilibrium is defined as that time when pressure has decayed to .20 peak pressure.

Since the pressure at all-burnt is equal to the peak pressure,

$$P_B = P_m = 12 N_m \lambda / V_B \quad (16)$$

where  $N_m$  is the value of  $N$  at peak pressure,  $N_m = C(1 - \psi)$ .

After all-burnt, the gas discharge rate is given by

$$dN/dt = -V_B dp/dt = K_c (T_m/T)^{1/2} A_t P \quad (17)$$

where the subscript  $m$  denotes the condition at peak pressure.

Assuming frictionless, adiabatic flow of ideal gases,

$$(P/P_m)^{1/\gamma} \quad \text{and} \quad (T_m/T)^{1/2} = (P/P_m)^{\frac{1-\gamma}{2\gamma}} \quad (18)$$

$$dp/dt = (P_m/P)^{-1/\gamma} P_m^{\frac{1-\gamma}{2\gamma}} dp/dt \quad (19)$$

Substituting equations 18 and 19 into equation 17 and integrating between limits  $P_m$  and  $P_e$  ( $P_e = .20P_m$ ) and  $t_b$  and  $t_e$ , the time from all-burnt to equilibrium is given by

$$t_e - t_b = (1/[\gamma - 1])(V_B/A_t)(1/6K_c\lambda) \left[ \left( \frac{P_e}{P_m} \right)^{\frac{\gamma-1}{2\gamma}} - 1 \right] \quad (20)$$

### Impulse

$$I = C_F C/K_c \approx 1.4 C/K_c \quad (21)$$

where the assumed value for thrust coefficient ( $C_F$ ) accounts for the ratio of average chamber pressure to atmospheric pressure and the ratio of nozzle exit area to nozzle throat area.



igniter pressure both in the theoretical calculation and the test firings. However, the magnitude of this effect was not accurately predicted by theory. A reasonable theoretical estimate was obtained for impulse and the time for pressure to decay from peak to a selected, reduced value.

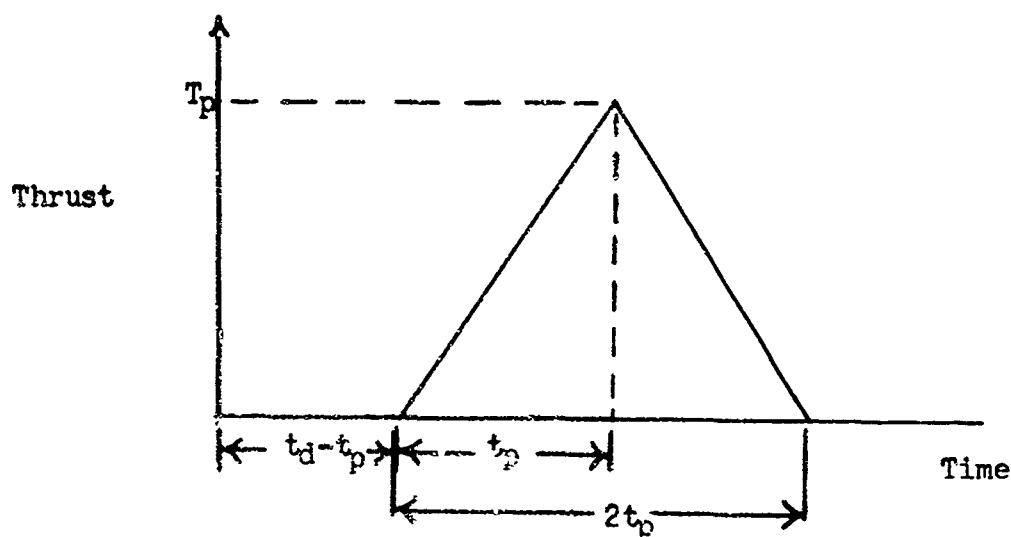
Generally, it can be concluded that the assumed analytical model used for computing pulser performance was not adequate for accurate estimation.

### 3.3.1.2 Control Effectiveness Analysis

The previous section discussed the design parameters associated with the performance of the pulser unit as an impulse generating device. The following discussion is concerned with the performance of the pulser as part of the projectile system. Without fully establishing the interrelationships between the aerodynamics, guidance, and control of the projectile, it is recognized that the aerodynamic properties of the projectile and the functional characteristics of the seeker will determine the choice of projectile spin rate. Therefore, the pulser must be designed to provide the desired impulse control at the established spin conditions. An analysis was performed considering two questions; how effectively does the pulser deliver impulse to a spinning projectile and what are the requirements on pulser discharge time relative to maintaining effective control? The problems associated with projectile pitching motion and control response have been discussed previously in sufficient detail (1) and design solutions established such that consideration here would not contribute any additional understanding.

Since the discharge time of pulser will not be extremely small as compared to projectile spin period, impulse must be examined in terms of a rotating thrust vector that is applied during the control cycle. A measure of control effectiveness, then, is the ratio of the useful impulse delivered to a spinning projectile ( $I_e$ ) as compared to the impulse generated by the pulser ( $I_p$ ). An expression for this "effectiveness" ratio is derived as a function of projectile spin rate ( $\phi$ ) and time to peak thrust ( $t_p$ ).

In deriving the control effectiveness ration ( $I_e/I_p$ ), the thrust-time variation of the pulser is assumed to be triangular shaped. (See sketch below.)



It is to be noted that the time to peak thrust ( $t_p$ ) defines the rise time of pulser thrust. To account for any delays that might occur in ignition,

the time from control system initiation to peak thrust ( $\bar{T}_p$ ) is indicated by " $t_d$ ".

The impulse generated by the pulser is given by,

$$I_p = \int_0^{2t_p} T dt \quad (1)$$

For the assumed thrust-time variation, the integral can be expressed as,

$$I_p = T_p \left[ \int_0^{t_p} (t/t_p) dt + \int_{t_p}^{2t_p} (2 - t/t_p) dt \right] \quad (2)$$

The solution to equation (2) is,

$$I_p = T_p t_p \quad (3)$$

The effective impulse ( $I_e$ ) is defined as the impulse delivered to the spinning projectile in the direction of the peak thrust vector. This quantity is derived by modifying equation (2) so as to account for the instantaneous orientation of the thrust vector throughout the control cycle. (See figure 3.3-1.)

$$I_e = T_p \left[ \int_0^{t_p} (t/t_p) \cos \phi dt + \int_{t_p}^{2t_p} (2 - t/t_p) \cos \phi dt \right] \quad (4)$$

Since projectile spin rate can be assumed to be constant during control, and since it is desired that the effective impulse be determined along the peak thrust vector, the instantaneous angular orientation of thrust can be expressed as,

$$\phi = \dot{\phi}t - \dot{\phi}t_p \quad (5)$$

Substituting equation (5) into equation (4) and integrating, provides a solution for effective impulse.

$$I_e = I_p \left[ \frac{1 - \cos t_p \dot{\phi}}{t_p \dot{\phi}} \right] \quad (6)$$

The control effectiveness ratio can be expressed, then, as a function of time to peak thrust and projectile spin rate.

$$(I_e/I_p) = \frac{2(1 - \cos t_p \dot{\phi})}{(t_p \dot{\phi})^2} \quad (7)$$

$$\text{Since } \cos t_p \dot{\phi} = 1 - \frac{(t_p \dot{\phi})^2}{2} + \frac{(t_p \dot{\phi})^4}{4}$$

$$(I_e/I_p) = 1 - \frac{(t_p \dot{\phi})^2}{12} \quad (8)$$

where  $t_p$  is time in seconds and  $\dot{\phi}$  is spin rate in radians/second.

Figure 3.3-1 shows the variation of the control effectiveness ratio with time to peak thrust for a projectile spin rate of 20 RPS.

On the basis of effective delivery of impulse, it appears that impulse delivery time can be increased to 4 or 5 milliseconds, thereby,

reducing peak chamber pressure, without significantly degrading pulser performance. Generally, it can be concluded that the loss of impulse effectiveness due to spin rate is a relatively minor consideration in the selection of pulser discharge time (as related to pulser rise time). It will be shown in the following section that pulser discharge time has a significant effect on control system error and the selection of this critical time parameter must account for this error.

### 3.3.1.3 Control Error

In order for impulse control to effectively operate in the POLCAT concept, the impulse must be delivered in such a manner that the peak thrust occurs at a specific projectile roll attitude as determined by the seeker. This, theoretically, can be achieved if the roll rate is constant and the time delay associated with seeker-pulser operation is fixed. If both conditions are not fulfilled, the impulse will be delivered out of the control plane by a polar angle defined as  $\Delta\phi$ . This error is related to the variations in roll rate and time delay as follows.

$$\Delta\phi = \Delta\dot{\phi} t_d + \Delta t_d \dot{\phi} \quad (9)$$

The magnitude of the miss distance ( $d_m$ ) at the target directly attributed to this control error is a function of the magnitude of impulse or angular projectile correction ( $\gamma$ ), and the range to the target at the time of control ( $r$ ).

$$d_m = \Delta\phi r \gamma \quad (10)$$

At this time, it is known that roll rate will vary but that the variation in time delay ( $t_d$ ) will be small. Thus, calculations were made

assuming that the total polar angle error ( $\Delta\phi$ ) was caused only by roll rate variation. The relation between the total time to peak thrust ( $t_d$ ), miss distance at the target ( $d_m$ ), and target range ( $r$ ) is given in figure 3.3-2. The following conditions were assumed:

Projectile roll rate ( $\dot{\phi}$ ): 20 RPS

Variation in roll rate ( $\Delta\dot{\phi}$ ): 3 RPS

Impulse control angle ( $\delta$ ): 0.05 rad

It is to be noted that these results cannot be directly applied to the final selection of pulser discharge time until the statistical distributions for  $r$  and  $\Delta\phi$  are determined and the resulting error due to control is combined with other system errors. However, a preliminary estimate of allowable delay time was made based on available trajectory data. These data indicate that for a correction angle ( $\delta$ ) of 0.05 radians, the 3 $\sigma$  value of target range ( $r$ ) at the time of control is approximately 300 feet, and the 3 $\sigma$  value of roll rate variation ( $\Delta\dot{\phi}$ ) is approximately 3 RPS at target ranges of 1500 meters. For these conditions, the maximum miss distance (3 $\sigma$ ) caused by this specific function can be limited to 1.5 feet if delay time ( $t_d$ ) does not exceed 5 milliseconds.

#### 3.3.1.4 Test Fixture Design

Based on the design studies described in the preceding sections, the preliminary control performance requirements were set at 20-35 lb-sec of impulse to be delivered within .003 seconds. Further, it was estimated that the desired performance could be obtained by the range of design parameters given below.

Peak Pressure: 20,000-30,000 lb/in<sup>2</sup>  
Chamber Volume: 9-13 in<sup>3</sup>  
Nozzle Throat Area: .3-.7 in<sup>2</sup>

Two test fixture designs, both suited to eventual incorporation within the test projectile, were established. Each design provided for changing nozzle throat area (.3, .5, and .7 in<sup>2</sup>) and chamber volume (9 and 13 in<sup>3</sup>).

Test Fixture No. 1, as shown in figures 3.3-3 and 3.3-4, contained a simple bottle type chamber with the axis of the cylindrical chamber coinciding with the nozzle axis. Chamber volume was varied by installing a sleeve.

Test Fixture No. 2, as shown in figures 3.3-5 and 3.3-6, placed the nozzle axis perpendicular to the axis of the cylindrical chamber. Chamber volume was varied by two end plugs.

#### 3.3.1.5 Prototype Pulser

The design of the prototype pulser utilized the internal geometry of Test Fixture No. 2 since this design could be more readily incorporated within the test projectile by modifying the boattail section of the XM419 projectile. This is shown in figure 3.3-7. By placing the pulser chamber in the aft body adapter, the axis of the nozzle passed through the center of gravity of the test projectile transverse to the longitudinal axis. The pulser section maintained the same boattail angle of the XM419 projectile and was designed to mate with the tail boom adapter of the projectile. The seeker section was mounted on the forward portion of the pulser section.

The mass and dimensional characteristics of the pulser capable of delivering 24 lb-sec of impulse are given below.

Weight	5.3 lb
Chamber Volume	9.0 in <sup>3</sup>
Nozzle Throat Area	0.5 in <sup>2</sup>
Propellant:	
Type	M5 SP .021" web
Weight	885 grains

Initial test fixture firings established that M2 SP .016" web propellant consistently provided the desired impulse with a time of 1.0 millisecond to peak pressure. However, the prototype pulser failed structurally in a test with the M2 propellant. As a consequence, the slower burning M5 propellant with a larger web is recommended for use with this design although the time to peak pressure is longer (1.5 milliseconds).

### 3.3.2 Test

The test program executed as part of the impulse control development consisted of 150 firings with the two test fixtures and the prototype pulser. These tests were conducted in two series. The first series of tests were conducted to determine the fundamental relationships between pulser design parameters and performance, and are described in Section 3.3.2.1, Test Fixture Firings. The second series of tests were conducted to establish the performance of a specific pulser design. These tests are described in Section 3.3.2.2, Pulser Qualification Firings.

The data obtained during this test program and the previous pulser development (4) were analyzed and an empirical expression for relating chamber volume, nozzle throat area, peak chamber pressure, time to peak pressure,



and impulse delivered, was developed. The empirical relationship which could be extremely useful in future pulser development work is given in figure 3.3-8.

#### 3.3.2.1 Test Fixture Firings

Initially, firings were conducted with Test Fixtures No. 1 and No. 2 with 9 in<sup>3</sup> and 13 in<sup>3</sup> chambers to determine the effect of nozzle area and ignition system on impulse performance. Then, firings for charge establishment were conducted with Test Fixture No. 2. All firings were made at ambient temperature. The results are presented in Tables 3.3-3 and 3.3-4. Pressure data were obtained from a piezo electric gauge and impulse was measured by pendulum displacement.

Due to instrumentation difficulties in the initial firings, few usable thrust records were obtained with the load cell. Consequently, the magnitude of the impulse delivered to the system could not be determined accurately. A special pendulum was constructed to permit direct measurement of impulse. Recoil was measured by means of an electronic water-bath system. Load cell records were taken, concurrently, with the recoil to serve as a comparison.

#### 3.3.2.2 Pulser Qualification Firings

The prototype pulser was tested in an assembled test projectile (dummy seeker head) with an 800 grain charge of M2 SP .016" web propellant. The purpose of this test was to determine whether the test projectile, particularly the tail boom adapter, could sustain the impulse loading of control as well as test the performance of the pulser. The firing of the pulser shattered the projectile aft section (pulser chamber) in a manner

Table 3.3-3 Test Firing Data - Design Investigation

Propellant: M2 SP .016" web

No of Rds	Charge (grains)	Chamber Volume (in <sup>3</sup> )	Throat Area (in <sup>2</sup> )	Ave. Peak Pressure (lb/in <sup>2</sup> )	Ave. Time to Peak (millisec)	Average Impulse (lb-sec)
Test Fixture No. 1						
2	800	9	.5	24,000	1.0	19.4
1	800	9	.5	17,200	.8	22.0
3	800	9	.7	15,100	.7	17.3
3	800	9	.3	36,700	.8	21.3
Test Fixture No. 2						
2	500	9	.5	8,700	1.0	13.9
3	800	9	.5	21,000	.9	20.6
3	800	9	.7	14,700	.8	18.5
3	800	9	.3	28,200	.8	20.0
5	1200	13	.7	22,000	1.0	31.8
6	1200	13	.5	26,000	1.0	33.0
1	1200	13	.3	35,000	1.0	34.0
10	820	9	.5	20,000	1.0	23.4
9	820	9	.3	31,000	1.0	26.0

Table 3.3-4 Test Firing Data - Charge Establishment

Test Fixture No. 2: Chamber Volume - 9 in<sup>3</sup>  
 Nozzle Throat Area - .5 in<sup>2</sup>  
 Time to Peak Pressure - 1.0 millisecond

Propellant: M2 SP .016" web

No of Rds	Charge (grains)	Average Peak Pressure (psi)	Average Impulse (lb-sec)
Aluminum Cartridge Cases			
5	800	17,500	24.7
4	900	27,300	27.3
5	1000	29,200	33.0
4	820(a)	13,000	22.4
1	800(b)	15,000	25.2
1	900(b)	29,000	29.2
Modified Aluminum Cartridge Cases with Steel Sleeves			
3	400	3,500(c)	10.0
2	600	7,300	16.7(c)
3	800	17,000	22.3
3	900	23,500	22.7

- (a) Cardboard cartridge case
- (b) Aluminum nozzles
- (c) Only one measurement recorded

that indicated detonation of the propellant. See figure 3.3-9.

Investigations were, then, performed to determine the cause of failure. During the test fixture firings, the M2 propellant ignited by the T20F1 detonator had consistently developed peak pressure within 0.8-1.0 milliseconds and, as a consequence, it was believed that actual dynamics of the pressure rise in this short time period had not been fully accounted for. This was confirmed by subsequent stress analyses which indicated that the measured peak pressures could not possibly cause failure of any pulser components. This led to the conclusion that unequal pressures existed in the chamber during the pressure rise causing a rupture at some critical point in the chamber, thereby initiating complete failure of the structure.

Firings were conducted with Test Fixture No. 2 instrumented to measure pressure at the end of the chamber opposite the detonator (Sta. B) and at the center of the chamber (Sta. C). These data shown in Table 3.3-5 substantiated the theory that a significant pressure difference existed in the chamber in firings with M2 propellant.

To reduce peak pressure, the larger web M5 propellant was used in test firings. The results presented in Table 3.3-5 indicate a pressure reduction; however, this is accompanied by a wide and undesirable variation in impulse delivered.

Curtailement of the test program precluded determination of the true cause of prototype pulser failure.

### 3.3.3 Summary

The most significant achievement of the pulser development effort was the establishment of basic experimental data relating the design

Table 3.3-5 Test Firing Data - Propellant Study

Test Fixture No. 2:  $V_0 = 9 \text{ in}^3$   $A_t = .05 \text{ in}^2$

Round	Charge (grains)	Peak Pressure (psi)		Impulse (lb-sec)	Propellant	
		Sta. B	Sta. C		Type	Web
101	800	17020	12060	27.0	M2	.016"
102	800	19780	13860	24.8	M2	.016"
103	800	15970	12130	27.0	M2	.016"
104	885	8730	7880	22.5	M5	.021"
105	885	8350	7880	23.4	M5	.021"
106	800	5600	5910	18.0	M5	.021"
107	800	4670	6070	18.0	M5	.021"
108	800	--	--	20.3	M5	.019"
109	800	6780	6040	15.8(a)	M5	.019"
110	800	7130	8560	13.5(a)	M5	.019"
111	885	6700	3500	13.5(a)	M5	.021"
112	800	6620	5460	13.5(a)	M5	.021"
113	885	8680	6880	26.6	M5	.021"
114	885	--	--	27.0	M5	.021"
115	885	8930	8540	27.0	M5	.021"
116	885	8880	8270	22.5	M5	.021"
117	885	9470	8560	22.5	M5	.021"
118	885	9670	8700	22.5	M5	.021"
119	885	9270	8140	22.5	M5	.021"

(a) questionable measurement

characteristics and the performance of this type of hardware. A pulser design capable of generating 20 to 25 lb-sec of impulse has been established although additional qualification testing is required with instrumentation better suited to the design goals of POLCAT impulse control systems.

The interior ballistics analysis indicated that pulser impulse can be estimated theoretically with an accuracy that is acceptable for the purposes of preliminary design. This was not the case in the estimation of peak chamber pressure and discharge time. Apparently, these performance parameters are extremely sensitive to the particular conditions associated with pulser ignition and thus, the simplifying assumptions that were made, preclude their accurate estimation.

The data obtained from the test firings revealed the most significant deficiency of the overall control development effort: the lack of adequate instrumentation. The available load cell instrumentation was not sufficiently reliable and the pendulum measurement systems were not sufficiently accurate.

In view of the POLCAT system requirement for the accurate delivery of impulse, it appears that the first consideration of any future control system development should be the acquisition of suitable test instrumentation.

Figure 3.3-1 Control Effectiveness Ratio

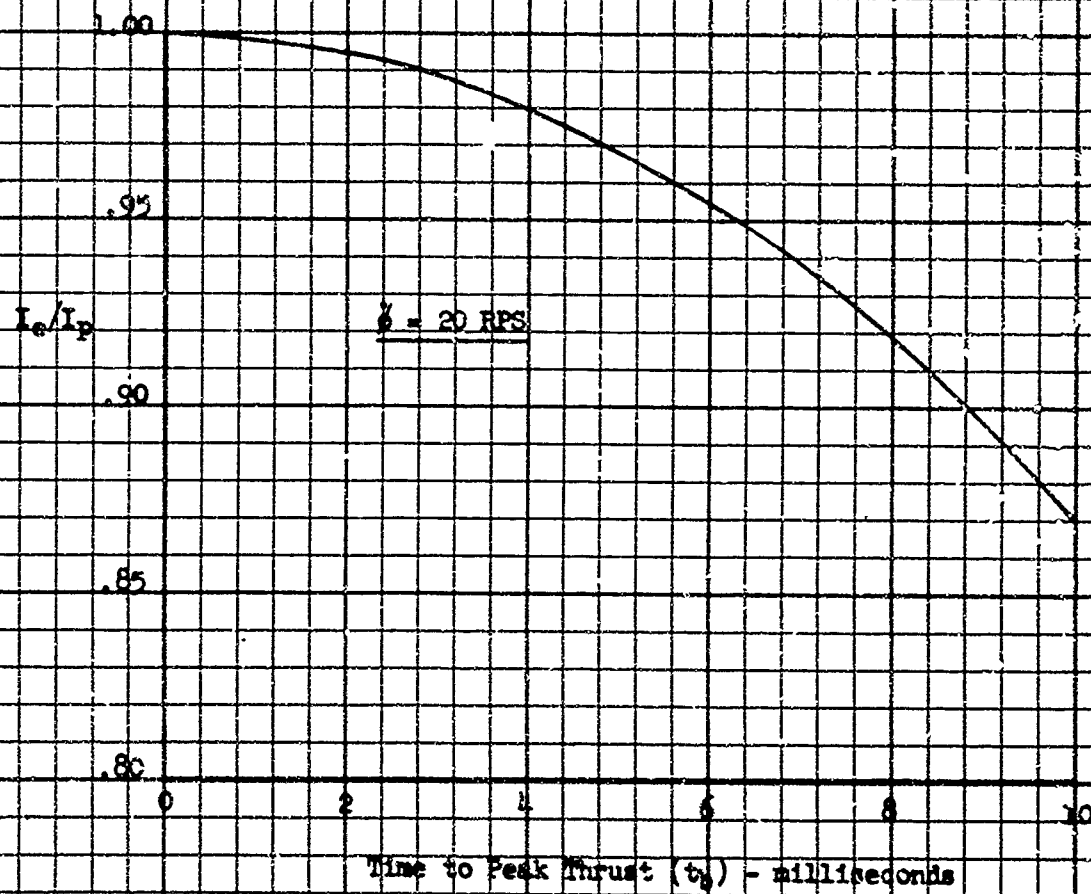
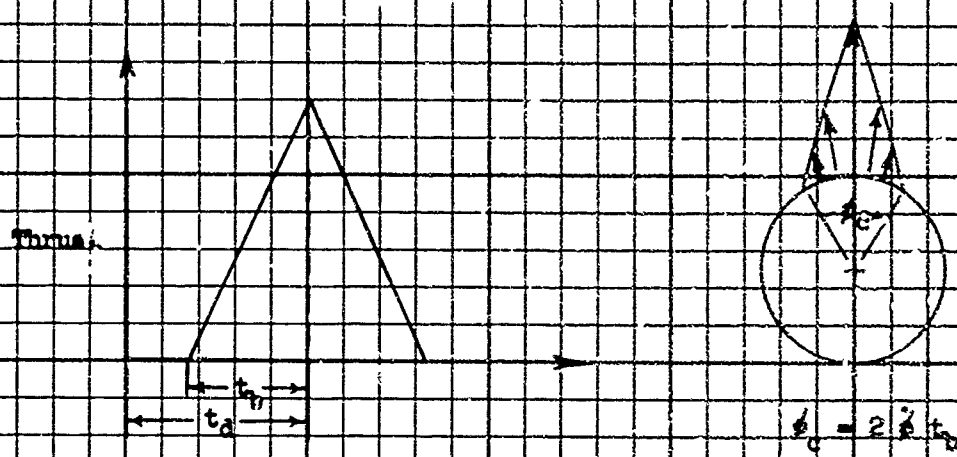
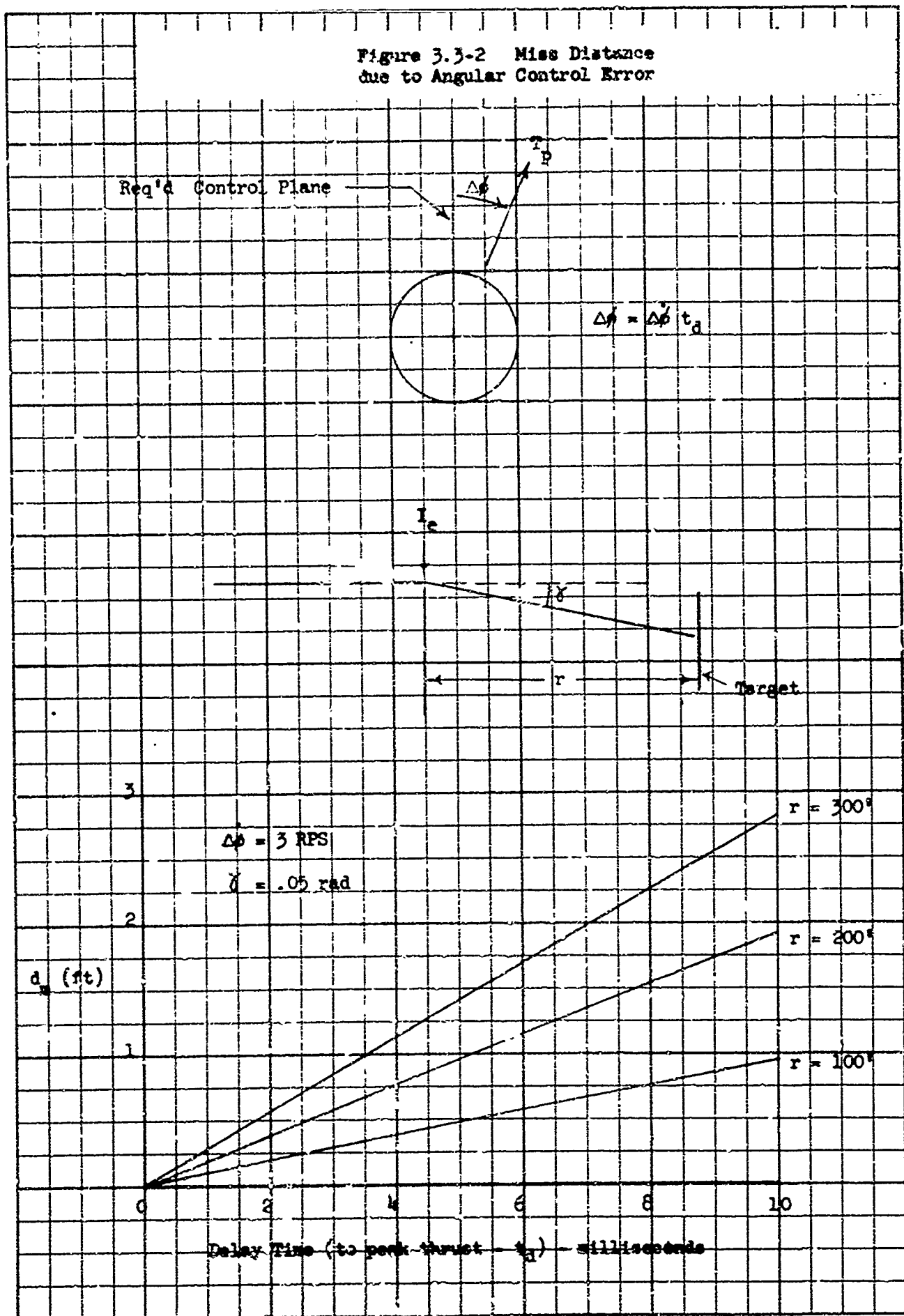


Figure 3.3-2 Miss Distance  
due to Angular Control Error





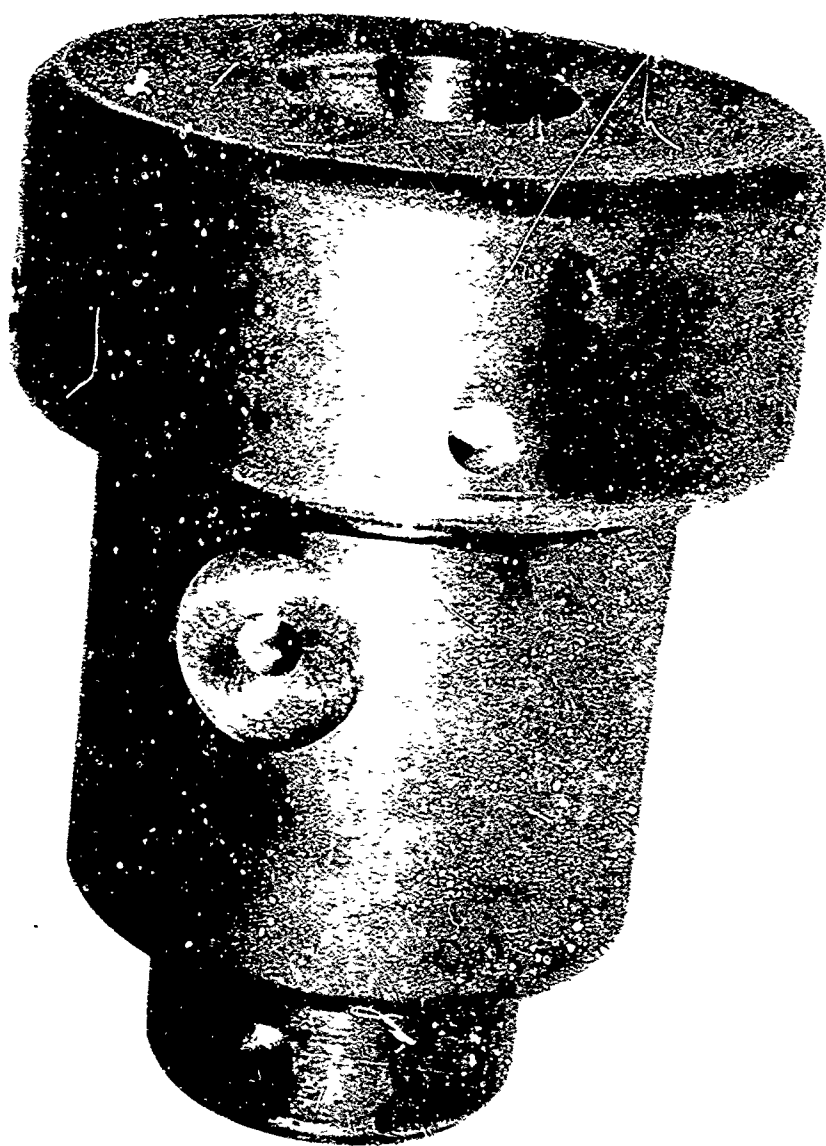
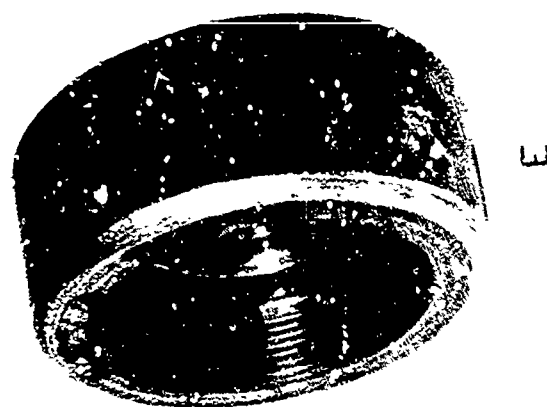


Figure 3.3-3. Test Fixture No. 1 - Assembly



D - Blowout  
disc  
E - Nut

A - Body  
B - Sleeve  
C - Nozzle

Figure 3.3-4. Test Fixture No. 1 - Exploded View

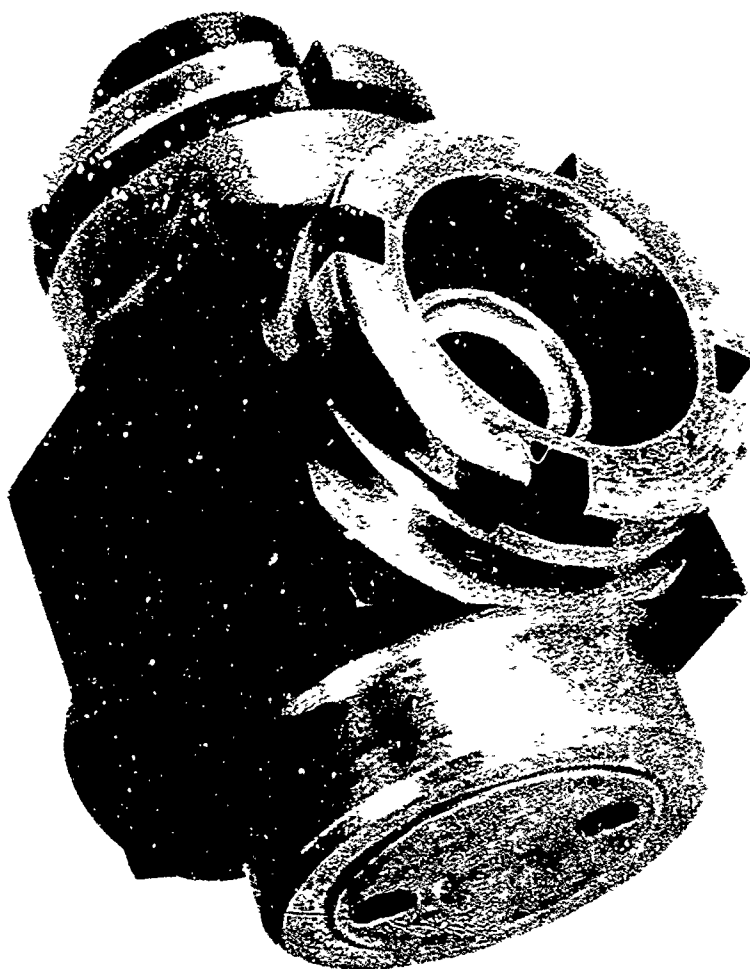


Figure 3, 3-5. Test Fixture No. 2 - Assembly

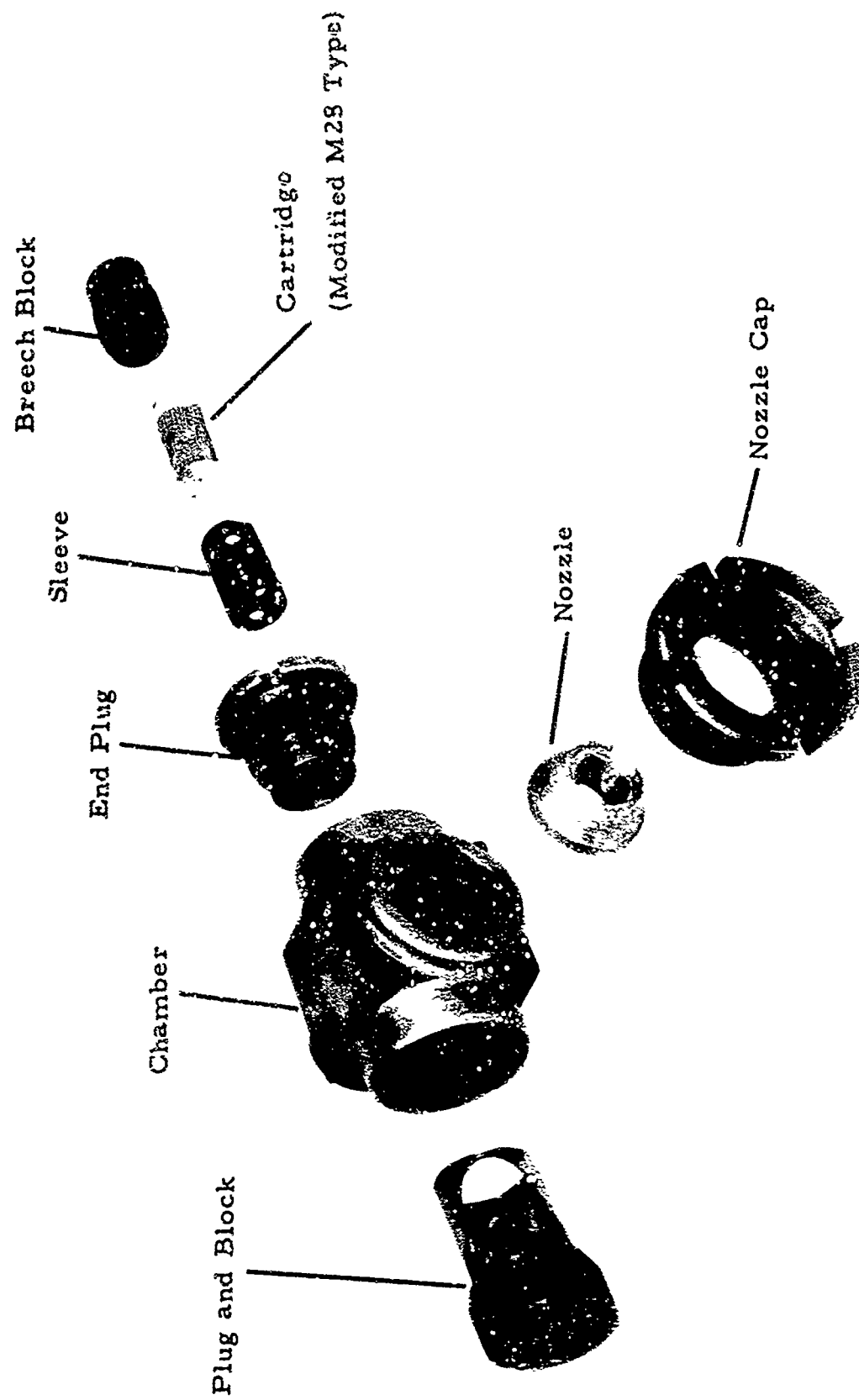


Figure 3.3-6. Test Fixture No. 2 - Exploded View

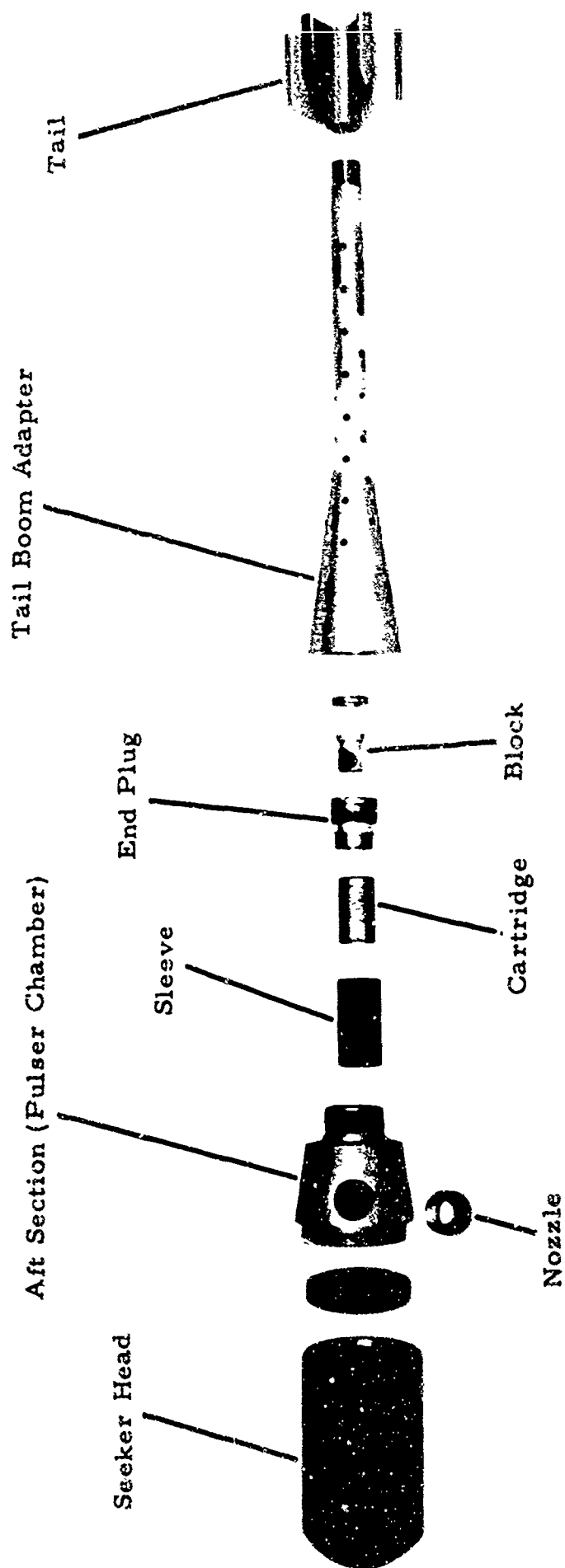


Figure 3.3-7. Test Projectile with Pulser - Exploded View

Figure 3.3-8 Empirical Relationship for  
Impulse and Pulsar Design Parameters

A = throat area (in<sup>2</sup>)  
V<sub>0</sub> = chamber volume (in<sup>3</sup>)  
P = peak pressure (psi)  
t = time to peak pressure (ms)  
I = impulse (lb-sec)

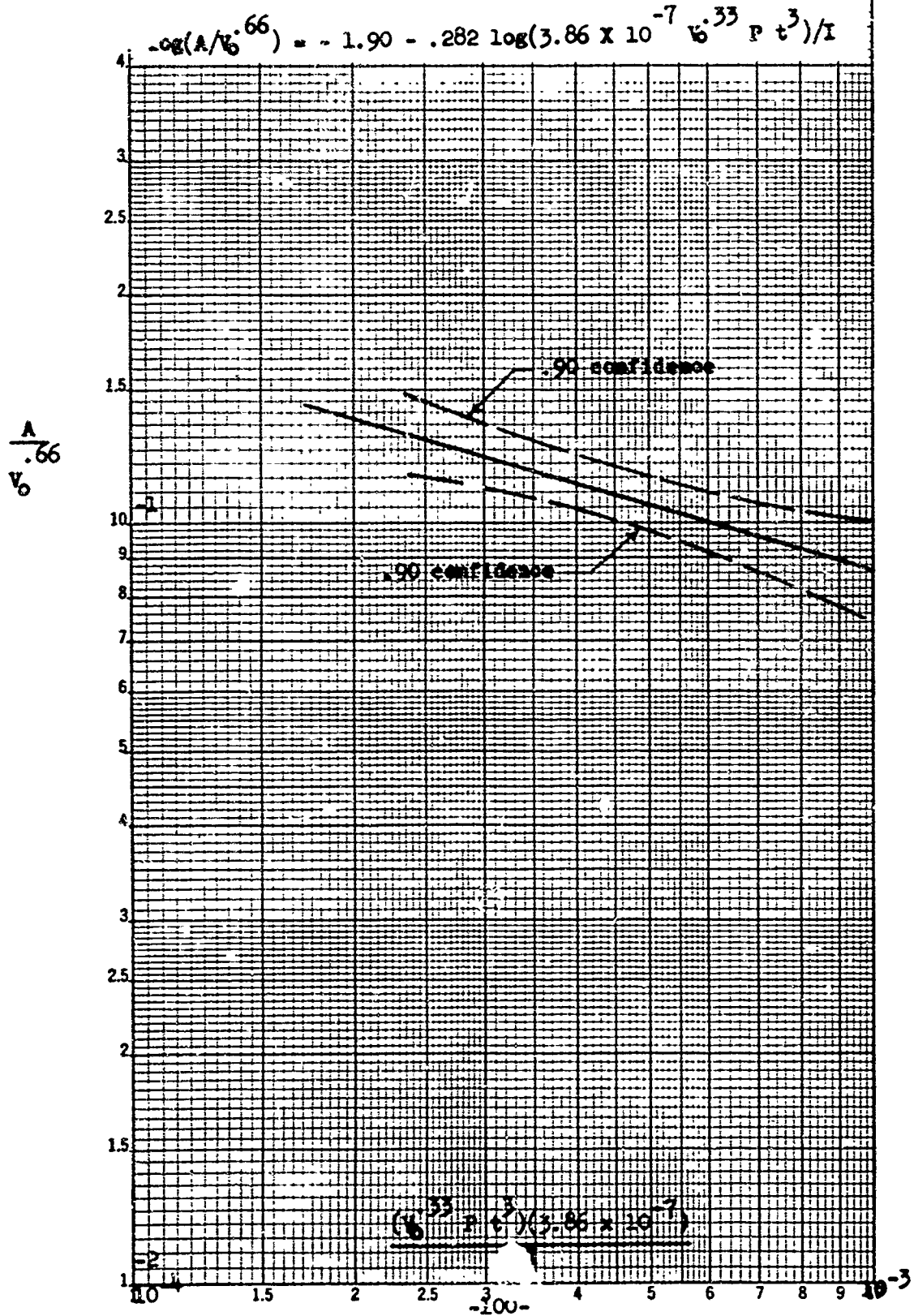




Figure 3.3-9. Test Projectile after Pulser Firing

### Control References

1. Fenton, S. J.: Feasibility Study of an Advanced Recoilless Rifle Weapon System Utilizing a Terminally-Guided Projectile. Frankford Arsenal Report R-1425, Dec. 1, 1957.
2. Vinti, J. P. and Kravitz, S.: Theory of the Transient State of a Rocket Motor or a High-Low Pressure Gun. BRL Report 772, Dec. 1951.
3. Corner, J.: Theory of the Interior Ballistics of Guns. John Wiley and Sons, Inc., 1950
4. Fulton, C. L.: A Reaction Thrust Generator for Projectile Guidance and Possible Missile Guidance. Frankford Arsenal MR-689, 1958
5. Development of 105mm Battalion Antitank Weapons and Interior Ballistics for the Design of Recoilless Rifles. Armour Research Foundation, Summary Report, Volume I ARF Project No. L034, July 1954.



### 3.4 GUIDANCE

The development of a POLCAT homing link was directed toward the fulfillment of two primary objectives;

- (a) the development of a seeker-illuminator combination capable of providing an adequate guidance signal for the target seeker under test firing conditions, and
- (b) the development of a seeker capable of performing its intended function after being subjected to the high accelerations of gun launching.

Accordingly, design studies, laboratory tests, and field test measurements were conducted to establish basic design data and to qualify the hardware that was fabricated. The following discussion describes these efforts and, in addition, presents a guidance analysis that was prepared specifically for this report.

Section 3.4.1, Guidance Analysis, considers the semi-active guidance technique used in the POLCAT concept in the light of communication theory. The analysis defines the optimum receiver, the advantages of coding, and the relation of signal recognition and false alarm probabilities to signal-to-noise ratio (SNR).

Section 3.4.2, Noise Analysis, discusses the various types of noise that must be considered in homing link design.

Section 3.4.3, Signal Analysis, describes the illuminator that was developed and the effects of the atmosphere and target reflectivity on the guidance signal.

Section 3.4.4, Seeker Design, presents the characteristics of the seeker that was developed. Finally, the field tests that were conducted with the seeker are described in Section 3.4.5.

Table 3.4-1 Guidance Notation

A	amplitude of voltage pulse (volt)
$A_d$	area of detector ( $\text{cm}^2$ )
b	threshold level (volt)
c	velocity of light ( $3 \times 10^{10}$ cm/sec)
C	capacity (farads)
D	diameter of entrance pupil of transmitting optic (cm)
$D^*$	detectivity ( $\text{cm cps}^{1/2}/\text{watt}$ )
E	energy of received signal (watt-sec)
f	frequency of signal (cycle/sec)
$f(t)$	input function of time (volt)
$\Delta f$	measurement bandwidth (cycle/sec)
$f_s$	scan rate (cycle/sec)
$g(t)$	output function of time (volt)
h	Planck's constant ( $6.62 \times 10^{-34}$ watt-sec/deg)
$h(t)$	impulse response (volt)
$H_{\lambda}$	spectral incidence at receiver due to target signal (watt/ $\text{cm}^2$ -micron)
I	current (amp)
$I_0$	average bias current (amp)
k	Boltzmann Constant ( $1.38 \times 10^{-23}$ joules/deg $^\circ$ )
$k_x, k_y$	transform variables (cycle/radian)
L	path length (cm)
$I_{10}$	loss involved in mistaking a signal for noise
$I_{01}$	loss involved in mistaking noise for signal

$M$	effective aperture of receiver ( $\text{cm}^2$ )
$n$	number of samples
$n$	minimum number of sequel pulses
$N$	mean squared noise ( $\text{volt}^2$ )
$\bar{N}$	average total number of free carriers
$\bar{N}_{\text{BL}}$	average rate at which photons are reflected by a unit area of background into a normal unit solid angle per unit wavelength interval at $\lambda$ microns ( $/\text{cm}^2\text{-steradian-micron}$ )
$\bar{N}_{\text{TA}}$	average rate at which signal photons arrive at a unit area of receiver per unit spectral interval
$P_1$	a priori probability that a signal will be present
$P_0$	a priori probability that there will be no signal
$p_1(v)dv$	conditional probability density corresponding to the probability of receiving voltage $v$ if a signal was present
$p_0(v)dv$	conditional probability density corresponding to the probability of receiving voltage $v$ if there is no signal
$p(v)dv$	probability that voltage $v$ will fall in a region $v \pm dv/2$
$P(1/v)$	probability that given a particular value of $v$ , a signal was present
$P(0/v)$	probability that given a particular value of $v$ , there was no signal
$P_{\text{BL}}$	spectral power in the beam ( $\text{watt/micron}$ )
$r_\lambda$	coefficient of diffuse spectral reflectivity ( $\text{micron}^{-1}$ )
$R$	resistance ( $\text{ohm}$ )
$R$	equivalent input resistance
$R_{\text{T-R}}$	distance between target and receiver ( $\text{cm}$ )
$\text{SNR}$	ratio of signal energy to noise spectral density
$t$	time ( $\text{sec}$ )
$t_\lambda$	spectral transmissivity of air path ( $\text{micron}^{-1}$ )

$T$	absolute temperature ( $^{\circ}$ Kelvin)
$v_j$	jth voltage sample (volt)
$V_n$	wind velocity (cm/sec)
$V$	visual range (km)
$w$	precipitable water (mm)
$w_{T\lambda}$	spectral sterance of background (watt/cm <sup>2</sup> -steradian-micron)
$w_{s\lambda}$	spectral sterance of source (watt/cm <sup>2</sup> -steradian-micron)
$X, Y$	angular dimensions of scanned area (radians)
$\alpha$	pitch angle (degree)
$\epsilon$	optical beam width (radian)
$\eta$	noise spectral density (watt/cycle/sec)
$\theta_v, \theta_H$	angular dimensions of instantaneous field of view (radian)
$\theta_c$	line of sight angle: average radius of scan annulus (radian)
$\lambda$	wavelength (cm, micron)
$\lambda_c$	wavelength at the midpoint of a spectral interval of interest (micron)
$\Delta\lambda$	wavelength interval (micron)
$\eta_\lambda$	spectral efficiency of transmitter (micron <sup>-1</sup> )
$\eta_\lambda$	spectral quantum efficiency (micron <sup>-1</sup> )
$\nu$	photon frequency (cycle/sec)
$z$	distances between diaphragms (cm)
$\sigma$	variance
$\phi_c$	angular tolerance on corrective impulse measured about spin axis (degree)
$\omega$	frequency (radians/sec)

### 3.4.1 Guidance System Analysis

The elements of a semi-active guidance system are indicated in the block diagram below.



Figure 3.4-1

The received signals are attenuated by the atmosphere and scattered by the target. In addition the receiver must process extraneous fluctuations due to random effects in the transmitter, channel and receiver, and interactions between them. In general, the receiver has two functions; first, it must decide whether it is receiving a signal plus noise or noise alone and, second, it must decide which of all possible signals that could have been transmitted was indeed sent. Figure 3.4-2 shows the general case for a single transmitted signal.

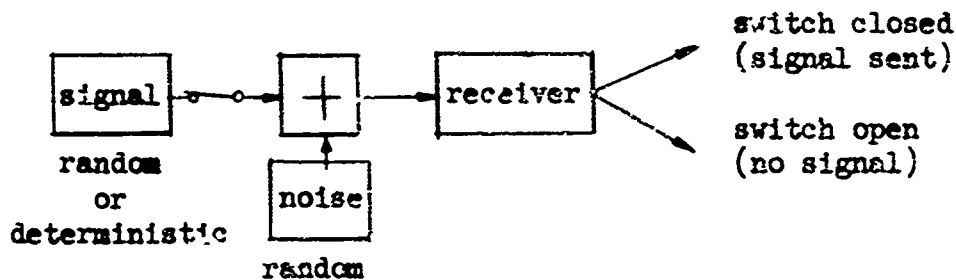


Figure 3.4-2

If the receiver decides that the switch was closed when actually it was open, this represents a false alarm. On the other hand, if the receiver does not recognize when the switch closed, this is a miss. It will

be shown that the a priori requirements for the false alarm probability and recognition probability establish the energy required in the signal.

Systems in which the receiver can determine the phase of the transmitted signal, and hence tell whether a signal  $f(t)$ , or its negative  $-f(t)$ , was sent, are called coherent; those in which phase information is lost are called incoherent. The POLCAT guidance system is an incoherent system.

On the basis of signal detection theory, there is an optimum manner in which the received signal should be processed (1). Upon reception, the signals and noise pass through a bank of parallel filters, one matched to each of the possible signals. For incoherent systems, the outputs of the matched filters are envelope detected; for coherent systems the detector is omitted and the phase is preserved. The value of the output, measured at the end of the transmission interval, contains all of the information relevant to identification of the signal transmitted. In the case of white, gaussian, additive noise, the probability of correct reception of each signal is a function of the ratio of the energy of the received signal to the spectral density of the noise. It is important to note, therefore, that this probability is independent of the shape of the signal, its duration, and its bandwidth (2).

To put the foregoing on a more secure theoretical basis, the relation of the signal-to-noise ratio to the error probabilities is derived and the advantages of repetitive pulses established. For continuity, this will be done first for the simplest binary system. Then, the criteria for deciding whether or not a signal has been received, and for establishing the threshold level and optimum receiver design will be developed for a

POLCAT type binary system.

#### 3.4.1.1 Probabilistic Criteria

Received signals are corrupted by additive fluctuation noise and therefore their wave shapes or amplitudes can only be estimated in the statistical sense. Statistical decision and estimation theory enables one to determine how to "best" perform the estimates.

The simplest problem is that of detecting the presence or absence of a signal pulse. In statistical terminology, given the value of a statistical sample, say voltage ( $v$ ), at a particular instant of time one must select one of two hypotheses,  $H_0$  or  $H_1$ . Hypothesis  $H_0$  may correspond to saying voltage ( $v$ ) represents noise and hypothesis  $H_1$ , the alternate hypothesis, then corresponds to saying a signal is present. Either choice could be in error.

If  $P(1,v)$  is the joint probability of occurrence of a signal and a received voltage of value  $v$  is the range  $v \pm dv/2$ , it can be expressed as,

$$P(1,v) = P_1 p_1(v)dv \quad (1)$$

It can also be expressed that,

$$P(1,v) = p(v)dv P(1/v) \quad (2)$$

Combining the two equations,

$$P(1/v) = P_1 p_1(v)/p(v) \quad (3)$$

Similarly,

$$P(0/v) = P_0 p_0(v)/p(v) \quad (4)$$

Given a specified sample value ( $v$ ), equations (3) and (4) are used to calculate the conditional probabilities  $P(1/v)$  and  $P(0/v)$ . For the case where  $H_0$  and  $H_1$  are of equal importance, the decision procedure simply involves choosing  $H_0$  if  $P(1/v) > P(0/v)$  or  $H_1$  if reversed. This insures a minimum number of errors over a large number of trials.

In the event that the two types of error have different significance, the above rule requires some modification. One possible procedure is to assign some loss values to the different types of errors and minimize average loss (3). The choice of hypothesis  $H_1$  corresponds to,

$$L_{10}P_1 p_1(v) > L_{01}P_0 p_0(v) \quad (5)$$

The effect of repeating a binary signal  $n$  times in an attempt to improve its detectability is considered, assuming that the a priori probabilities  $P_0$  and  $P_1$  are known.

The signal and additive noise at the receiver results in a random voltage ( $v$ ). If voltage is sampled  $n$  times, the problem, then, is how to "best" process the  $n$  samples,  $v_1, v_2, \dots, v_n$ , directed toward minimizing the overall probability of error in deciding between hypotheses  $H_0$  and  $H_1$ . As before, the conditional probabilities  $P(1/v_1, v_2, \dots, v_n)$  and  $P(0/v_1, v_2, \dots, v_n)$  are evaluated with the decision  $H_1$  or  $H_0$  based on the larger of the two.



An important case is where the successive samples of  $v$  are statistically independent, and in which instance the joint probability density functions become the product of their respective first order density functions. The test for choosing hypothesis  $H_1$  becomes,

$$\frac{p_1(v_1) p_1(v_2) \dots p_1(v_n)}{p_0(v_1) p_0(v_2) \dots p_0(v_n)} > \frac{P_0}{P_1} \quad (6)$$

(For this case the sampling interval  $1/B$  with  $B$  the system bandwidth in cps).

If the signal pulse is of amplitude  $A$  and the additive noise is gaussian with variance  $N$ , then, the  $j^{\text{th}}$  sample of voltage  $v$  will have, when the signal is present, the following probability distribution:

$$p_0(v_j) = \exp \left[ -(v_j - A)^2 / 2N \right] / (2\pi N)^{1/2} \quad (7)$$

If the signal is absent,

$$p_1(v_j) = \exp (-v_j^2 / 2N) / (2\pi N)^{1/2} \quad (8)$$

Using the ratio criterion of equation (6) to determine the condition for deciding on hypotheses  $H_1$ , and taking natural logarithms of both sides to simplify.

$$\sum_{j=1}^n v_j^2 - (v_j - A)^2 > 2N \log_e \frac{P_0}{P_1} \quad (9)$$

and equation (9) can be reduced to,

$$\sum_{j=1}^n v_j > \frac{nA}{2} + \frac{N \log_e \frac{P_0}{P_1}}{A} \quad (10)$$

This establishes that the optimum way of processing the  $n$  independent samples of signal plus gaussian noise in order to minimize the overall probability of error, is to add the samples and require them to either exceed or drop below a specified threshold level which is given by,

$$b = \frac{nA}{2} + \frac{N}{A} \log_e \frac{P_0}{P_1} \quad (11)$$

The threshold setting depends upon the signal amplitude ( $A$ ), noise variance, the probabilities of signal transmission ( $P_0, P_1$ ), and the number of samples integrated.

The probability of error is a function of the above parameters and in the case of  $P_0 = P_1 = 1/2$ , can be expressed as,

$$1/2 [1 - \text{erf}(\sqrt{n} A / 2\sqrt{2} N)] \quad (12)$$

where  $\text{erf } x = \frac{2}{\pi} \int_0^x \exp(-y^2) dy$

This indicates the improvement possible with repetitive signals for a simple binary system.

#### 3.4.1.2 POLCAT Detection Criteria

The previous discussion has been given to provide a basis and serve as a comparison for the analysis of the class of guidance systems into which the POLCAT semi-active homing system falls. It was implicitly assumed that the a priori probabilities,  $P_0$  and  $P_1$  were known. In the POLCAT concept there is no way of knowing in advance whether or not a signal reflected from a target will appear. Most of the time the voltages in the processing circuits will be due to noise. A procedure for minimizing

the overall probability of error cannot be used. The testing procedure developed by Neyman and Pearson (4), has been widely used; is particularly appropriate in this case. It is based on specifying one of the error probabilities. The two possible types of error that can be made are,  $\alpha$ : the probability that  $H_0$  will be rejected although true; and  $\beta$ : the probability that  $H_1$  will be rejected although true. In applying these definitions to POLCAT, the following notations are useful:

$P_n$  (equivalent to  $\alpha$ ) is the probability that noise is erroneously called signal.

$P_s$  (equivalent to  $1 - \beta$ ) is the probability of detecting a signal when it appears.

The optimum processing of  $n$  reflected pulses, spaced at large enough time intervals to ensure independent noise samples, corresponds essentially to that derived using Bayes' decision rule as outlined earlier in the section and given by equation (10). The only difference in this case is that, since the a priori probabilities are unknown, the critical region chosen will depend upon the choice of  $P_n$ , rather than  $P_0/P_1$ .

Thus, interpreting equation (10) in the Neyman-Pearson sense, the detection procedure consists of requiring the sum of  $n$  voltage pulses to exceed a specified threshold level. This level is determined by the allowable false alarm probability ( $P_n$ ). The recognition probability ( $P_s$ ), that signal plus noise will exceed the level (after summing or integrating) and be identified correctly as signal, is dependent upon the signal-to-noise ratio (SNR).

The application of this test procedure is independent of the actual signal amplitude or SNR. It is optimum in the sense that it defines

minimum SNR for a given  $P_N$  and  $P_s$ .

Figure 3.4-3 shows the relation between the false alarm rate ( $P_N$ ) and the SNR at the input to the envelope detector as a function of number of pulses added for a recognition probability of 98 percent.

The foregoing has not considered signal shape, system bandwidth and filter characteristics, etc. The ratio of the voltage sampled at the signal peak to the rms noise,  $A/\sqrt{N}$ , was determined and the probability of error established. Since both  $A$  and  $N$  depend upon the system transfer function, the transfer function is chosen to maximize  $A/\sqrt{N}$ .

If a signal  $f(t)$  is passed through a linear filter with impulse response  $h(t)$ , the filter represents the entire system between the point at which white noise is introduced and the point at which  $A/\sqrt{N}$  is measured. The output  $g(t)$  of the filter at some time  $t$  is given by the convolution integral.

$$g(t) = \int_{-\infty}^{+\infty} f(\tau) h(t - \tau) d\tau \quad (13)$$

The mean squared noise output at this same point, due to white noise of spectral density  $\eta$  at the filter point is,

$$N = \eta/2 \int_{-\infty}^{+\infty} h^2(\tau) d\tau \quad (14)$$

The filter impulse response appears in the equations for both  $g(t)$  and  $N$ . For convenience, consider the square of the ratio of  $g(t_0)/\sqrt{N}$ , with  $t_0$  defined as the time at which  $g(t)$  has its peak value  $A$ .

$$\frac{g^2(t_0)}{N} = \frac{S}{N} = \frac{\left[ \int_{-\infty}^{+\infty} f(\tau) h(t_0 - \tau) d\tau \right]^2}{\eta/2 \int_{-\infty}^{+\infty} h^2(\tau) d\tau} \quad (15)$$

In order to maximize this ratio, an artifice is used in which it is assumed that the signal energy ( $E$ ) is a known constant given by,

$$E = \int_{-\infty}^{+\infty} f^2(t) dt \quad (16)$$

Dividing equation (15) by a known constant will not affect the maximization process and leads to the following expression to be maximized:

$$\frac{\left[ \int_{-\infty}^{+\infty} f(\tau) h(t_0 - \tau) d\tau \right]^2}{\int_{-\infty}^{+\infty} f^2(t) dt \int_{-\infty}^{+\infty} h^2(\tau) d\tau} \quad (17)$$

by Schwarz's inequality

$$\left[ \int_{-\infty}^{+\infty} f(\tau) h(t_0 - \tau) d\tau \right]^2 \leq \int_{-\infty}^{+\infty} f^2(t) dt \int_{-\infty}^{+\infty} h^2(\tau) d\tau \quad (18)$$

with the equality holding if,

$$\begin{aligned} f(\tau) &= h(t_0 - \tau) \\ \text{i.e.} \quad h(t) &= f(t_0 - \tau) \end{aligned} \quad (19)$$

This condition, called a matched filter, provided the maximum value of peak SNR. This maximum SNR is given by substituting equation (19) into equation (15).

$$(\text{SNR})_{\max} = \frac{\int_{-\infty}^{+\infty} f^2(t) dt}{\eta/2} \frac{2E}{\eta} \quad (20)$$

The maximum values of the peak SNR, then depends only on the signal energy and the white noise spectral density.

The binary signal decision problem in the case of "colored" noise (noise of arbitrary spectral density) can be treated similarly by first equalizing or pre-filtering to convert the noise to band limited white

noise, and then proceeding with the matched filter decision procedure (5).

Equation (20) indicates the important design considerations for the POLCAT guidance system. Assuming the optimum receiver (matched filter) and best decision procedure (Neyman-Pearson in this case) the signal-to-noise ratio will be maximum if the energy of the signal is maximized in the region where the noise spectral density is minimum. When the peak power of the illuminator is limited, the energy may be increased by making the signal duration as long as possible..

As the signal length is increased the ability to resolve the spatial position of the target decreases, therefore, the maximum signal duration is a function of the error probabilities. If the noise is white, a single pulse of energy (E) would produce the same SNR as a series of pulses with the same total energy.

In the following discussion of the various sources of guidance system noise, it is shown that the spectral density of the noise, which limits POLCAT, is not white and that it is desirable to shape the signal so that its power is located in the most advantageous region of the spectrum.

### 3.4.2 Noise Analysis

The term noise defines those random electrical fluctuations that are added to the signal between the transmitter and the point in the communication link where the decision as to whether a signal is present or not is made. The previous section showed that the probability of the POLCAT receiver detecting a signal in noise was inversely proportional to the noise spectral density. The additive noise are those fluctuations which are present even when there is no signal. The noise may be due to effects in the channel or receiver or due to interactions between them. This excludes those random characteristics of the encoder and transmission medium which only modulate the signal, since they are multiplicative noises and must be treated by different analytical techniques.

The limitations on POLCAT guidance performance due to additive noise are determined by examining photon noise, semiconductor noise, atmospheric scintillation, and scanning noise.

#### 3.4.2.1 Photon Noise

The photon noise effect is due to the random arrival at the detector of the discrete energy carriers, photons. According to the best accepted theory, the mechanism of photoconductivity in lead sulfide detectors is due to the increase in charge carriers liberated by the incident photons. Therefore, assuming that the rate of arrival of photons is a random process, the variations in detector current are determined by the statistics which describe the rate of absorption of photons by the detector. The photon process may be due to thermally emitted photons from the background and detector surrounds (which are described by Bose-Einstein statistics) or they may be

due to photons reflected from the background or they may be due to photon fluctuation in the signal itself.

The dominant noise phenomenon affecting POLCAT guidance performance is due to the reflected sunlight from the background. The average number of photons which arrive at the detector from the element of background which is viewed during the measurement interval is,

$$\int_{\lambda}^{\lambda+\Delta\lambda} \left( \frac{\bar{N}_{B\lambda} t_{\lambda} \theta_v \theta_h M}{2 \Delta f} \right) d\lambda \quad \text{photons} \quad (1)$$

The average number of photons which arrive at the detector during the measurement time when there is a target in the field is:

$$\int_{\lambda}^{\lambda+\Delta\lambda} \frac{\bar{N}_{B\lambda} t_{\lambda} \theta_v \theta_h M + \bar{N}_{T\lambda} M}{2 \Delta f} d\lambda \quad (2)$$

Since the random process can be described by a Poisson distribution the variance is equal to the average. The number of free carriers due to the target photons can be detected against the carriers liberated by the background photons within the specified error probabilities, when

$$\int_{\lambda}^{\lambda+\Delta\lambda} \left( \frac{\bar{N}_{T\lambda} t_{\lambda} \theta_v \theta_h M}{2 \Delta f} \right) d\lambda \geq \text{SNR} \left[ \int_{\lambda}^{\lambda+\Delta\lambda} \left( \frac{\bar{N}_{B\lambda} t_{\lambda} \theta_v \theta_h M}{2 \Delta f} \right) d\lambda \right]^{1/2} \quad (3)$$

When the distribution of  $\bar{N}_{B\lambda}$ ,  $\bar{N}_{T\lambda}$ ,  $t_{\lambda}$ ,  $\theta_v$ ,  $\theta_h$  are uniform over  $\Delta\lambda$

$$\frac{\bar{N}_{T\lambda} t_{\lambda} \theta_v \theta_h M \Delta\lambda}{2 \Delta f} \geq \left[ \text{SNR} \frac{\bar{N}_{B\lambda} t_{\lambda} \theta_v \theta_h M \Delta\lambda}{2 \Delta f} \right]^{1/2} \quad (4)$$



Since the photon energy is  $h\nu$ , the above can be expressed in terms of the signal spectral incidence at the receiver ( $H_{T\lambda}$ ) and the background spectral sterance ( $W_{B\lambda}$ ) as follows (20),

$$\frac{H_{T\lambda} / (\lambda M \Delta\lambda)}{2 \Delta f h \nu} \geq \text{SNR} \left[ \frac{W_{B\lambda} t_{\lambda} \mu_{\lambda} \theta_v \theta_h M \Delta\lambda}{2 \Delta f h \nu} \right]^{1/2} \quad (5)$$

which establishes the requirements for signal spectral incidence in terms of background spectral sterance for a photon noise limited system.

$$H_{T\lambda} = \text{SNR} \left[ \frac{2 W_{B\lambda} t_{\lambda} h c \theta_v \theta_h \Delta f}{\lambda \Delta\lambda \mu_{\lambda} M} \right]^{1/2} \frac{\text{watt}}{\text{cm}^2 \text{-micron}} \quad (6)$$

where  $\lambda$  defines the spectral wavelength in centimeters. The photon noise equivalent power (SNR = 1) is obtained from equation 5 in terms of background sterance and expressed as,

$$\text{NEP}_{\text{photon}} = \left[ \frac{2 W_{B\lambda} t_{\lambda} h c \Delta f \theta_v \theta_h M \Delta\lambda}{\lambda \mu_{\lambda}} \right]^{1/2} \text{ watts} \quad (7)$$

#### 3.4.2.2 Semiconductor Noise

The characteristics of the semiconductor noise depend upon the physical properties of the material used and the particular operating conditions. The various types of noise may be categorized as thermal noise, generation-recombination noise (similar to shot noise) and current noise. Figure 3.4-4 shows the relative frequency regions in which each of these occur.

Thermal noise is present in all conductors and semiconductors and is caused by the random motions of the charge carriers. This noise dominates

at high frequencies. The mean square thermal noise current is given by:

$$\overline{i_N^2}_{\text{thermal}} = \frac{4 k T \Delta f}{R} \quad \text{amp}^2 \quad (8)$$

This noise spectrum is independent of frequency up to about  $10^{13}$  cps where quantum-mechanical effects occur.

In semiconductor materials, the statistical fluctuations in the concentration of charge carriers gives rise to generation-recombination noise. It is analogous to shot noise in electron tubes and is associated with photon noise in photon detectors. This is the major source of detector noise at intermediate frequencies.

The power spectrum of the g-r noise (8) is given by:

$$P(f) = \begin{cases} \frac{4 I_0^2}{N(1 + \omega^2 \tau^2)} & \frac{\text{watt}}{\text{cps}} & \text{for extrinsic} \\ & & \text{semiconductors} \\ \frac{2 I_0^2}{N(1 + \omega^2 \tau^2)} & \frac{\text{watt}}{\text{cps}} & \text{for intrinsic} \\ & & \text{semiconductors} \end{cases} \quad (9)$$

which is essentially flat up to frequencies which correspond to the mean carrier lifetime.

The mean square g-r noise current can be generally expressed as:

$$\overline{i_N^2}_{\text{g-r}} = \frac{K_1 I_0^2 \Delta f}{1 + (f/f_1)^2} \quad \text{amp}^2 \quad (10)$$

where the constants  $K_1$  and  $f_1$  are related to the number of charge carriers and their lifetimes, and are chosen to fit experimental data for a particular

material.

The third type of noise which arises in semiconductor detectors is current noise. It is also called  $1/f$  or modulation noise. Current noise source are associated with potential barriers existing at intergranular contacts, at rectifying electrodes, at the semiconductor surface, at dislocations, at point contacts or at p-n junctions. It has been suggested that this noise is due to some effect which modulated the carrier densities and thus the conductivity of the material.

The power spectrum of current noise may be expressed as (8),

$$\overline{i_{N\text{current}}^2} = \frac{K_2 I^\alpha \Delta f}{f^\beta} \quad (11)$$

where  $\alpha \approx 2$ ,  $\beta \approx 1$  and  $K_2$  is a constant related to the resistivity, dimensions and other material constants.

#### 3.4.2.3 Atmospheric Scintillation

When a point source is viewed through the atmosphere, the image varies with time both in position and intensity. This is called atmospheric scintillation noise. The turbulence in the transmission medium due to wind and temperature gradients causes temporal variation of the propagation parameters. Measurements of this effect (10) indicate that:

- (a) Fluctuations of light intensity caused by atmospheric turbulence have a log normal distribution.
- (b) Dependence of  $\sigma^2 = \overline{[\log(I/I_0)]^2}$  on path length ( $L$ ) agrees with the theory of the phenomenon, which leads to the formula  $\sigma \approx L^{11/6}$ .
- (c) Confirmation of the theoretical conclusion that the correlation

- (c) function of the fluctuations of the light intensity depends on  $c/(\lambda L)^{1/2}$  and that the correlation distance is of order  $(\lambda L)^{1/2}$ .
- (d) The frequency spectrum of light intensity depends on  $f(\lambda L)^{1/2}/V_n$  and good agreement is observed between the intervals of time correlation and space correlation.

The frequency at which maximum fluctuations occur is given by,

$$f_m = 0.32 V_n / (\lambda L)^{1/2} \quad \text{cps} \quad (12)$$

Figure 3.4-5 shows the frequency spectrum of light intensity variation for different wind velocities.

It was also found that the amplitude of the fluctuations depends significantly on the dimensions of the collecting aperture. Figure 3.4-6 shows an empirical relation between the amount of twinkling and the receiver diameter.

#### 3.4.2.4 Scanning Noise

Guidance systems which employ optical search techniques require relative motion between the line of sight and the target background. Any spatial variations in the background sterance pattern will give rise to a time variation in the received radiation. This fluctuation which is due to the interaction of the background pattern, the optical field of view and the scan function is the scanning noise. Since the optical and scan parameters are known for any particular system the randomness arises from the background description. Those backgrounds of interest in the POLCAT guidance concept are non-stationary, two dimensional distributions. Varia-

tions in the pattern and changes in the intensity and direction of the sunlight illumination make the background a non-stationary random process. It might be developed when scanning a terrain with high contrast objects on bright clear days. It is also to be expected that different classes of scenes (fields, deserts, built up areas) might have different statistical descriptions.

Analytical methods for treating the stationary version of the problem have been suggested by Genoud (12) and Biberman (13), based on the more general studies by Elias (14) and Jones (15). Applying these methods, which assume the autocorrelation function of the background radiance to be constant, the noise power per unit area from the background had been computed (20) for a POLCAT seeker incorporating a rectangular scanning aperture and ideal electrical filters. The limitation of this analysis was the lack of knowledge relative to the background autocorrelation function for the type of terrain applicable to POLCAT.

Accordingly, a program was conducted which determined, directly, Fourier spectra for noise developed by scanning terrain representative of the ground combat environment. Figure 3.4-7 shows some of the scenes where measurements were made. All the data obtained during the measurement program are presented in the Design Data Supplement. For the purposes of this report, these data were reduced to the spatial frequency spectrum given in figure 3.4-8. This single dimensional description was obtained by assuming the background to be isotropic. It is an average representation; the standard deviation for the limited number of scenes which were scanned is three to five times the average.

To use the figure 3.4-8, it is necessary to determine the spatial frequency region in which the system operates. The spatial center frequency (cycles/rad) is determined by the ratio of signal frequency (cps) to line of sight rate (rad/sec). The bandwidth (cycles/rad) is determined by multiplying the spatial center frequency (cycles/rad) by the ratio of the electrical bandwidth (cps) to the electrical frequency (cps).

### 3.4.2.5 Noise Evaluation

The basic noise mechanisms of the POLCAT guidance system have been discussed from a general standpoint in the foregoing paragraphs. It is necessary to examine each in the light of the system parameters and tactical environment. A convenient method for determining the limiting noise effect is to compare the noise equivalent powers due to each mechanism. This will require using certain design values which will be discussed and derived in subsequent sections.

Using equation 7, the photon NEP is estimated for the following conditions:

$$W_{B\lambda} = 5000 \text{ microwatts/cm}^2\text{-steradian-micron (reference 8)}$$

$$t_{\lambda} = 1.0 \quad \tau'_{\lambda} = 1.0$$

$$M = 100 \text{ cm}^2 \quad \Delta\lambda = 0.4 \text{ microns}$$

$$\Delta f = 1000 \text{ cps} \quad \lambda = 10^{-4} \text{ cm}$$

$$\Theta_V = \Theta_H = \Theta = 0.025 \text{ radians}$$

$$\underline{\text{NEP}_{\text{photon}} = 2.2 \times 10^{-10} \text{ watts}}$$

In photoemissive, photovoltaic or PEM detectors, background fluctuations contribute to the photon noise. However photoconductors depend upon

the change in concentration of charge carriers upon irradiation. The concentration of free carriers is determined by both the generation and recombination rates. With radiation falling on the detector the carriers are undergoing continuous photoexcitation and recombination. It has been shown (16) that at equilibrium in a photoconductor the total noise power (photon and g-r) can be no less than twice the photon noise power alone. This gives:

$$\underline{NEP_{\text{photons and g-r}} = 4.4 \times 10^{-10} \text{ watts}}$$

A lead sulfide photoconductor was used in the POLCAT receiver. Ordinarily this type of semiconductor is current noise limited (8), where the noise follows a power law that exhibits essentially a simple inverse frequency dependence. From equation 11 it is seen that the current noise is a strong function of the bias current. If the detector is biased from a constant supply (high impedance) the noise current will remain constant under all levels of illumination. However to minimize aging and other effects it is often convenient to use a source impedance which is less than that of the detector. This approaches a constant voltage supply. Under maximum illumination within its linear range ( $10^5$  to 1) the resistance of the POLCAT PbS detector will decrease by less than a factor of two (9). Therefore, the maximum current noise which can be expected, due to high ambient illumination is no more than about twice the noise due to the dark current. The NEP due to semiconductor noise is given by  $(\Delta f)^{1/2} (A_d)^{1/2} / D^*$  in watts.

For,

$$D^*(1\mu, 2000, 1) = 3 \times 10^{10} \text{ cm-cps}^{1/2} / \text{watt (reference 7)}$$

$$\Delta f = 1000 \text{ cps}$$

$$A_d = 0.026 \text{ cm}^2$$

$$\underline{\text{NEP}_{\text{current}} = 2 \times 10^{-10} \text{ watts}}$$

To estimate the scanning noise, it is necessary to determine the line of sight writing rate, which for an annular scan is given by  $(\pi f_s / 90) \tan^{-1} \pi \theta_c$  in radians/second.

For,

$$\theta_c = 0.070 \text{ radians}$$

$$f_s = 20 \text{ cycles/second}$$

$$\text{signal frequency} = 2000 \text{ cps}$$

$$\text{signal bandwidth} = 1000 \text{ cps}$$

The line of sight rate is 8.7 rad/second. This gives the center frequency in terms of spatial dimensions as 230 cycles/radian and the spatial bandwidth as about 100 cycles/radian. From figure 3.4-8 the scanning noise equivalent incidence is  $5 \times 10^{-10} \text{ watts/cm}^2\text{-micron}$ . For a collecting aperture of  $100 \text{ cm}^2$  and a spectral bandwidth of 0.4 microns,

$$\underline{\text{NEP}_{\text{scanning}} = 2 \times 10^{-9} \text{ watts}}$$

### 3.4.3 Signal Analysis

The received signal incidence,  $H_{T\lambda}$ , is a function of the transmitted signal power and the various attenuations it has undergone. This is given

$$\text{by: } H_{s\lambda} = \frac{P_{B\lambda} t_{\lambda} r_{\lambda}}{\pi R_{T-R}^2} \quad \text{watt/cm}^2\text{-micron} \quad (1)$$



This expression is random to the extent of the uncertainty for each of the multiplicative factors.

In this section each of the factors will be considered in the light of the POLCAT concept requirements. The characteristics of an illuminator designed for field operation with the POLCAT system and actually used for related studies will also be described.

#### 3.4.3.1 Illuminator

The signal source was designed so as to provide the maximum energy in the region of minimum noise spectral power density. Since the power spectrum of the noise which limits the guidance system decreases with frequency and spectral width, the light beam which illuminates the target should have the highest possible power concentrated in the narrowest possible wavelength band, modulated at the highest possible frequency, and the receiver should be designed so it can examine the reflected power for the longest possible time.

The peak spectral power into the beam is approximated by:

$$(\pi/4)^2 \delta^2 D^2 \lambda W_{s\lambda} \quad \text{watt/micron} \quad (2)$$

It is desirable to maximize all of the factors in equation 2.

In the POLCAT application, the illuminator beam must subtend no more than about two meters at 2000 meters which gives a maximum beamwidth of 0.001 radians. For a maximum diameter of the optics of 30 cm and an optical efficiency approaching unity, the spectral flux into the beam is approximately,

$$5 \times 10^{-4} W_{s\lambda} \quad \text{watts/micron} \quad (3)$$

The source most compatible with the POLCAT concept and available within the state of the art at the time of illuminator design was the arc discharge lamp. The spontaneous emission from this source occurs in spectral lines which broaden as temperature and pressure are increased. Since the excitation is electronic instead of thermal, the brightness of an emission band at modest input powers can be equivalent to a relatively high temperature black body. Most discharge lamps emit in the visible and ultraviolet spectrum. The xenon lamp provides output in the near infrared. Figure 3.4-9 shows the spectral sterance of the commercial xenon arc lamp used in the POLCAT system. In the 0.88 to 1 micron region the sterance is about 400 watts/cm<sup>2</sup>-steradian-micron.

The radiation from discharge tubes may be modulated by varying the input electrical power.

An illuminator was designed and fabricated in accordance with the POLCAT guidance system and environmental requirements. Figure 3.4-10 shows two photographs of the equipment.

### Illuminator Specification

Source - Hanovia Xenon Lamp type 844-C-1  
arc length: 0.3 mm  
spectrum: 0.8 - 1.1 microns

Optics - Parabolic reflector  
aperture: 12 inches  
focal length: 12 inches

Beam width - 3 milliradians (limited by optical aberrations)

Modulation - 2000 cps, mechanically chopped

Power supply - demand 28vdc at 5 amps  
rechargeable battery capacity: 300 amp hr

The illuminator was designed to accommodate either a xenon or mercury arc discharge lamp. Since mercury lamps cannot be effectively modulated electrically, mechanical modulation was used. The modulation frequency was limited to 2000 cps by mechanical considerations in the illuminator and by the time constant of available detectors.

#### 3.4.3.2 Atmospheric Transmissivity

Atmospheric transmissivity is predictable to the extent that weather and battlefield conditions are predictable. Since transmissivity is a multiplicative factor on the signal, its variance has an appreciable effect on POLCAT receiver performance.

Atmospheric attenuation in the infrared is due to three independent phenomena: molecular absorption, principally from water vapor; aerosol scattering, by mist and fog; and particle absorption, by dust and haze.

The water vapor volume varies between 0.001 and 1 percent depending upon geographical and meteorological conditions. Figure 3.4-11 shows the precipitable water vapor per foot of path length as a function of tempera-

ture and relative humidity (17).

The particle and aerosol concentration is given below:

<u>Atmospheric Contaminants</u>		
<u>Atmospheric Condition</u>	<u>Particle Size</u>	<u>Particle Concentration</u>
clear, dry (18)	0.1-1 micron: 95 percent 1-10 microns: 5 percent	100 particles/cm <sup>3</sup>
industrial haze (18)	0.03-2 microns	100,000 particles/cm <sup>3</sup>
fog (19)	3-60 microns (peaks at 7)	50-500 particles/cm <sup>3</sup>
clouds (19)	2-30 microns	1-50 particles/cm <sup>3</sup>

The attenuation at any particular wavelength thus depends on physical factors which may be difficult to specify. Empirically derived factors or models are used, in general, to determine the transmissivity. Models are useful, not only from the standpoint of simplicity, but also since they relate the transmission in the infrared to that in the visual regions. There is some variability among methods of determining the atmospheric transmissivity. The model given here is after Kruse et al (8).

The model requires computation of two attenuation factors,  $\tau_{a1}$  due to absorption in various regions of the infrared, and  $\tau_{s1}$  due to scattering. The expressions are,

$$\tau_{a1} = \begin{cases} \exp(-A_1 w^{1/2}) & \text{for } w < w_1 \\ k_1(w_1/w)^{B1} & \text{for } w > w_1 \end{cases} \quad (4)$$

where  $w$  is the precipitable water in mm.

The constants  $A_1$ ,  $k_1$ ,  $B_1$ , and  $w_1$  are evaluated as follows:

Spectral region (microns)	$A_1$	$k_1$	$B_1$	$w_1$
0.72-0.94	0.0305	0.800	0.112	54
0.94-1.13	0.0363	0.765	0.134	54

$$\text{and } \tau_{s1} = \exp \left[ - \frac{3.91}{V} \left( \frac{\lambda_1}{.55} \right)^{-q} x \right] \quad (5)$$

where  $V$  is the visual range in kilometers (distance at which contrast is reduced to 2 percent), and where  $q = 0.59 V^{1/3}$  for  $V \leq 6$  km;  $q = 1.3$  for "average" conditions of visibility; and  $q = 1.6$  for "excellent" conditions of visibility.

The overall atmospheric transmission coefficient is the product of the absorption and scattering coefficient. Figure 3.4-12 presents the results of atmospheric transmission measurements in the near infrared spectrum.

### 3.4.3.3 Target Reflectivity

The beam of radiation from the POLCAT illuminator is both attenuated and scattered by the target. This is a result of the surface conditions such as color and texture as well as the geometrical shape. The target cannot be described as a simple reflecting surface with a diffuse or specular coefficient but rather the pattern of the reflected power as a function of angle of incidence must be given, in order to attain this definition (11).

Measurements were made of the field pattern of reflected power from

an M48 A-1 tank when illuminated by the POLCAT illuminator (21). It was determined that the reflected power could be generally described by a specular component and a diffuse component. Table 3.4-2 lists some of the results of the measurements.

The contour pattern of figure 3.4-13 represents a model for the field pattern of the reflected power from a fully illuminated tank target.

#### 3.4.3.4 Target Signal

The spectral power density at the receiver of the radiation reflected from the tank (signal incidence) is given in terms of the source and the attenuation factors sterance by combining equations (1) and (3).

$$H_{s\lambda} = \frac{1.6 \times 10^{-4} W_{s\lambda} t_{\lambda} r_{\lambda}}{R_{T-R}^2} \quad \text{watt/cm}^2\text{-micron}$$

Figure 3.4-14 shows the total power incident on the detector for the specified optical parameters as a function of target-receiver distance. This peak signal power can be compared with the limiting system noise (Section 3.4.2) and the resulting SNR related to the guidance system error probabilities given by figure 3.4-3.

Table 3.4-2 Reflection Coefficients of M48 A-1 Tank  
Beam diameter at target: 6 feet

Tank Aspect to Incident Beam	Receiver Spectral Range (microns)	Angle from Horizontal (degrees)	Tank Surface Condition	Total		Diffuse Reflection Coef. ( $r_d$ )	Specular Reflection Coef. ( $r_s$ )
				Power Refl. Total	Power Incid.		
beam	0.28-2.7	0	clean, dry	0.135		0.037	0.0024
beam	0.28-2.7	0	clean, dry	0.11		0.037	0.0015
front	0.28-2.7	0	clean, dry	0.09		0.05	0.0003
rear	0.28-2.7	0	clean, dry	0.065		0.043	0.0002
45°	0.28-2.7	0	clean, dry	0.095		0.048	0.0003
45°	0.28-2.7	0	wet	0.155		0.025	0.0037
beam	0.7-1.1	0	clean, dry	0.13		not determined	
45°	0.28-2.7	10	clean, dry	0.09		not determined	
45°	0.28-2.7	45	clean, dry	0.09		not determined	

received power density due

to diffuse reflection

$$r_d = \frac{\text{received power density due to diffuse reflection}}{\text{total power incident on target}}$$

$$\propto (\text{target-receiver distance})^2$$

received power density due

to specular reflection

$$r_s = \frac{\text{received power density due to specular reflection}}{\text{total power incident on target}}$$

$$\propto \frac{1}{r^2} (\delta) (\text{distance from illuminator to target}) R_{T-R}$$

where: 1. target fills beam 2. receiver is within specular reflection

#### 3.4.4 Seeker Design

As established by the POLCAT concept, the seeker must perform two basic functions: 1) determine when the illuminated target enters its instantaneous field of view, and 2) provide a control signal to the pulser if this occurs. The preceding analyses established the requirements for performance where the seeker is considered a receiver in a communication system. Thus seeker design must provide a) a spectral "match" and an electrical "match" for the target signal, and b) provide a Neyman-Pearson type decision process for non-coherent signals. The POLCAT seeker design, shown in figure 3.4-15, is discussed from this point of view.

Descriptions are given of the optics, detector, electronic processing system (amplifier and trigger circuit), power supply, and the functional tests that were performed with these components.

##### 3.4.4.1 Optics and Detector

The design of the optical system was determined by the requirements on angular resolution, spectral interval, optical "speed" and, particularly, the requirement of withstanding 10,000 g acceleration at launch. The latter requirement had a significant effect on the optical configuration that was selected. Prior air gun tests indicated that all-refractive optics, which are usually edge supported, failed during test. All-reflecting optics, which expose the detectors and optical filters, lead to a difficult mounting problem. The refractive-reflective optical design, shown in figure 3.4-16, was conceived as the most practical. The arrangement permits both the optics and detector to be supported in such a way as to distribute the launching shock uniformly against a large flat



surface. The design also provides a double "fold" of the optical path which results in a compact design. The refracting front surface acts as a dome, offering protection for the detector and optical filters. The results of air gun tests on the lens described in Section 3.2.2.1 indicated that this optical design can withstand launch accelerations of 10,000 g.

The required optical resolution is related to instantaneous field of view. This field may be found from the required signal characteristics which were discussed in Section 3.4.3 and in turn, shown to be based on the allowable error probabilities, viz., false alarm probability, recognition probability and hit probability.

The tangential dimension of the elemental field is given by:

$$\tan^{-1} \left\{ 2(\tan \alpha) \left( \tan \frac{80 n f_s}{f} + \Delta \phi_c \right) \right\}$$

The radial dimension of the instantaneous field is  $2\alpha$  degrees where  $\alpha$  is the pitch angle in degrees. For the expected projectile flight characteristics, the dimensions of the instantaneous field were established as follows:

tangential angle = 1 and 1/2 - 2 degrees

radial angle = 1 degree

For maximum sensitivity the total energy in each signal pulse should fall on the detector. This requires that the resolution of the optics be better than

$$\frac{\text{tangential angle}}{n + (f \Delta \phi_c / 180 f_s)} \quad \text{degrees}$$

that is, better than about  $1/4$  degree.

The focal length of the lens was designed to be as short as possible, compatible with the above criteria. This not only permits a compact design but also minimizes the area of the sensitive detector. As mentioned in Section 3.4.2, this also minimizes the noise potentials developed in the cell.

The spectral wavelength region of the signal was discussed in Section 3.4.3. The optics were fabricated from a glass which would provide the characteristics derived above with radiation from 0.8 to 1.2 microns. Chromatic aberration was found to limit the resolution of the lens.

The lens specifications are as follows:

Material:	Borosilicate Crown (Schott type BK-7)
Focal Length:	180 mm
Aperture Ratio:	$f/1.5$
Resolution:	0.15 degree (on axis)
Flange Focal Length:	30 mm
Spectral Range:	0.8 - 1.2 microns

The manufacturing specification for the lens is given in the Design Data Supplement.

The detector was selected so that its electrical characteristics matched the signal and its physical characteristics were compatible with the required field of view and the environment. The detector specifications are as follows:

Material:	Lead Sulfide - chemically deposited (low sodium glass substrate) Infra- red Industries type BLSA7
Detectivity: D* (500, 1500, 1)	$3 \times 10^8$ cm (cps) <sup>1/2</sup> /watt
Time Constant:	less than 60 microseconds
Dark Resistance:	less than a megohm
Active Area:	0.160 x 0.160 inches
Wave Length of Peak Sensitivity:	2.85 micron

Figure 3.4-17 shows the optic-detector arrangement. To achieve the required resolution it is necessary that the center of the field of view be along the optical axis. Therefore the lens and detector combination were offset from the roll axis by the line of sight angle.

In order to support the detector and its lead wires during launch and flight, and to prevent extraneous radiation falling on the detector, epoxy potting material was added to the detector cavity. The surface of the conical cavity was grooved to eliminate internal reflections and coated with an optically black paint.

#### 3.4.4.2 Electronic Processing System

The POLCAT electronic processing system first linearly amplifies the detector signal with a "matched filter". It then provides a logic circuit which decides if a signal is present in noise. In the event of a signal a pulse of electrical energy is delivered to the control cartridge. A block diagram of the seeker electronic system is shown in figure 3.4-18.

In Section 3.4.3 the signal was shown to be a train of sinusoidally

modulated radiation. For a train  $t_0$  seconds long and a modulation of amplitude  $A$  and frequency  $\omega_0$ , the signal is described by

$$f(t) = A \sin \omega_0 t \quad -t_0/2 \leq t \leq t_0/2$$

The energy spectrum is

$$K \left[ \frac{\sin 4\pi(\omega/\omega_0 - 1)}{4\pi(\omega/\omega_0 - 1)} + \frac{\sin 4\pi(\omega/\omega_0 + 1)}{4\pi(\omega/\omega_0 + 1)} \right]^2$$

Figure 3.4-19 shows the energy spectrum for a 4 cycle train modulated at 2000 cps.

It was shown in Section 3.4.3 that the filter impulse response should be  $h(t) = f(t_0 - t)$ . In actual practice the exact shape of the matched filter is usually of secondary importance, the proper system bandwidth being the crucial quantity (6). The output SNR for a single RC network (the low frequency equivalent of a single tuned circuit), a gaussian filter (this corresponds to a large number of synchronously-tuned amplifier stages) and an ideal rectangular filter show little difference if the bandwidth is chosen properly. All of the filters provide a peak SNR within one db of that obtainable in the matched filter case. The optimum bandwidths are shown in figure 3.4-20. For the case of multistage filters the overall response approaches the gaussian filter. The peak SNR occurs in this case for  $f_c t_0 = 0.4$ . The maximum is quite broad, however, varying by no more than one db from  $f_c t_0 = 0.2$  to  $f_c t_0 = 0.7$ .

As shown in Section 3.4.2, the limiting noise is due to electrical

signals generated by scanning the variegated terrain background. This noise power incidence was shown to be about  $5 \times 10^{-10}$  watts/cm<sup>2</sup> - micron. For an effective collecting aperture of 80 sq cm and a spectral bandwidth of 0.5 micron, the average scanning noise equivalent power is about  $2 \times 10^{-8}$  watts. This is an average noise voltage out of the detector of about 40  $\mu$ volts.

At this point, detailed descriptions of the amplifier and, then, the trigger circuit are given.

#### 3.4.4.3 Amplifier

The amplifier consists of four stages of common-emitter transistor circuits. Sufficient dc degeneration is utilized in each individual stage for dc bias stabilization, while ac degeneration is also incorporated to minimize variation of gain of each stage. The loads on the first two stages consist of tuned circuits to obtain the required band-pass characteristics. A zener diode voltage regulator drops the battery voltage down to 22 volts dc as required by the amplifier circuitry. An R-C decoupling network minimizes the effect of the battery or zener diode source resistance on the frequency stability of the amplifier. The transistors utilized are of the 2N43A type. These transistors have low noise and medium gain characteristics. Their reliability in extreme environments had been proven by past performance and rigorous testing.

The specifications for the POLCAT amplifier are given below.

Midband voltage gain	81 db (minimum)
Midband frequency	2000 cps
Bandwidth (3 db pts)	1500 cps - 2500 cps
Input impedance	33K $\pm$ 20 percent
Output impedance	1K + 0 percent -20 percent

Specifications for the POLCAT amplifier (cont'd):

Equivalent noise input voltage	$2.4 \times 10^6$ volts
Linear operating range	0 - 5 volts pk to pk
Operating temperature	-40 C to +100 C
Pulse response	Ringings must be less than 2 cycles to a step input
Power supply voltage	-40 volts +20 to -50 percent
Power supply impedance	1K ohm max

A schematic of the amplifier is shown in figure 3.4-21

... The overall performance of the amplifier can be summarized as conforming to the specifications tabulated in this report. The gain of the unit is adjusted to the required level by adjusting R 109 (shown in the schematic) to the proper value. The adjustment is necessary due to the large gain tolerance (3:1) of the transistors. The circuit will operate with no appreciable decrease in gain as the battery supply voltage is decreased to 20 volts. Applying an impulse of up to 1 volt magnitude to the input of the amplifier will result in a 2000 cps output signal of two-cycle duration. This is due to the ringing characteristics of the tuned circuits in the amplifier. This characteristic, however undesirable, is unavoidable if bandwidth requirements are to be met. However, since an output signal of at least four-cycle duration is necessary for successful triggering, a ringing of two-cycle duration does not significantly affect system performance.

Amplifier components were mounted inside a grooved annulus made of linen-base bakelite. Electrical connections were made by a long feed through posts that interconnect individual components of the system both electrically and mechanically. The circuitry was encapsulated by a mixture

of Hysol 6020 and Thyokol LP-3, plus Hysol Hardener C, in proper proportions. This mixture cures into a transparent hard solid.

#### 3.4.4.4 Trigger Circuit

The trigger circuit serves two purposes. It decides if the signal is present and then it provides an output signal to initiate the squib firing process. The specifications for the trigger circuit are as follows:

Input impedance	10 kilohms
Output impedance	2 ohms
Integrating time constant	1 millisecond
Energy into load	0.05 joules

In Section 3.4.1, it was shown that the optimum decision procedure for the incoherent on-off signal train included a rectifier to envelope detect the signal out of the matched filter and a summing circuit to add successive pulses. If the summed signal exceeds a threshold, established by the noise, then the decision is made that there is a signal present in the noise.

This procedure was implemented in the following manner. Referring to the schematic in figure 3.4-22, the 2N43A transistor is normally fully conducting and 2N1132 is normally cut off. It is important that the cut-off current of this stage be very low ( 10 microamps) or else the circuit will oscillate at a low frequency.\* When properly cutoff, the 0.28 f capacitor will charge to 18 volts. This voltage at the emitter of the

\* One of the five seeker units oscillated at a low frequency (motorboated) when received by Frankford Arsenal. Another seeker developed a similar trouble after air gunning. This was found to be caused by the high cutoff current of the 2N43A transistor which originally preceded the unijunction device. The amplifier design was modified to specify a 2N1132 transistor for this critical circuit. This design was successfully tested in on of the prototype POLCAT seekers.

2N490 unijunction transistor will not discharge that device, consequently the silicon controlled rectifier is cut-off. If an input signal greater than 1 volt peak to peak is applied, the positive halves of the signal turn the 2N43A off and the 2N1132 on. This brings the charging voltage at the collector to +36 volts. During each positive half of the input signal the 0.28 f capacitor and the 2 kilohm resistor receive a charging pulse of +22 volts which charges the capacitor towards 36 volts. The time constant of the charge circuit is adjusted so that the charge on the capacitor reaches 24 volts during the fourth cycle of a 2000 cycle per second signal. As the voltage on the 0.28 f capacitor reaches 24 volts the 2N490 fires. This, then, is the decision that a signal is present.

The 1 volt peak to peak threshold was set from the average background noise level multiplied by the gain of the linear amplifier section. The Neyman-Pearson decision criterion established the required threshold. If the noise is non-stationary, there are three possibilities for implementation -- a compromise threshold established, provision made for adjustment prior to firing, or inclusion of an automatically adjustable circuit.

When a signal is present, the trigger circuit must provide a suitable pulse of energy to an electronic detonating device (explosive squib). The trigger circuit design was based on operation with the T20E1 detonator which has a specified dc resistance of 2 to 10 ohms. Experience has shown that the nominal dc resistance for the T20E1 detonator is 2.5 ohms. Since the limits of 2 to 10 ohms are specified, the performance is summarized below for three values.



### Detonator dc Resistance Limits

	<u>10 Ohms</u>	<u>2 Ohms</u>		
Maximum firing Voltage	None	None		
Minimum firing voltage	50	50		
Delivered energy (ergs)	5000	5000		
Time energy delivered (microsecs)	6	3		
Digestion time for detonator (microsecs)	5-10	5-10		
Capacitor value (microfarads)	0.5	0.5		
Maximum Safe current flow without function (microamps)	50	50		
	<u>Initial</u>	<u>Final</u>	<u>Initial</u>	<u>Final</u>
Resistance change during firing (ohms)	10	21.9	2	14.9

An analysis of the electrical characteristics of the T20E1 detonator is given in the Design Data Supplement.

Based on the above specifications, the trigger circuit was designed to provide about 0.05 joules to the squib in less than one microsecond. Because of the launch environment, an electronic rather than mechanical switch was required. A pulse transformer was incorporated to isolate the squib from possible current leakage paths. When the unijunction transistor type 2N490 fires, the 47 fd capacitor discharges through the transformer primary. The secondary of the transformer is matched to its two ohm load and delivers the 0.05 joule pulse in less than one microsecond.

The components were mounted inside a grooved circular plate of linen-base bakelite. This circular plate fitted into the annular region of the ring that contains the batteries. As in the case of the amplifier, the circuit was potted to withstand shock in excess of 10,000 g. Connections,

both electrical and mechanical, were made by utilizing feed-through posts.

#### 3.4.4.5 Power Supply

The power to operate the amplifier, trigger circuit and bias the detector, is provided by a battery of Mallory mercury cells.

The following potentials are available:

-40 volts unregulated	for controlled rectifier uni-junction transistor and detonation circuit.
-22 volts regulated	for linear amplifier and decision circuit
-28 volts regulated	for detector bias

The battery was connected to its circuits by conducting links at the back of the seeker. These links were put in place before firing. The positive terminal on the plate served as the common return for the signal power supply and casing. The connection to the casing is made through a spring loaded contact in the rear plate. The terminal board was placed at the back of the seeker for the convenience of test and preflight checkout.

#### 3.4.4.6 Seeker Functional Tests

Laboratory tests were conducted to demonstrate the functional performance of the seeker. The test set-up and procedure for the tests are given in the Design Data Supplement.

The seeker field of view was measured by noting the response of the system as the lens-cell combination looked at a point source of 2000 cycle light. The head was rotated about an axis perpendicular to the plane containing the optic axis and the projectile axis. The point source of light was also in this plane. Rotation of the head about the perpendicular axis allowed the image of the spot to traverse the cell. After the image passed

the cell, the head was rotated 180 degrees about the projectile axis. As the head was farther rotated about the perpendicular axis, the spot image again traversed the cell. Figures 3.4-23 and 3.4-24 show the optical response for four seekers. This response remained unchanged after air gunning.

Tests were performed with the cell-amplifier combination and the results given in the form of frequency response in figure 3.4-25. The low frequency slope of all of the POLCAT amplifiers was very close to -14 db/octave and the high frequency slope approximately -19 db/octave. There was no change in this characteristic after the air gun tests.

Tests were conducted to establish the reliability of the squib detonating circuit and its behavior with a semiconductor switch, together with a transformer, used as an energy source.

To determine a margin of safety for operational use, the supply potential was varied from 20V dc to 40V dc. In addition, the value of the storage capacitor was varied from 5  $\mu$ f to 70  $\mu$ f. The experiment was performed at every value of voltage and capacity five times in order to see if any variation in results will be indicated with the different units. Forty squibs were chosen at random without measuring their resistance. This assured there would be no change in characteristic by passing current through them. A plot of the voltage across the squib versus time after application of the pulse is shown for the various settings of voltage and capacity in figure 3.4-26.

From the scope patterns it seems that, as the supply voltage decreases, the firing time increases, and the voltage across the squib decreases. These results indicate that the trigger circuit in the POLCAT system should function

reliably if the same type squib is used as the one tested.

#### 3.4.5 Seeker Field Tests

A POLCAT seeker was subjected to captive tests in the field. An illuminator-target-receiver configuration was used which simulated conditions under which a firing demonstration could be held. The purpose of the test was twofold. The received signal to noise ratio was determined for a variety of system and operational parameters; and the effect of the non-point source reflector on the guidance firing angle was determined.

##### 3.4.5.1 Instrumentation

A POLCAT Seeker Head Mod 1 was modified to permit monitoring the output of the amplifier and trigger circuit separately. An external power supply was used to permit operation for long periods. Figures 3.4-27 and 3.4-28 show plots of the instantaneous field of view. Figure 3.4-29 shows the total field of view generated by offsetting and rotating the instantaneous field of view.

A spin rig was constructed which permitted spinning the seeker head about its longitudinal axis at 10 rps or 20 rps. Since guidance angle measurements were made to an accuracy of 1 milliradian, the alignment of components and vibration were maintained to less than 1/4 milliradian. Because of the accuracy required of the measurements, much attention was given to the alignment procedure. A very sensitive, yet convenient method of simultaneously aligning the seeker longitudinal axis, bore-sight telescope and mortar sight in the field was devised.

The target was illuminated by the POLCAT illuminator described in Section 3.4.3.1. This unit was mounted on a jeep which facilitated changing

the illuminator-target distance to vary the spot size.

A 7' x 7' lenticular screen target was set up at the test range. This was irradiated by the POLCAT illuminator. The spin rig and seeker head were located suitably near the target so as to simulate the POLCAT projectile terminal geometry. The setup permitted flexible arrangement of the various system elements. Measurements were made for the following conditions:

Target-receiver distance	75 feet and 200 feet
Illuminated spot diameter	6 feet and 18 inches
Seeker spin rate	10 rps and 20 rps

This type of target was chosen in order to be certain that sufficient signal strength would be achieved. A lenticular screen reflects almost 100 percent of the incident energy into an angle of less than a steradian.

#### 3.4.5.2 Test Results

In order to establish that the POLCAT seeker head was capable of performing its guidance functions, the field tests (22) were executed to determine

- a) signal-to-noise ratio
- b) errors in measurement of guidance angle

Measurements were made for various combinations of target-receiver distance, illuminated spot size and seeker spin rate. The seeker signal channel was monitored at both the output of the linear amplifier and at the output terminals (firing signal).

The signal-to-noise ratio was determined by first measuring the seeker response to the energy reflected from the target without presence of background noise and then determining the amplitude of the noise voltage

without the target signal.

The pure target signal was measured by locating the maximum output from the non-spinning seeker.

The pure noise signal was measured by locating the maximum output from the spinning seeker with the illuminator turned off.

The trigger level was set so that no firing signal was generated as the field was scanned.

The angle at which the spinning seeker should be offset to locate a modulated point source was determined in the laboratory and given in figure 3.4-29. Any deviation from this angle due to noise or illuminated spot size is the guidance angle error.

With the target illuminated and the trigger level properly set so that no false alarms would be generated by the background, the seeker was offset from the target in various directions and slowly scanned towards the target. As soon as a firing signal was generated, the offset angle was recorded. The difference between this offset angle and the one measured in the laboratory is the guidance angle error. The complete test plan is given in the Design Data Supplement.

When comparing the results of the various measurements, attention must be given to the climatological conditions under which the runs were made. The following tabulation gives the weather data at the test site for the period during which the runs were made.

<u>Target-Receiver Distance in Feet</u>	<u>Illuminated Spot Size</u>	<u>Date</u>	<u>Time in Hours</u>	<u>Temp F</u>	<u>Relative Humidity Percentage</u>	<u>Pressure mm of Hg</u>
75	6 feet	6/18/62	1600-1730	89	50	29.78
75	18 inches	6/19/62	1420-1600	90	53	29.60
200	6 feet	6/20/62	1100-1300	78	82	29.66
200	18 inches	6/20/62	1500-1600	76	72	29.65

The photographs in figure 3.4-30 show signals obtained during a typical measurement. The signals were recorded as peak-to-peak values. To obtain the  $S_{rms}/N_{rms}$  the sinusoidal signal voltages were divided by 2.8 and the random noise voltages were divided by 4.5. The signal-to-noise ratios obtained in test are given below.

<u>Test</u>		<u><math>S_{rms}/N_{rms}</math></u>	
<u>Target-Receiver Distance</u>	<u>Illuminated Spot Size</u>	<u>Spin Rate 10 rps</u>	<u>Spin Rate 20 rps</u>
75 feet	6 feet	6.68	4.75
75 feet	18 inches	27.5	23.8
200 feet	6 feet	2.68	2.68
200 feet	18 inches	4.0	4.0

The target signal falls off as expected as the target-receiver distance increases. An inverse square attenuation predicts a relation between the signals at 200 ft and 75 ft of about 1/7. This relation holds quite well for the small spot size but not for the six foot diameter illuminated area. This may be due to the reflectivity pattern of the lenticular screen or atmospheric effects since the tests 6-75 and 6-200 were performed on

different days.

Figure 3.4-31 shows a photograph of the output signal of the amplifier as the line of sight scans past the target causing the trigger circuit to function.

The curves in figures 3.4-32 show the line of sight angles at which the firing signal occurred as compared with the preset offset angle.



Figure 3.4-3 Signal to Noise Ratio as a Function of False Alarm Rate and Number of Pulses

- recognition probability of 98 percent
- $n$  = number of pulses in signal

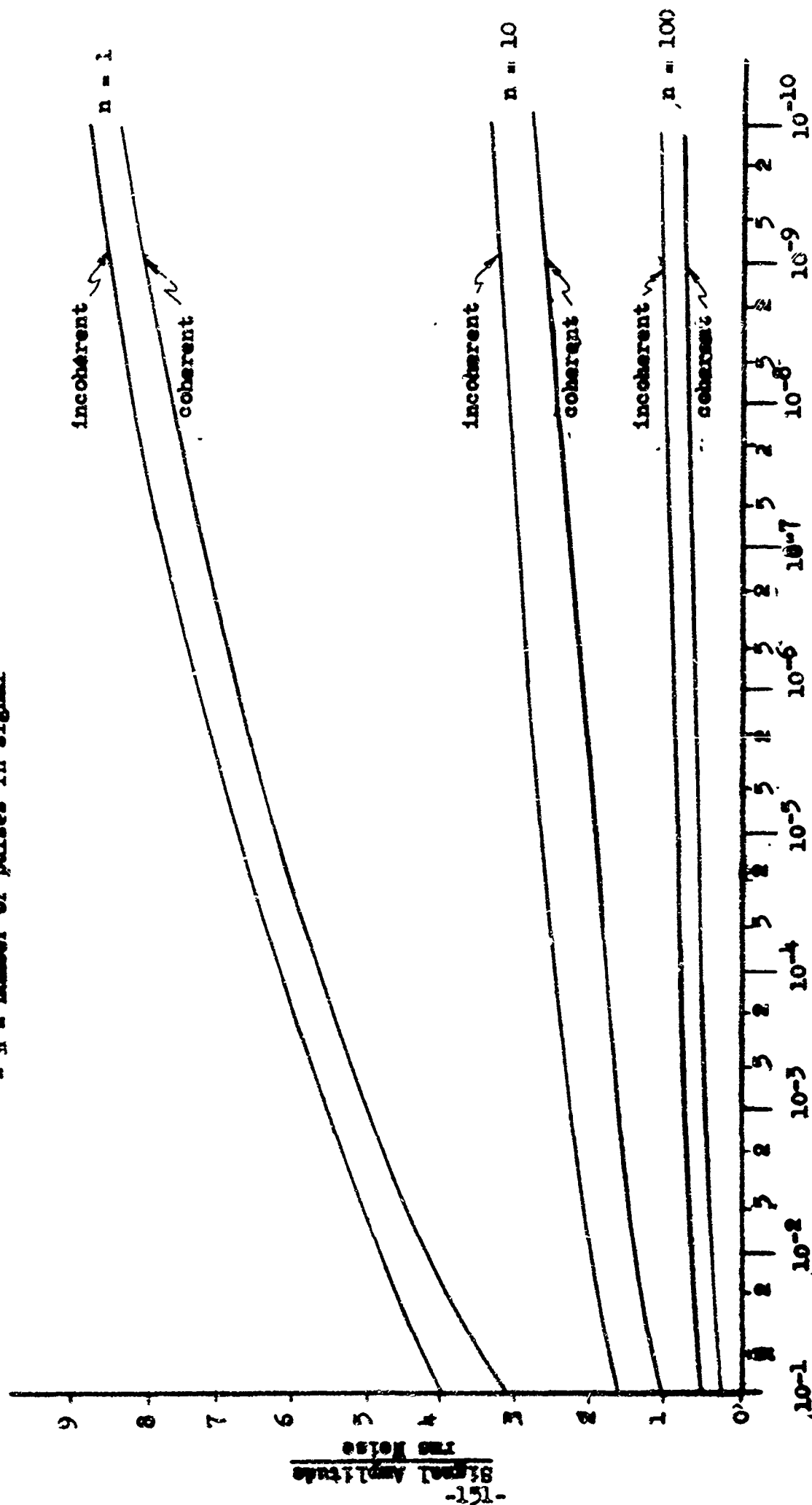


Figure 3.4-4 Spectrum of Noise Current in Semiconductors

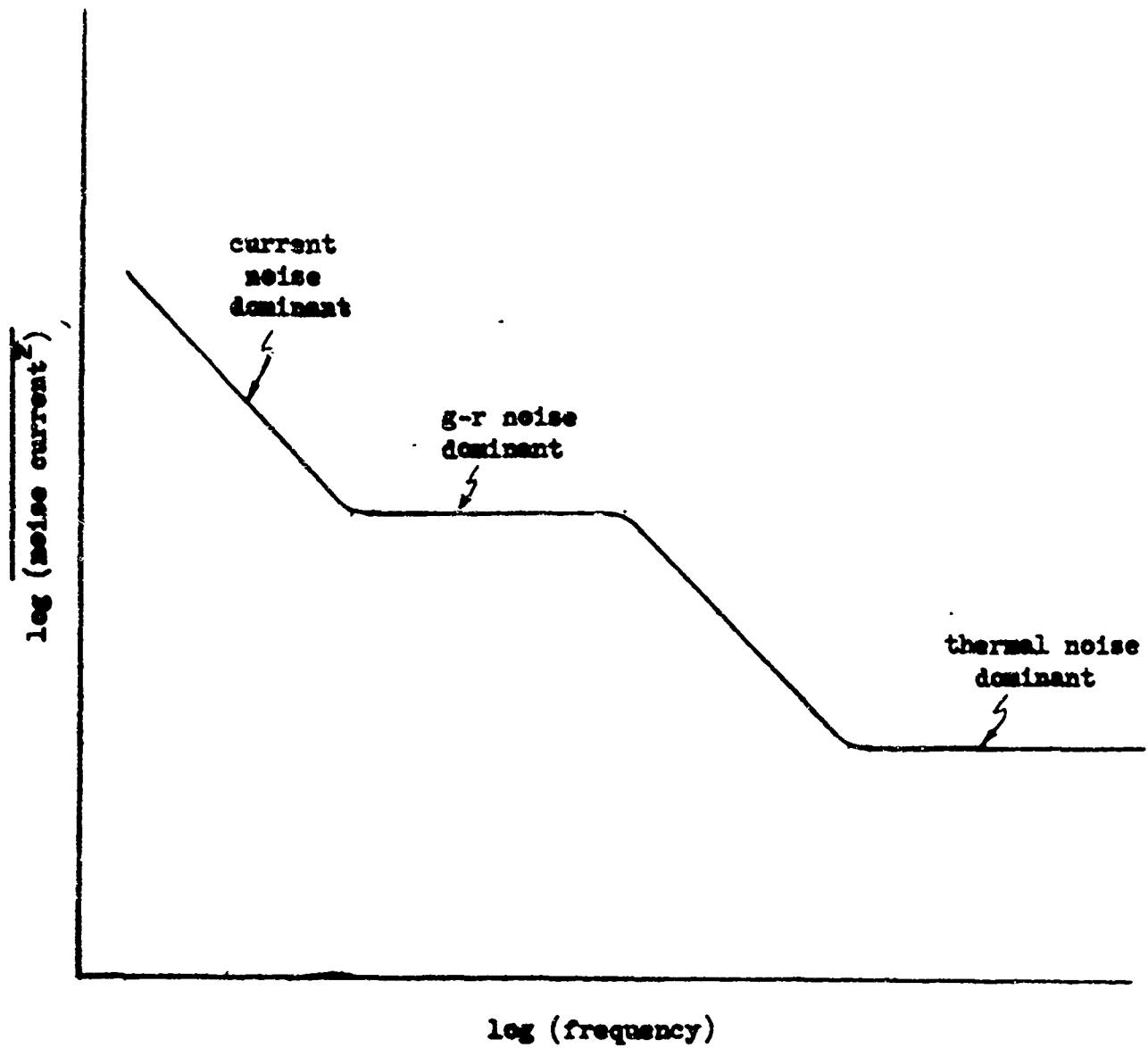


Figure 3.4-5 Empirical Frequency Spectrum of Light Intensity Fluctuation for Different Wind Velocities

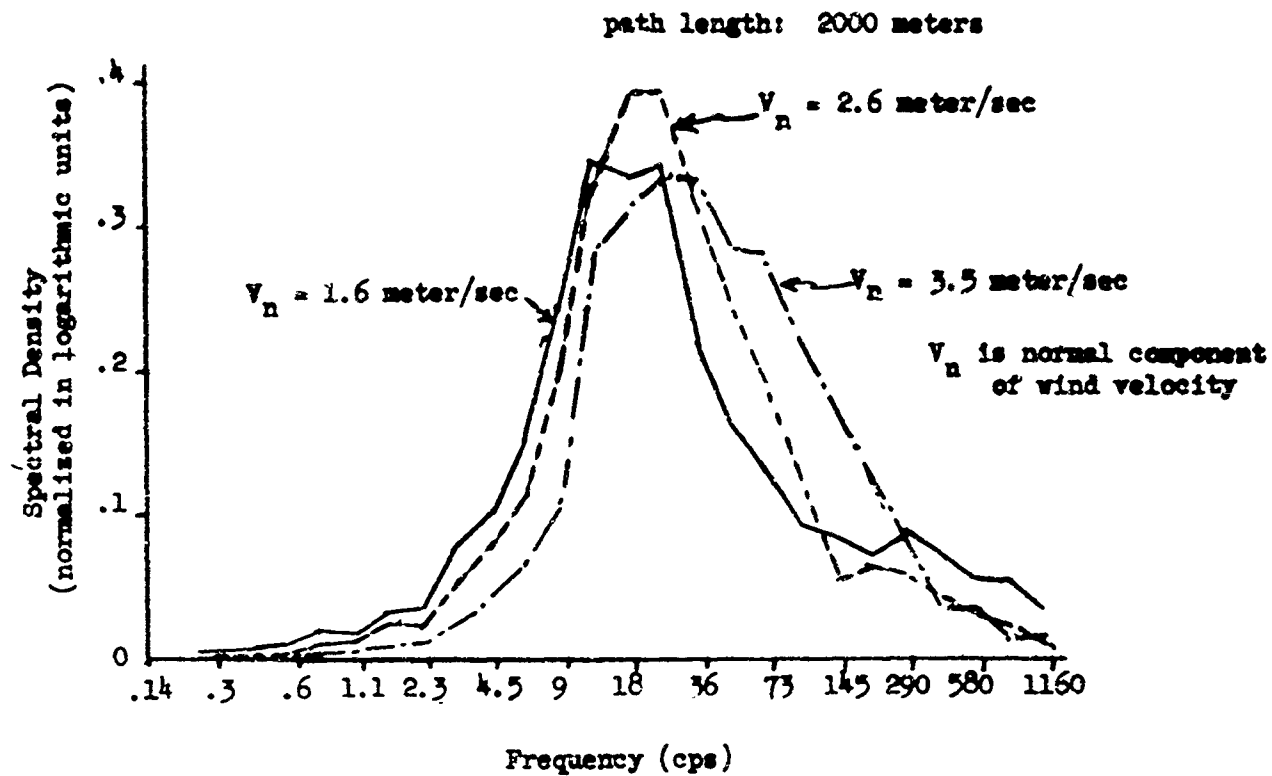
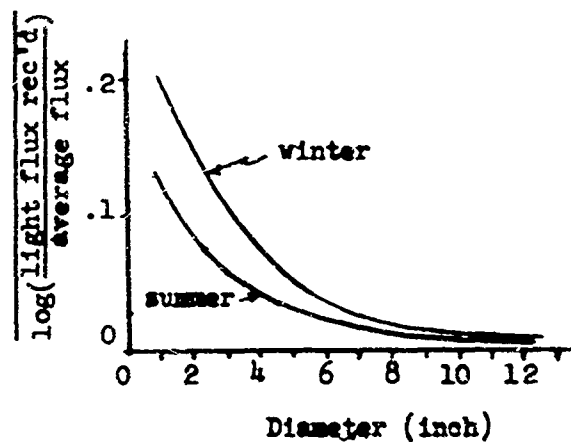


Figure 3.4-6 Empirical Dependence of Amount of Twinkle on Diameter of Telescope Diaphragm





Scene 3  
8/17/60 1135-1500  
22.75°C RH 55%  
No Clouds - Haze



Scene 5  
8/18/60 1209-1306  
24.25°C RH 59%  
Clear-Bright Sun-High Thin Clouds



Scene 8  
8/23/60 1050-1230  
20.5°C RH 70%  
Bright Sun-High Thin Clouds



Scene 10  
8/26/60 1220-1400  
23°C RH 62%  
Clear-Bright-Sun

Figure 3.4-7. Typical Background Terrain

Figure 3.4-6 Terrain Background Spectral Density Function

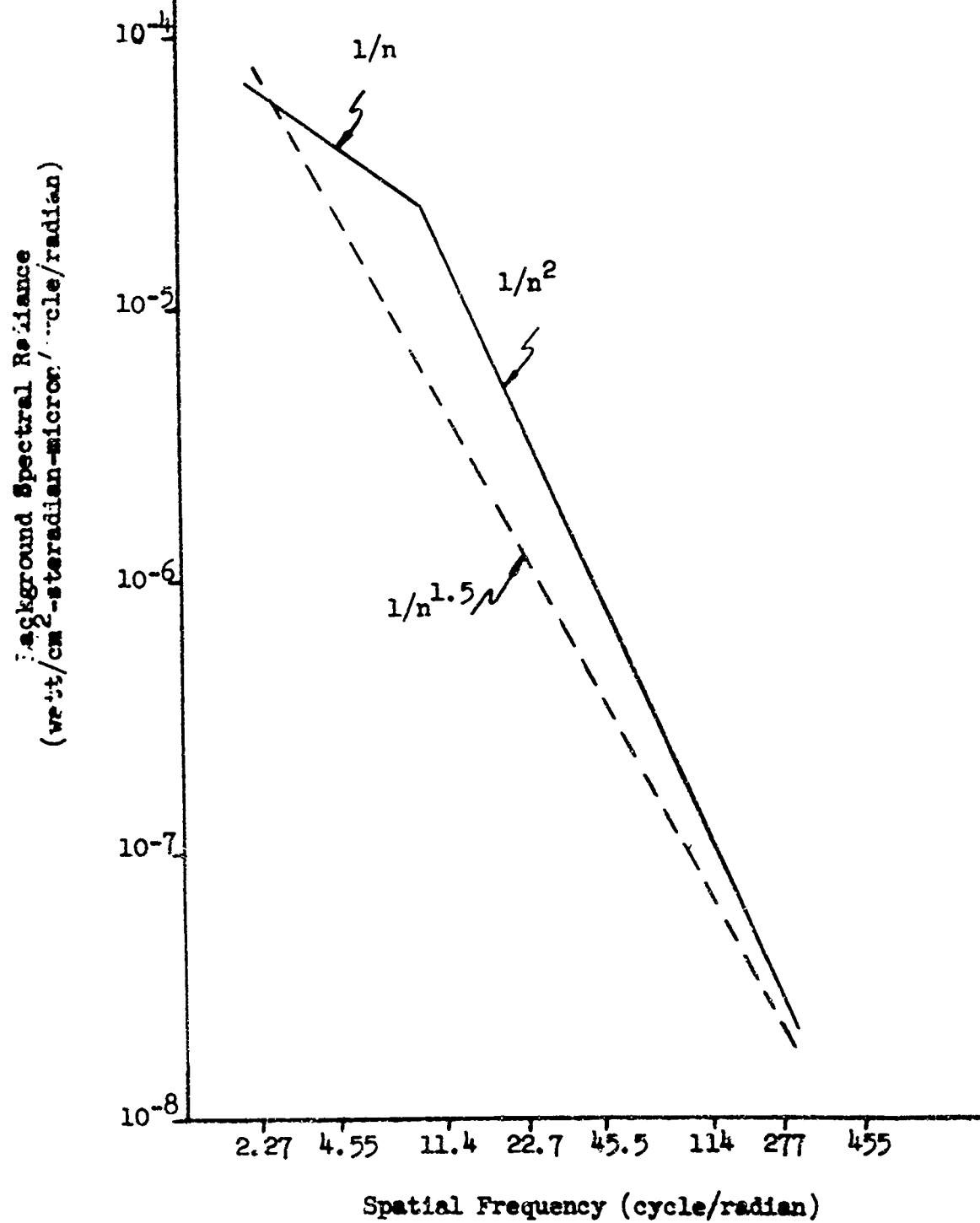
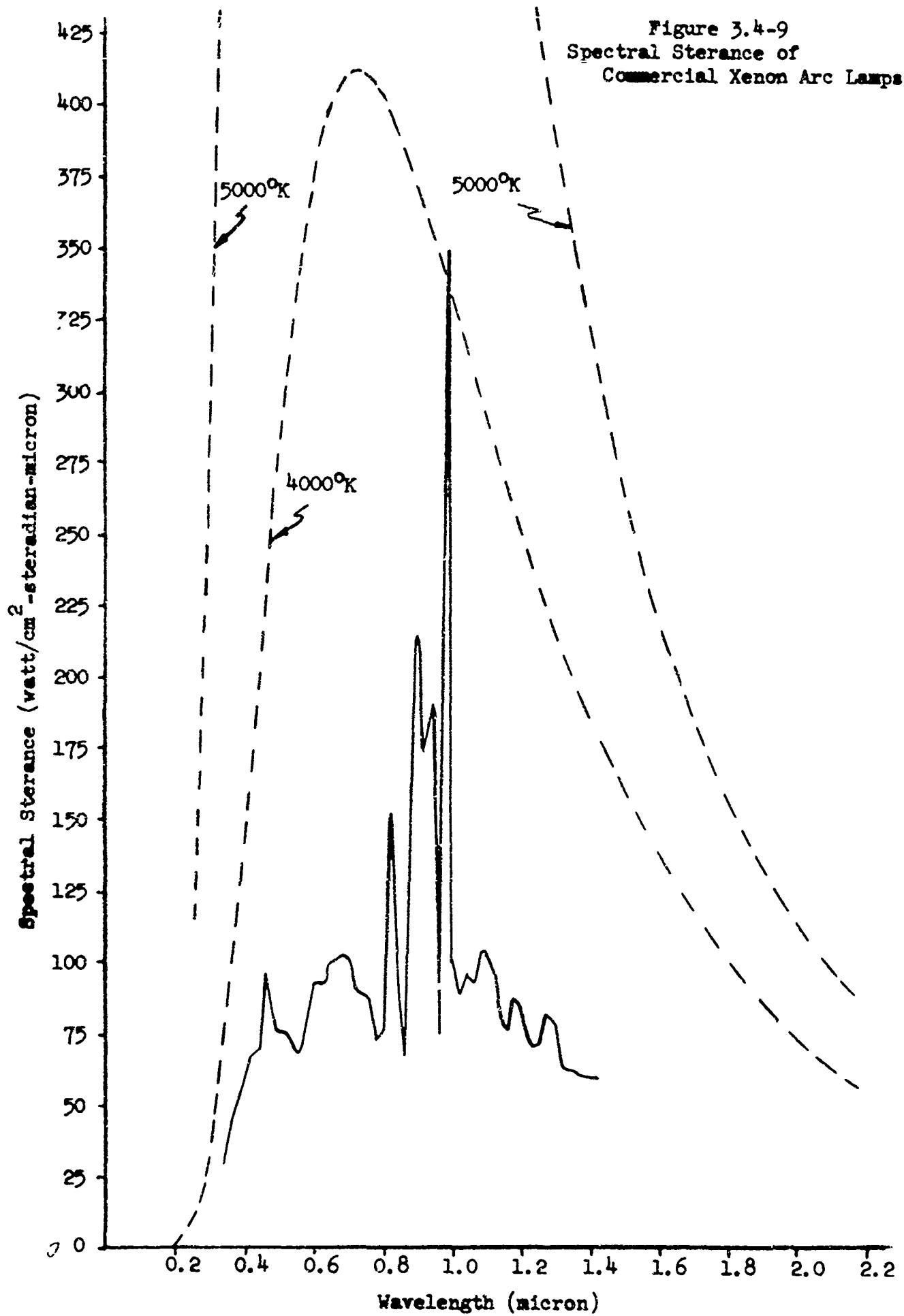


Figure 3.4-9  
Spectral Sterance of  
Commercial Xenon Arc Lamps



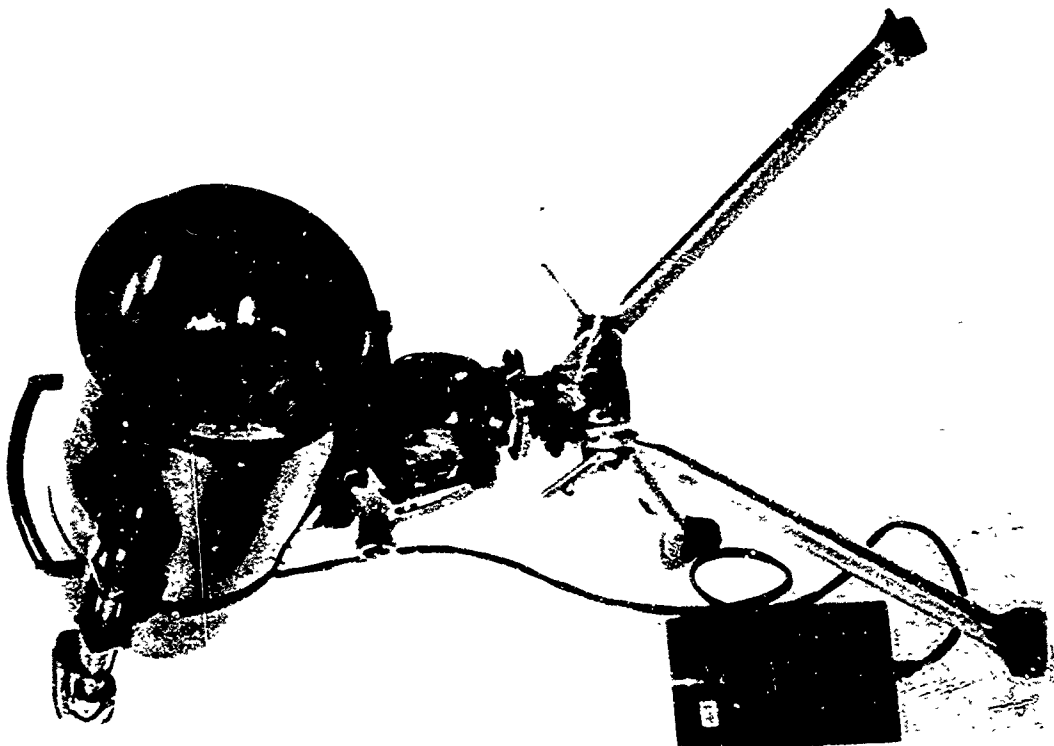
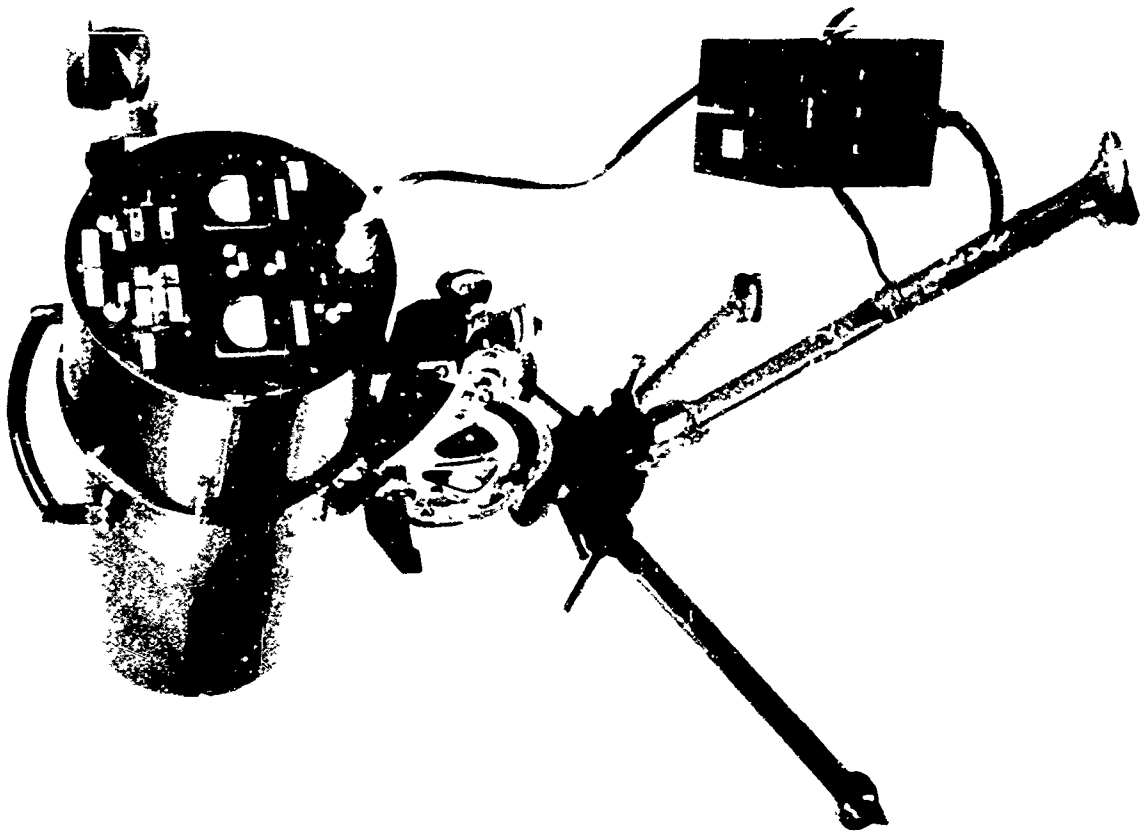
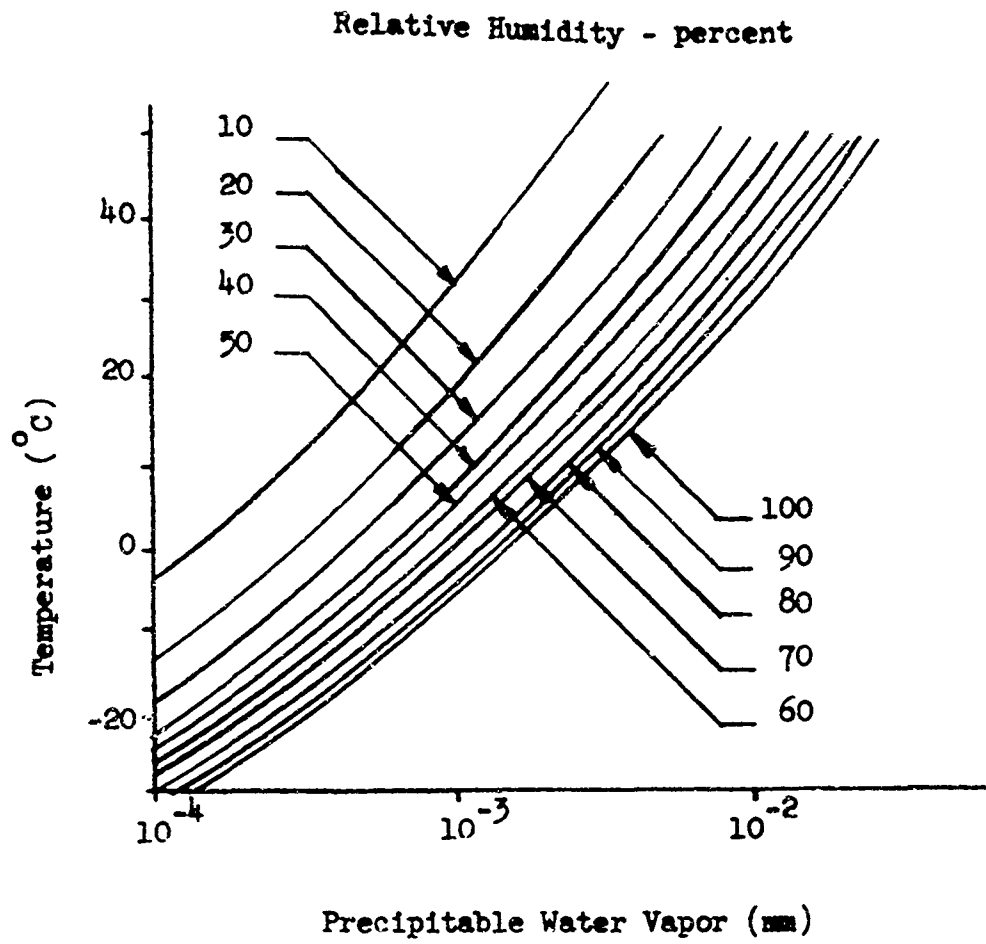


Figure 3.4-10. POLCAT Illuminator

Figure 5.4-11 Precipitable Water Vapor per foot of Path Length as a Function of Temperature and Relative Humidity





Curve	Path Length	Date	Time	Temp.	R.H.	Precipitable Water	Visual Range
A	1000 ft	3-20-56	3 P.M.	37° F	62%	1.1 mm	22 miles
B	3.4 miles	3-20-56	10 P.M.	34.5° F	47%	13.7 mm	16 miles
C	10.1 miles	3-21-56	12 A.M.	40.5° F	48%	52.0 mm	24 miles

#### Window Definitions

I	0.72 to 0.94 $\mu$	V	1.90 to 2.70 $\mu$
II	0.94 to 1.13 $\mu$	VI	2.70 to 4.30 $\mu$
III	1.13 to 1.38 $\mu$	VII	4.30 to 6.0 $\mu$
IV	1.38 to 1.90 $\mu$	VIII	6.0 to 15.0 $\mu$

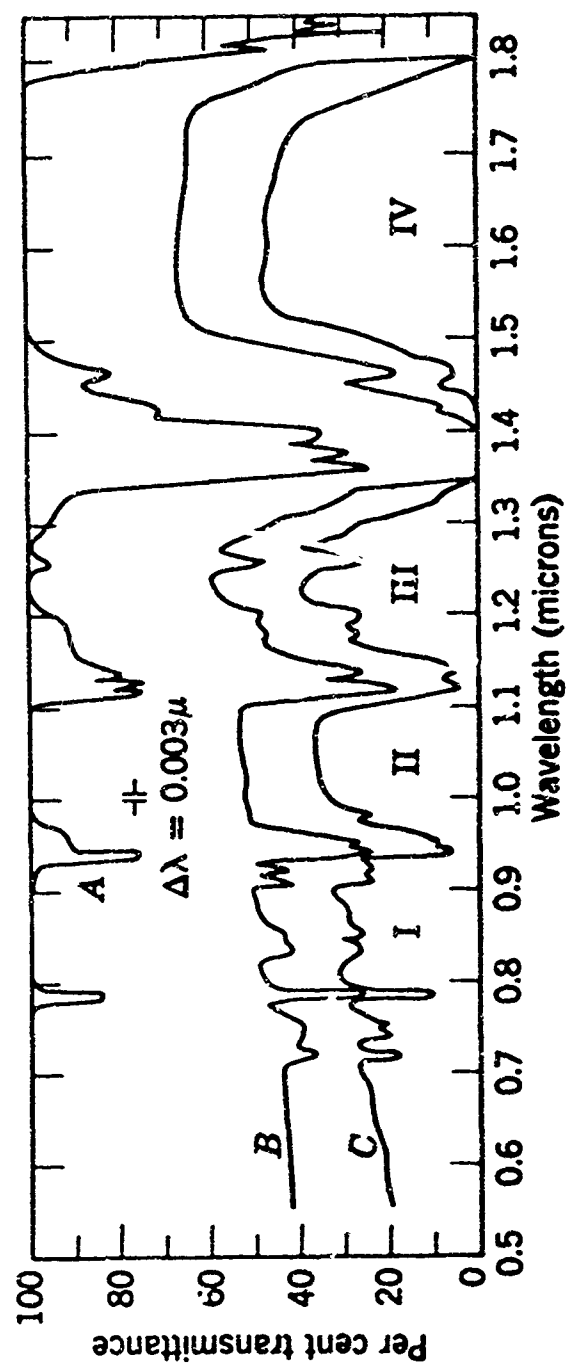
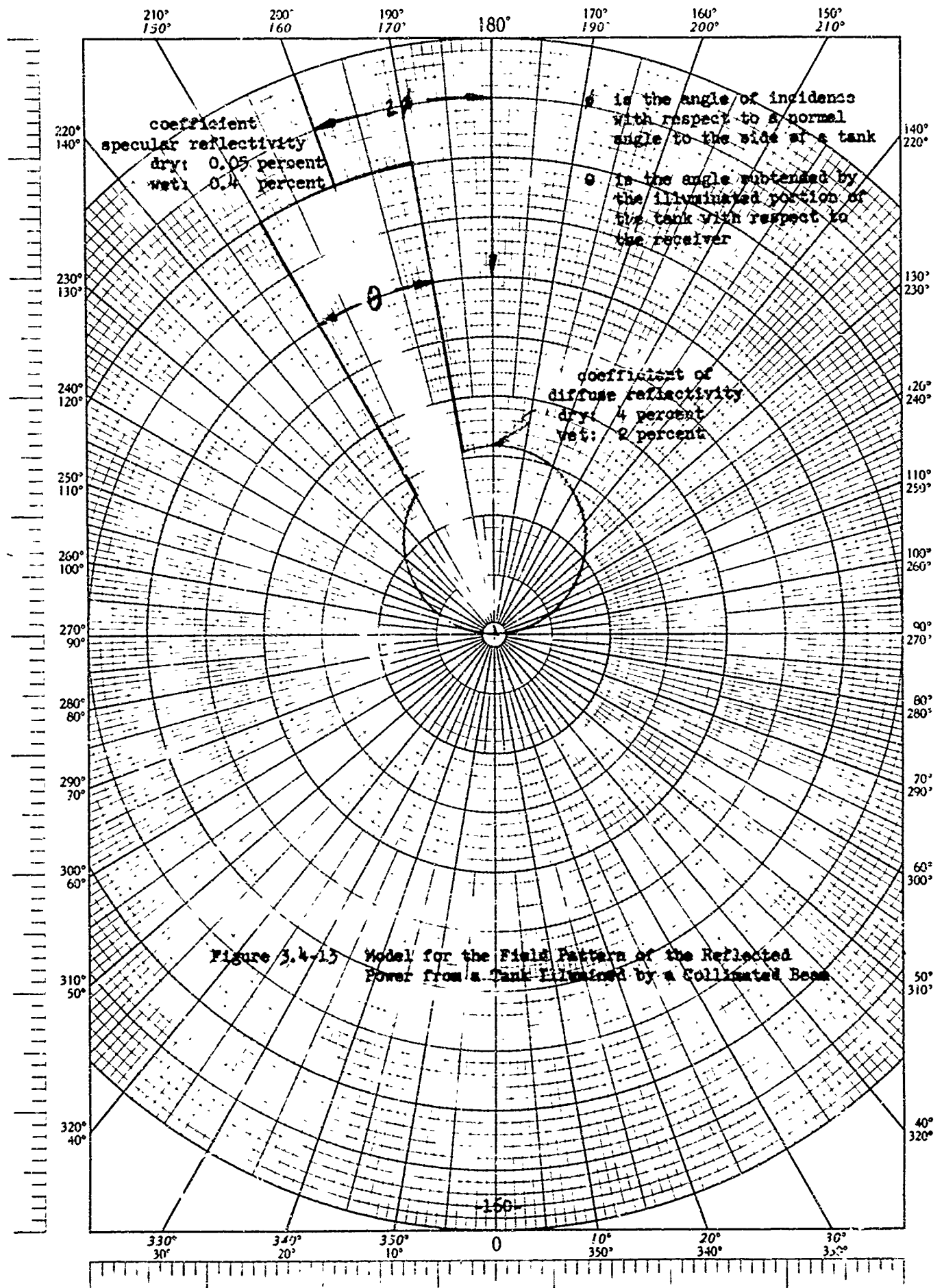
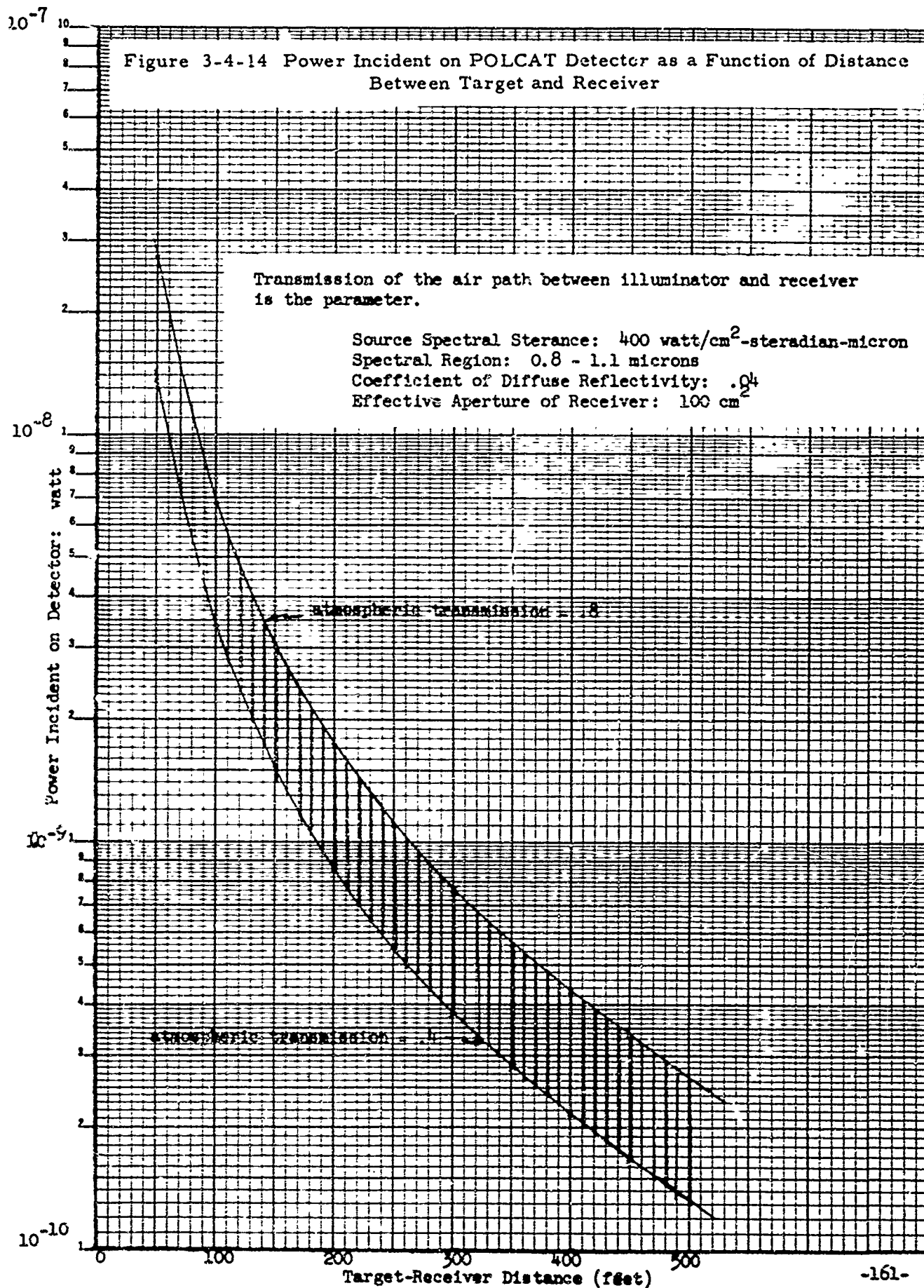


Figure 3.4-12. Measured Atmospheric Transmission





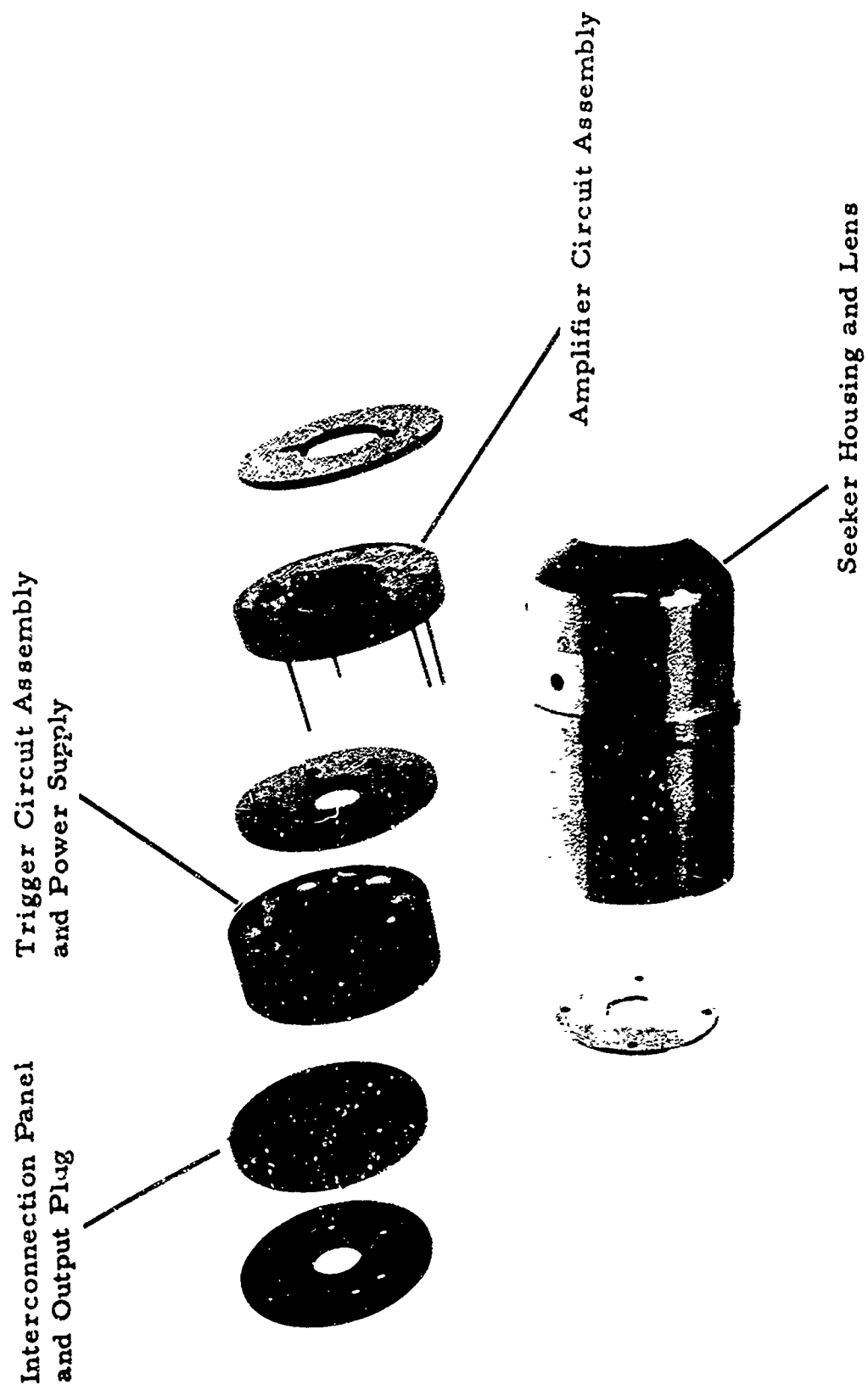


Figure 3.4-15. POLCAT Seeker

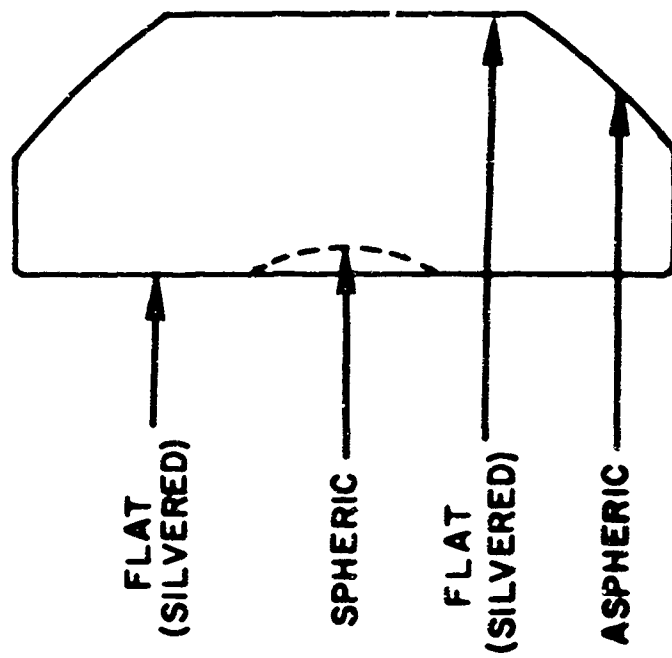
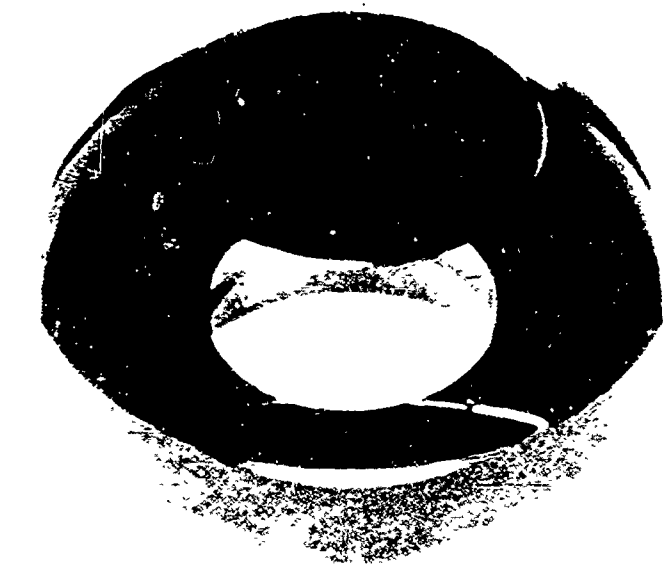


Figure 3.4-16. Seeker Lens

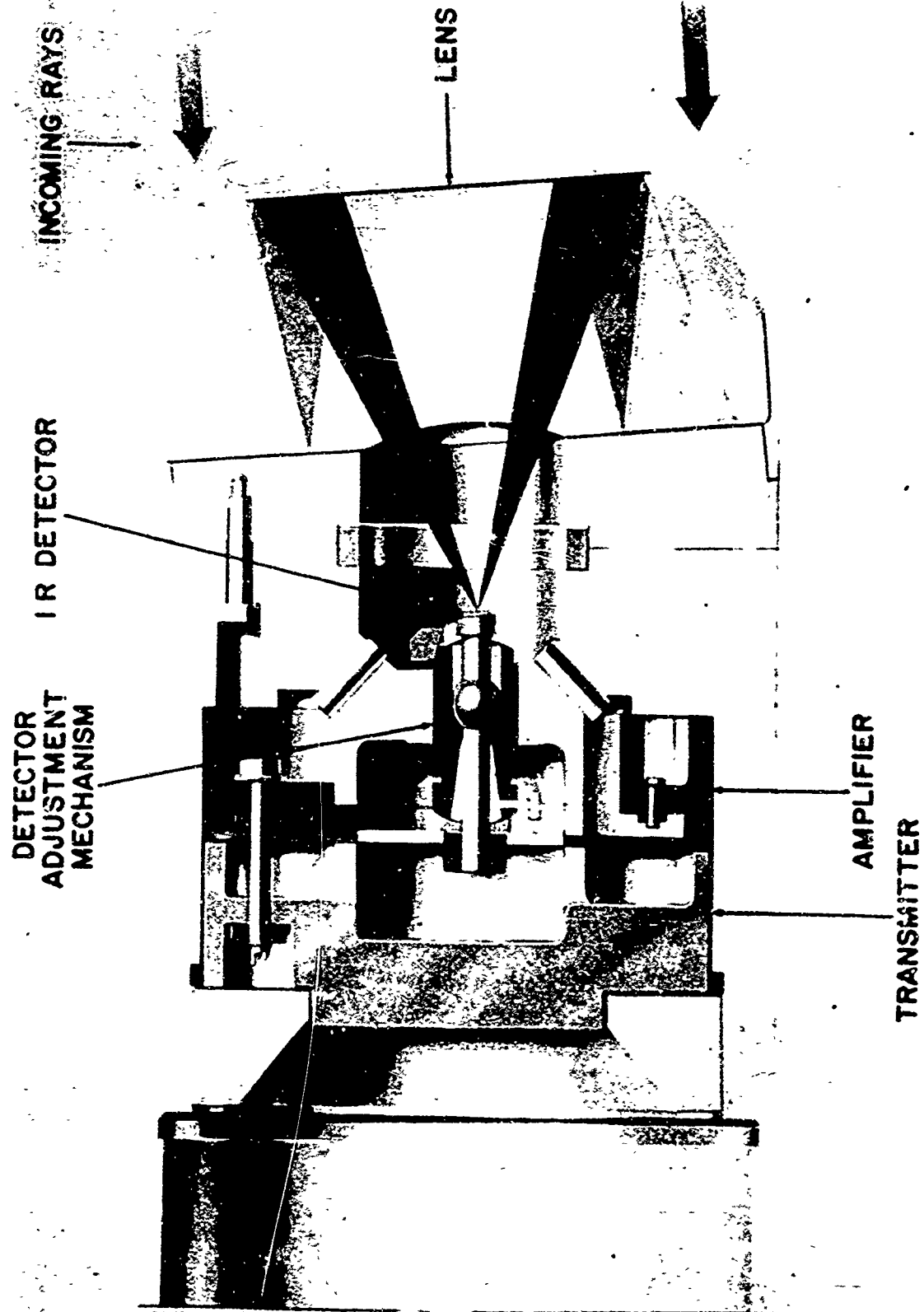


Figure 3.4-17. Optic Detector Arrangement

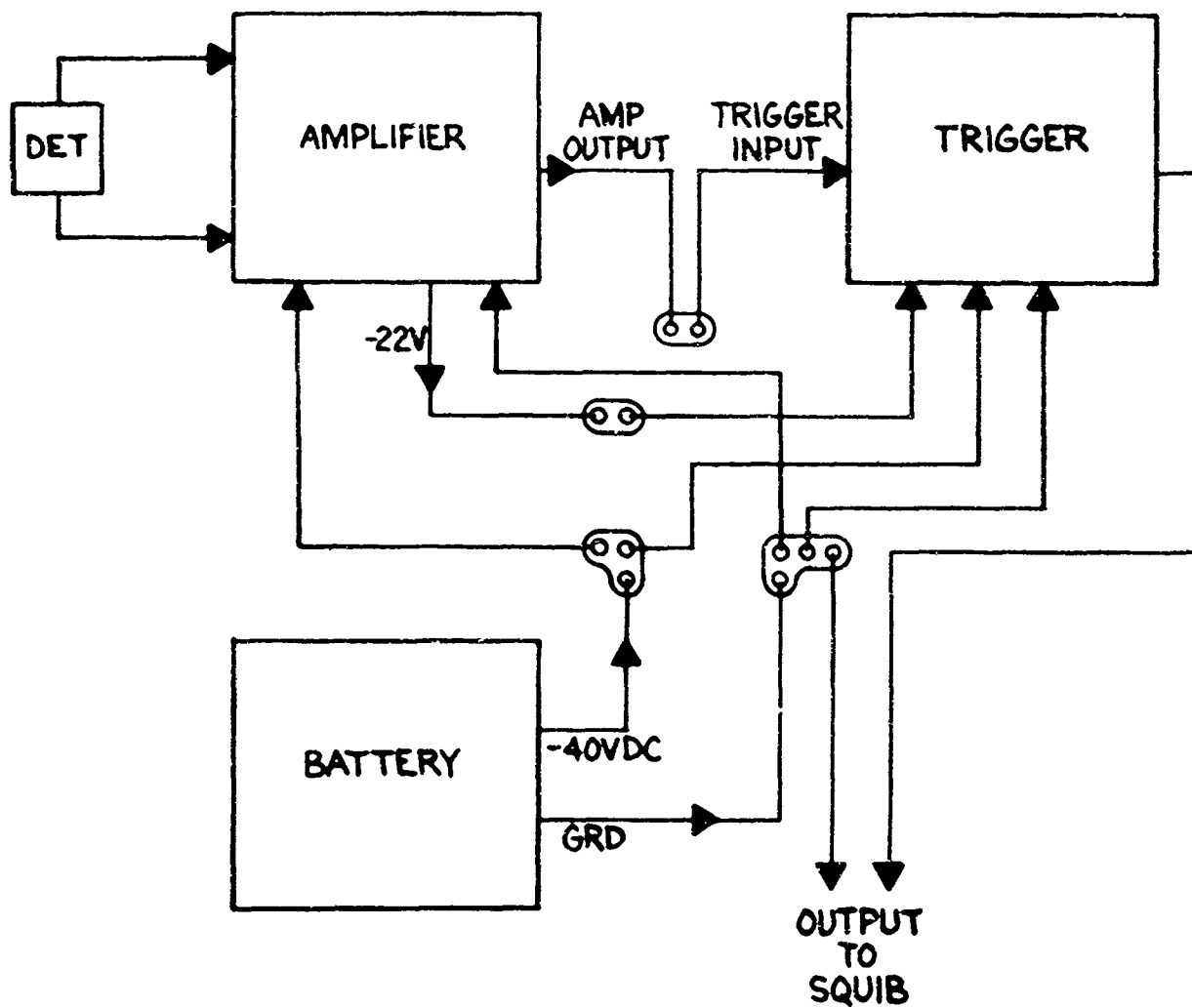


Figure 3.4-18. Seeker Block Diagram

Figure 3.4-19 Signal Energy Density Function

4 cycle train modulated at 2000 cps

$$\frac{\sin 4\pi(f/f_0 - 1)}{4\pi(f/f_0 - 1)} + \frac{\sin 4\pi(f/f_0 + 1)}{4\pi(f/f_0 + 1)}$$

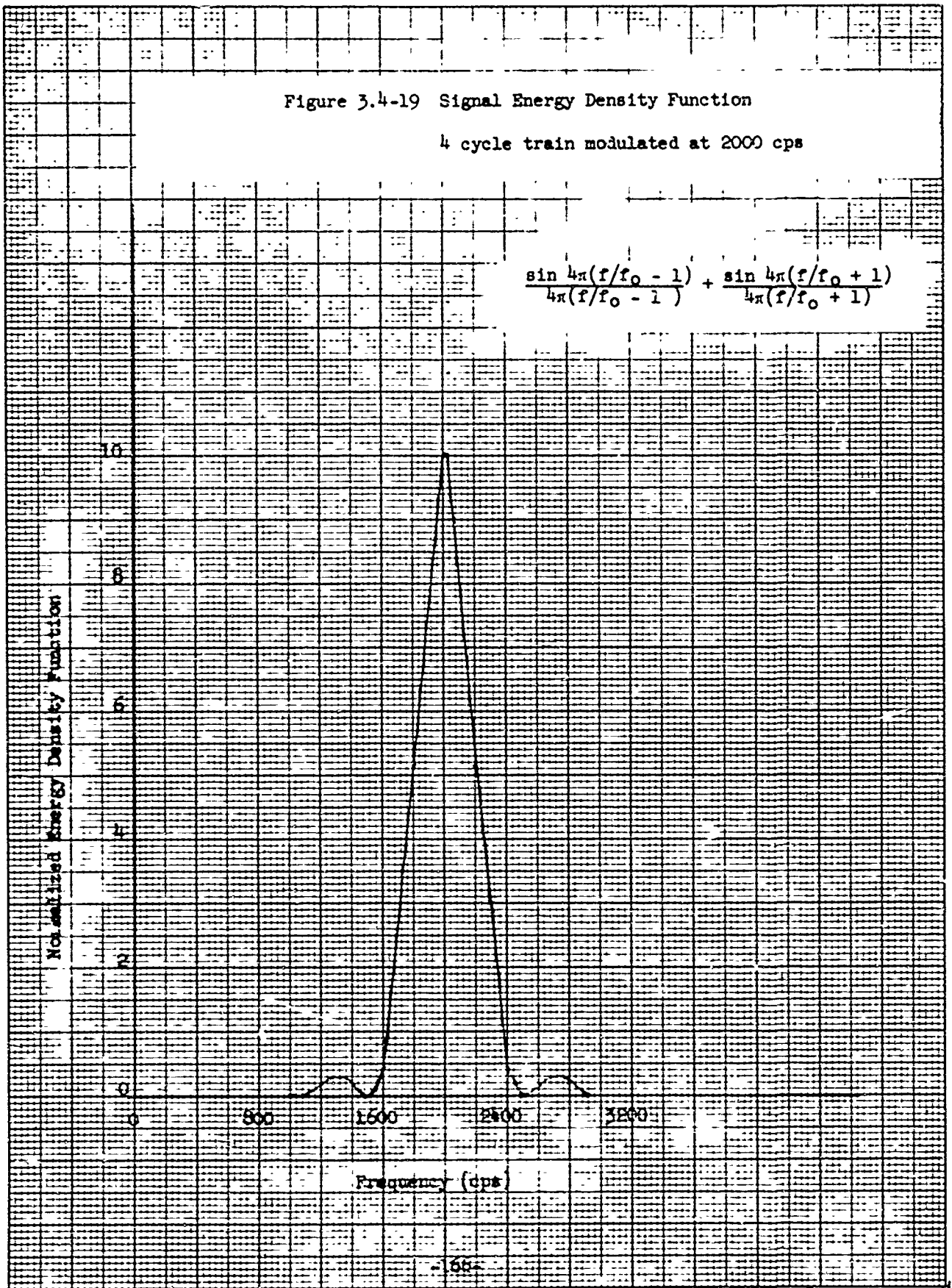
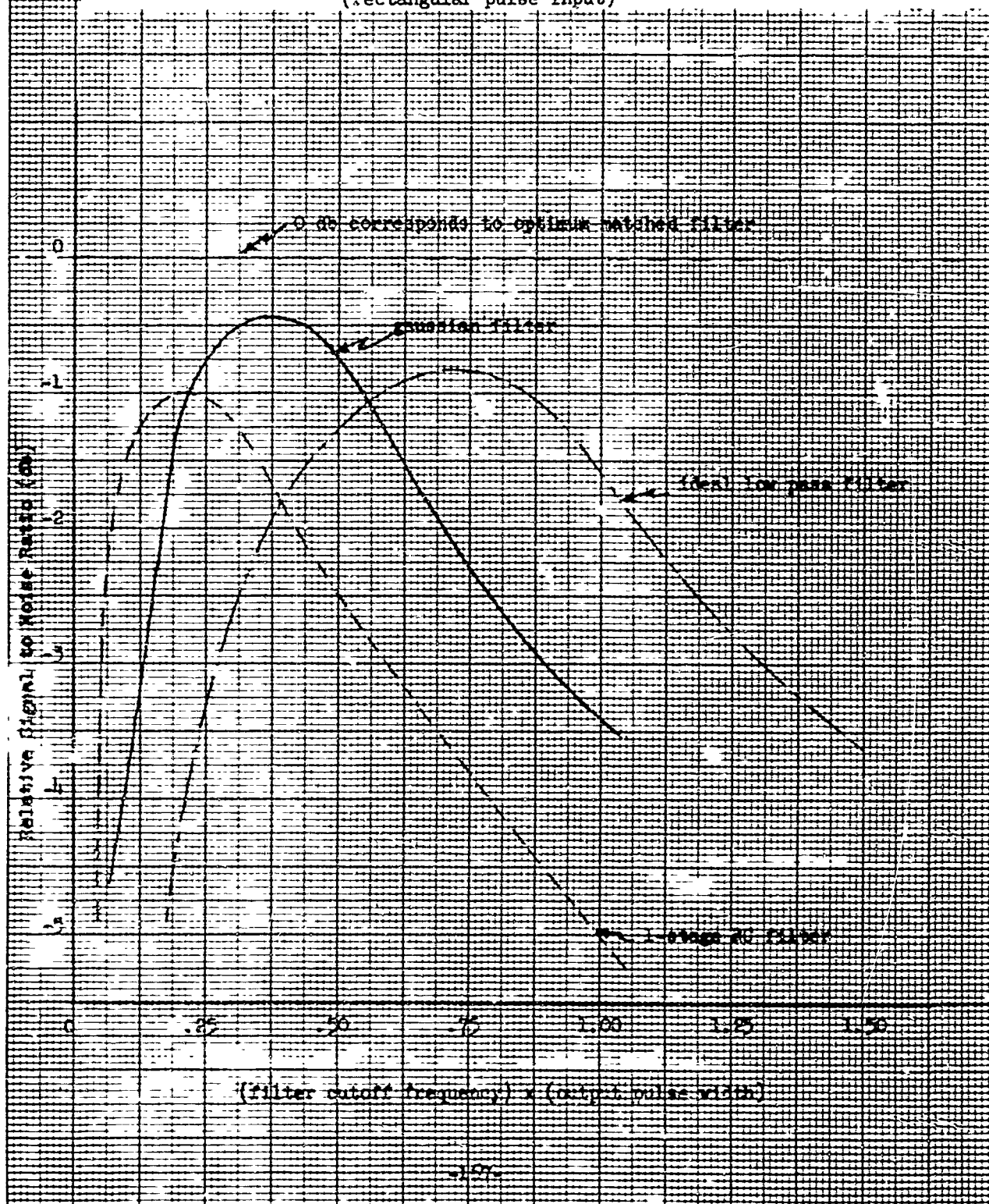




Figure 3.4-20 Peak SNR for Various Filters Compared with Matched Filter  
(rectangular pulse input)





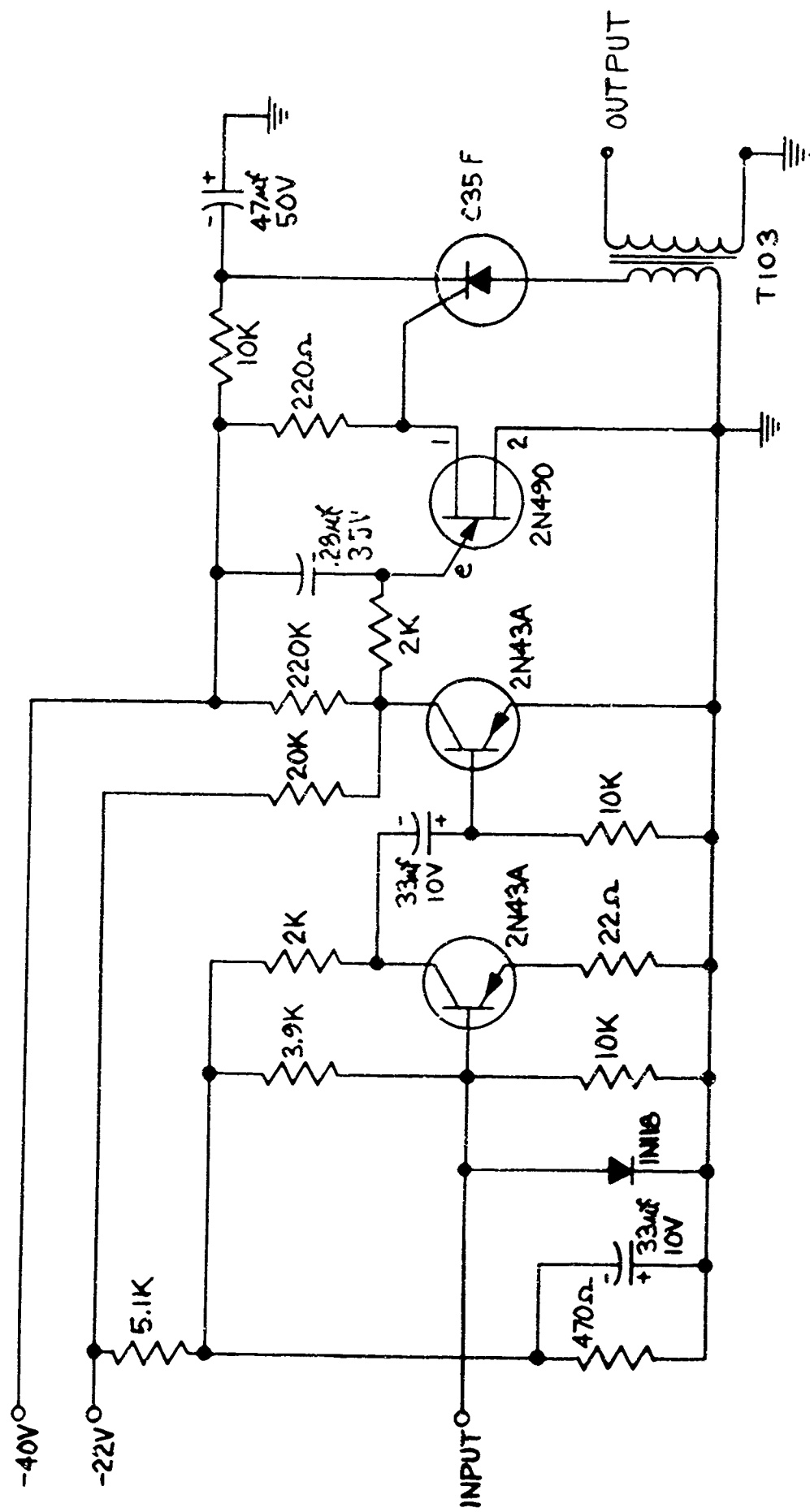
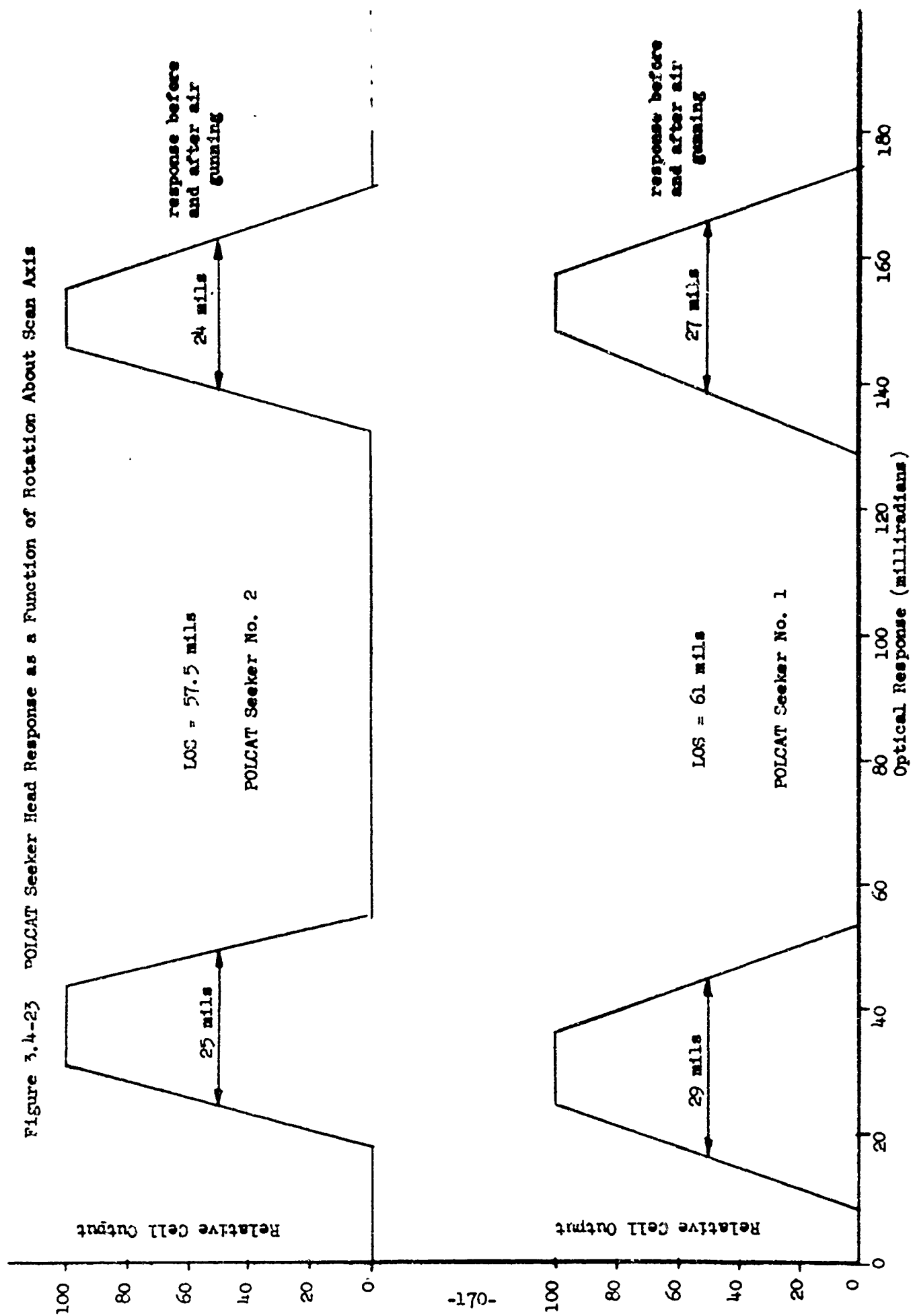


Figure 3.4-22. Trigger Circuit Schematic

Figure 3.4-23 POLCAT Seeker Head Response as a Function of Rotation About Scan Axis



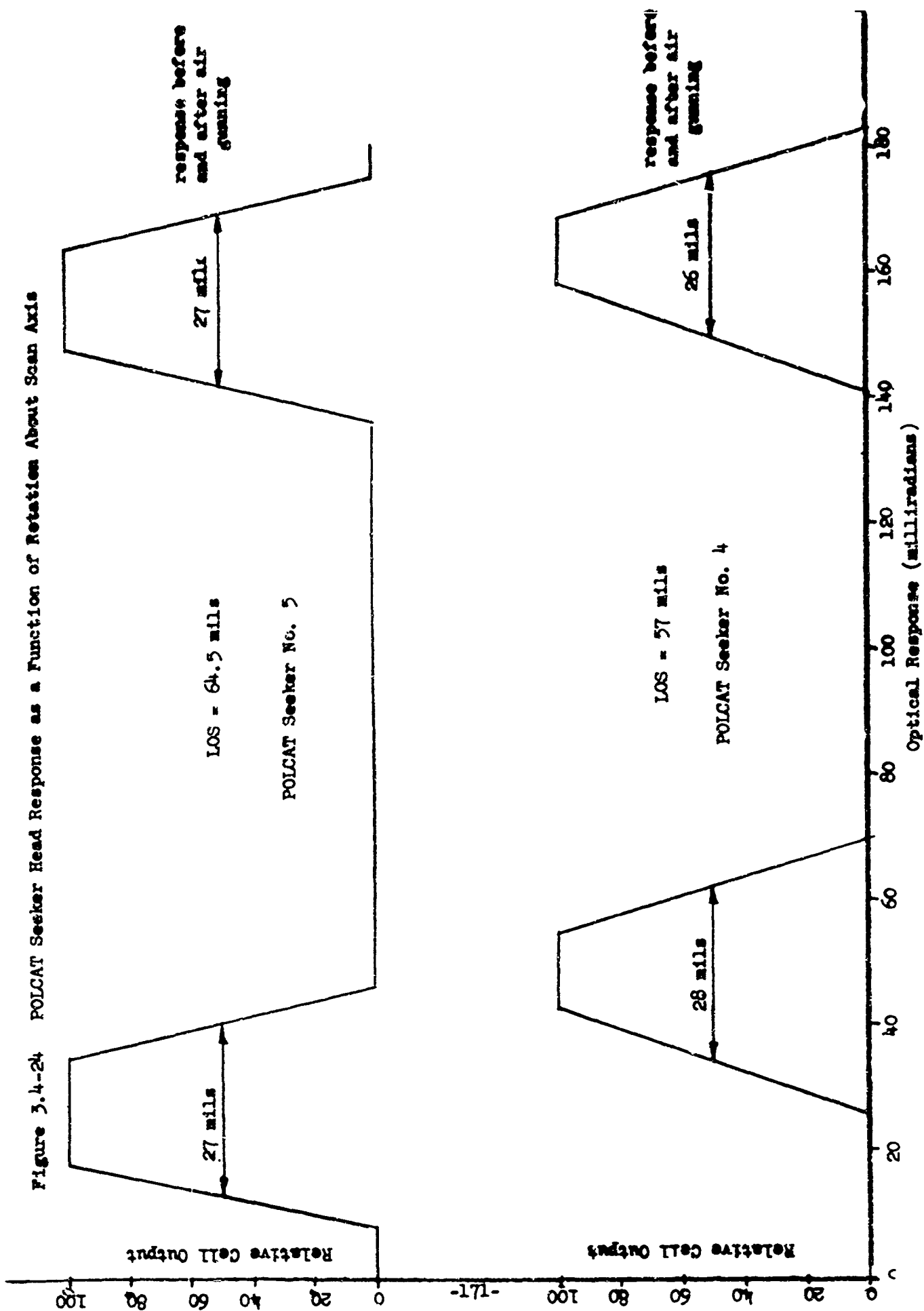
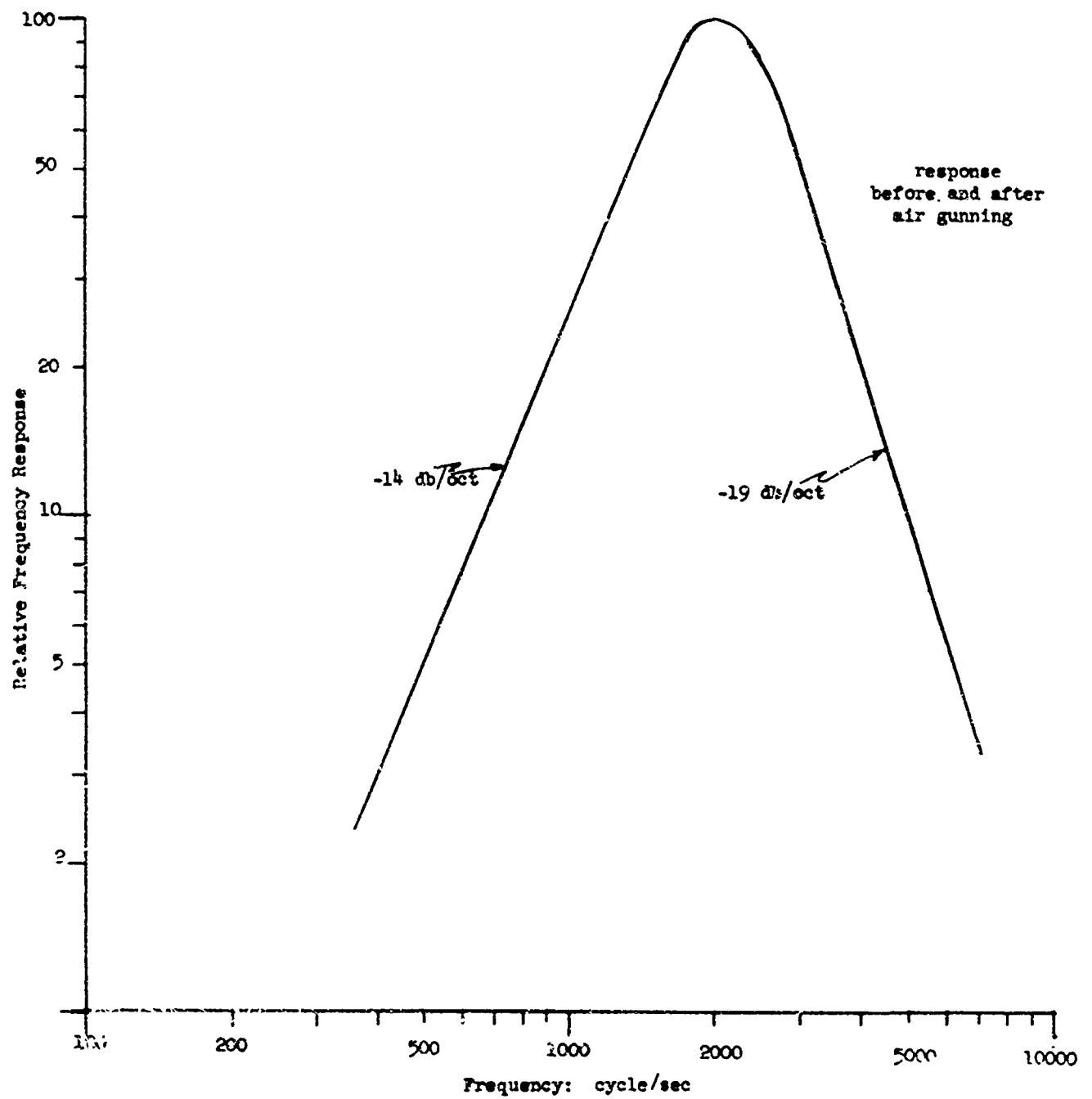
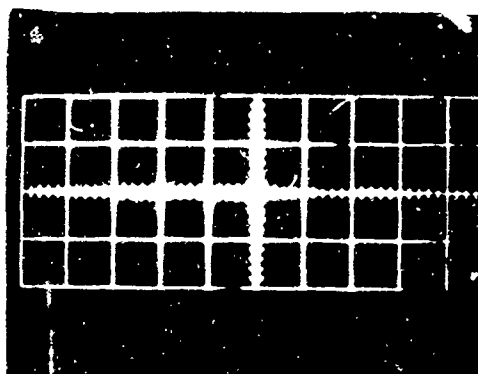


Figure 3.4-25 Cell Amplifier Combination Frequency Response for Typical POLCAT Seeker





SCALE



10 V/cm

2  $\mu$  sec/cm

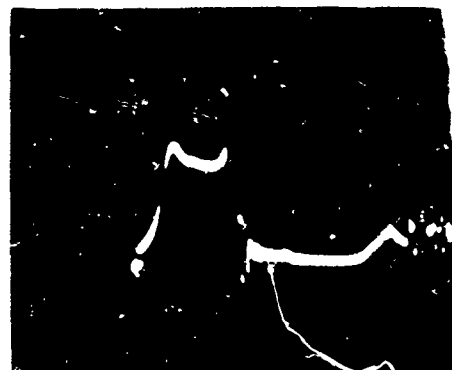
Supply Voltage - 20 VDC  
Capacitance - 5  $\mu$ f



20 V/cm

2  $\mu$  sec/cm

Supply Voltage - 25 VDC  
Capacitance - 78  $\mu$ f



20 V/cm

2  $\mu$  sec/cm

Supply Voltage - 25 VDC  
Capacitance - 5  $\mu$ f



20 V/cm

2  $\mu$  sec/cm

Supply Voltage - 36 VDC  
Capacitance - 5  $\mu$ f



20 V/cm

2  $\mu$  sec/cm

Supply Voltage - 36 VDC  
Capacitance - 78  $\mu$ f

Figure 3.4-26. Squib Voltage vs. Time After Signal Pulse

Figure 3.4-27 Instantaneous Field of View

horizontal

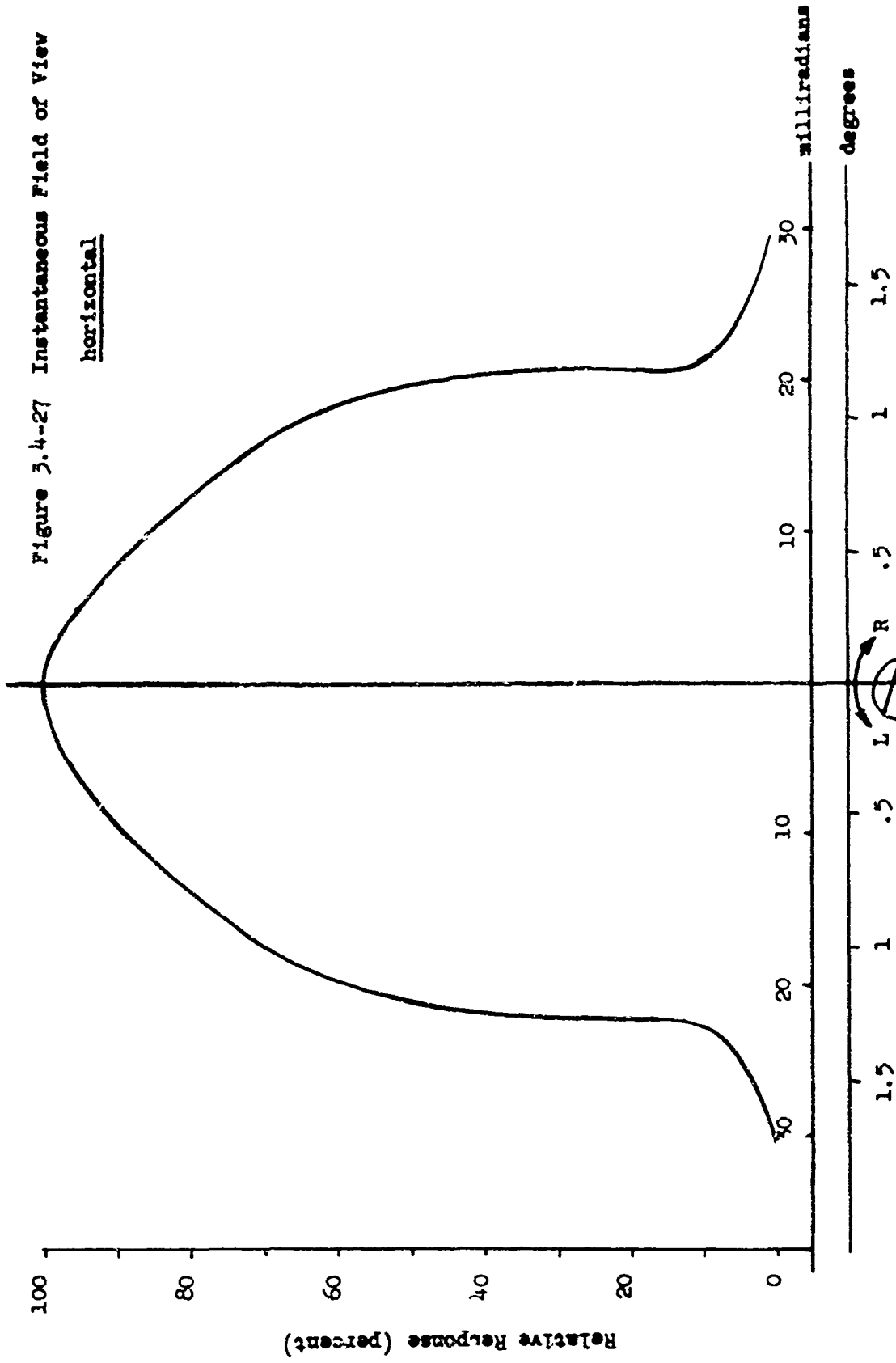




Figure 3.4-28 Instantaneous Field of View

vertical

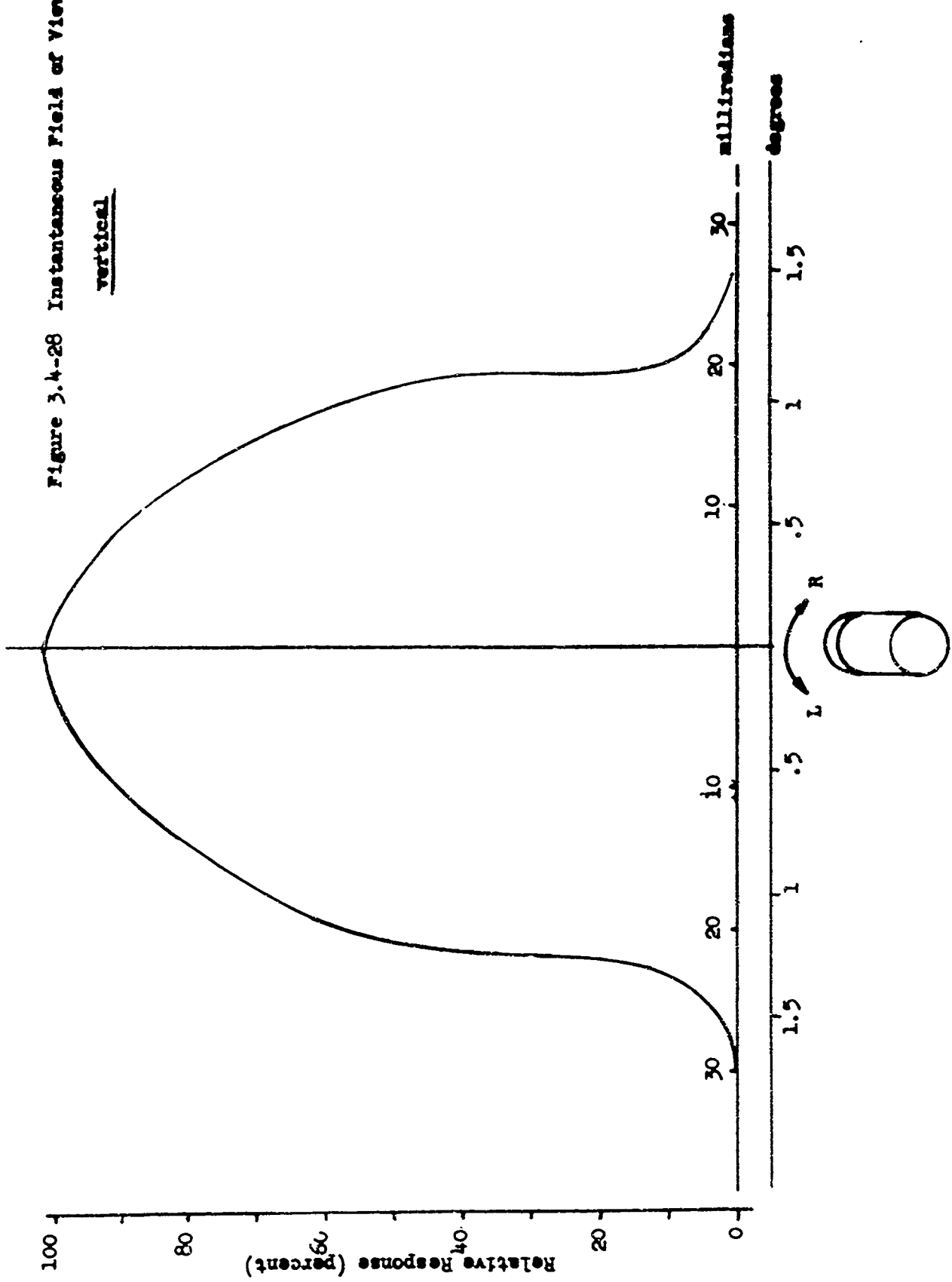
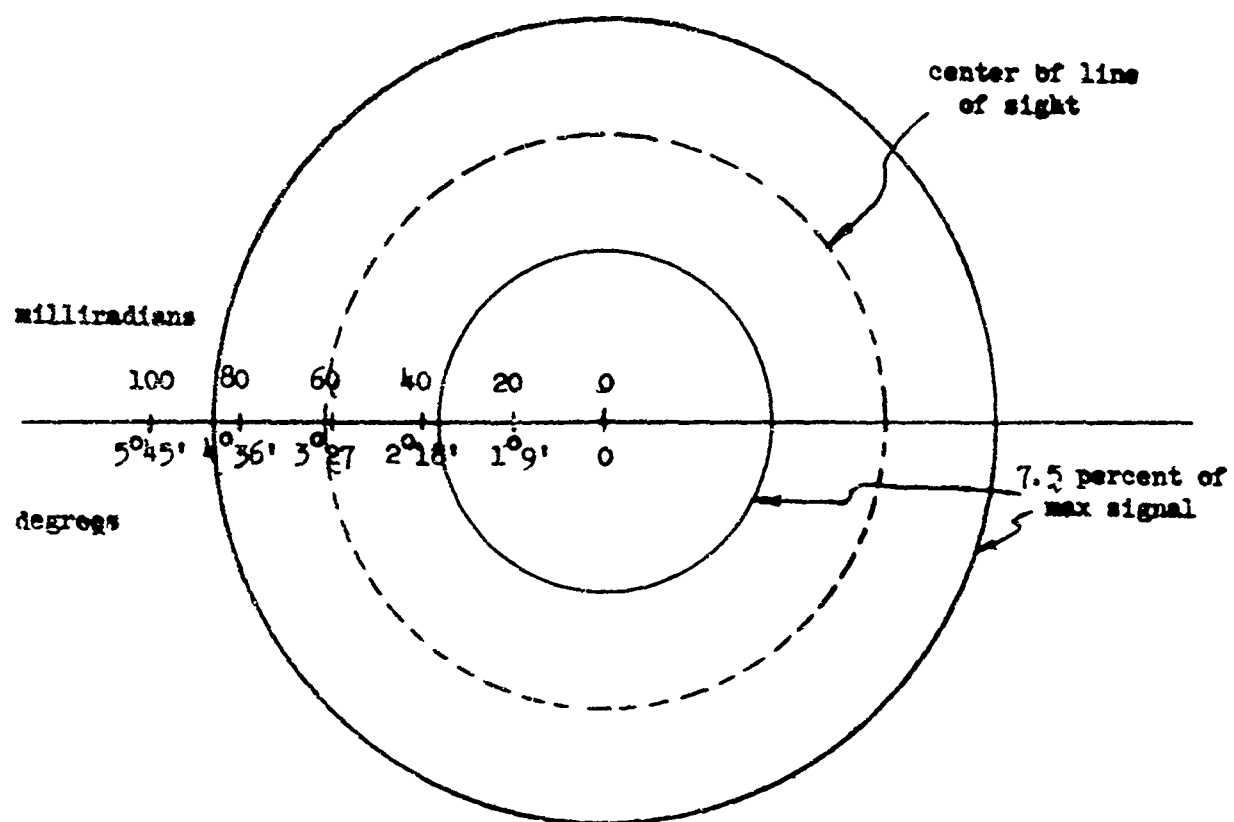

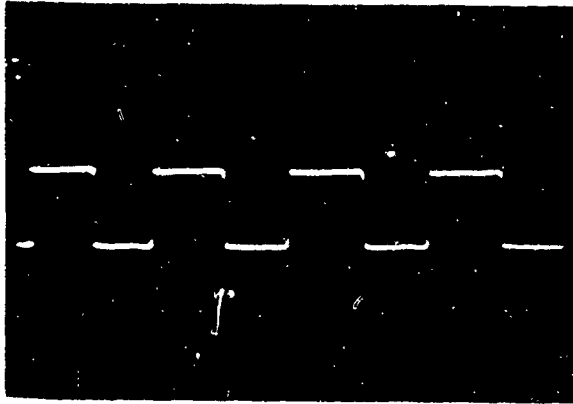


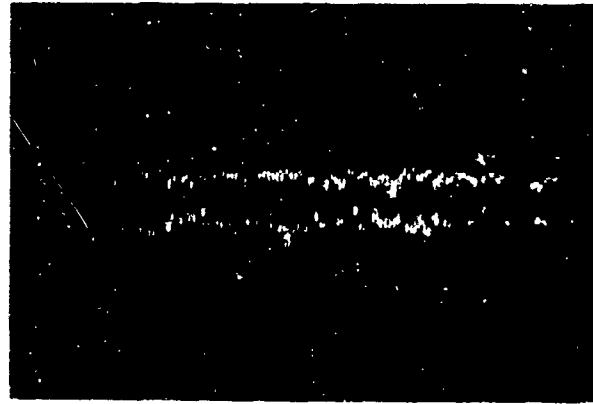
Figure 3.4-29 Scanner Field of View



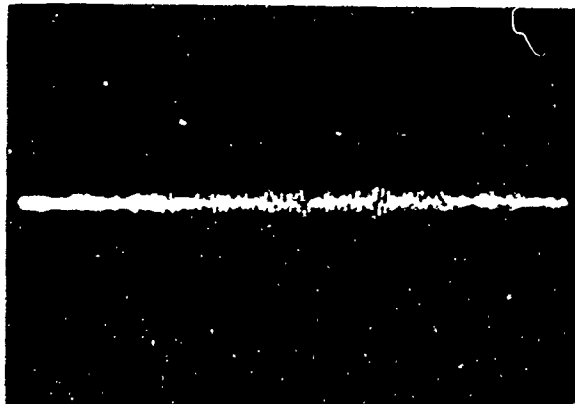
Scale  
  
 20 milliradians



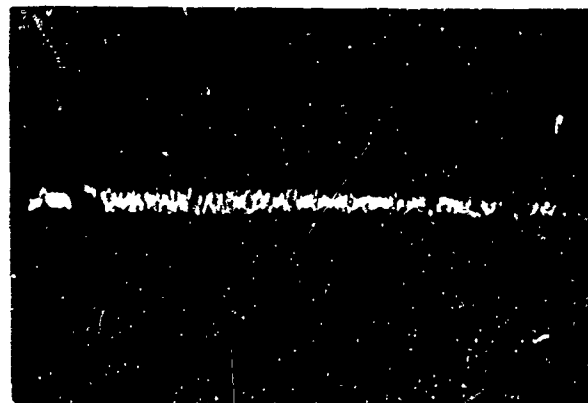
a) calibrate signal - 1 inch = 0.1 volts



b) Maximum Target Signal - no background noise (0.05 volts pk to pk)



c) System Internal Noise (0.02 volts pk to pk)



d) Maximum Background Noise Signal (0.03 volts pk to pk)

Oscilloscope Photos for Signal to Noise Measurement  
Test 6-200, 20

target - receiver distance - 200 ft.  
illuminator spot dia. - 6 ft.  
spin rate 20 rps

Figure 3.4-30. Typical Output Signals



Direction of Scan

Oscillogram of Output of Seeker Signal Amplifier as the line of sight scans past the target

target receiver distance 75 ft; illuminator spot size  
6 ft; spin rate 10 rps  
line of sight angle + 80 mils; (trigger signal coupled  
through the power supply)

Figure 3.4-31. Amplifier Output Signal as LOS Scans Target



#### Guidance References

1. <sup>e</sup>Helstrom, C. W.: Statistical Theory of Signal Detection. Pergamon Press Ltd., London, 1960.
2. <sup>e</sup>Helstrom, C. W.: The Comparison of Digital Communication Systems. IRE Trans on Comm. System. PGCS Vol 8, No. 3, Sept. 1960 141-150.
3. Davenport, W. B. and Root, W. L.: An Introduction to the Theory of Random Signals and Noise. McGraw-Hill, 1958.
4. Neyman, J. and Pearson, E. S.: In the Problem of the Most Efficient Tests of Statistical Hypotheses. Philos. Trans. Roy. Soc. of London, Series A 231, pp 289-337 (1931)
5. Kotelnikov, V. A.: Theory of Optimum Noise Immunity. McGraw-Hill, 1960.
6. Schwartz, M.: Information, Transmission, Modulation and Noise. McGraw-Hill, 1959 - p. 288-291
7. Infrared Industries, Inc.. Technical Bulletin 2.
8. Kruse et al: Elements of Infrared Technology, Generation, Transmission and Detection. John Wiley and Sons, Inc., 1962.
9. Personal Communication: John Bisbee, Infrared Industries, 3/18/64.
10. Tatarski, V. I.: Wave Propagation in a Turbulent Medium. McGraw-Hill, 1961.
11. Stoller, A. P.: Final Report - General Analysis of Infrared Semi-Active Homing Systems for Medium Assault Weapon (MAW) in SECRET Bulova Systems and Instrument Division. Doc #488-002, March, 1964
12. Genoud, R. H.: Statistical Problem in Infrared Search System. Rand Research Memorandum RM-2082. Jan., 1958 CONF
13. Biberman, L. M. and Grove, R.: The Infrared Detection of a Hostile Aircraft Against Terrain Backgrounds. Proc IRIS, vol 3, Sept. 1958 SECRET

14. Elias, Gray and Robinson: IOSA, vol 42, 1952. pp 127-134.
15. Jones, R. C.: New Method of Describing and Measuring the Granularity of Photographic Materials. JOSA, vol. 45, 1955. pp. 799-808.
16. Van Vliet, K. M.: Proc. IRE 46, 1004 (1958).
17. USAF Handbook of Geophysics 1960, Chap 14, 16.
18. Dessens, H. : Annale de Geophysique. 2, 243, 1946.
19. Simpson, G. C.: Quarterly Journal, Royal Meteorological Society 67, 99, 1941.
20. Terminology suggested by IRIS Infrared Background Speciality Group Report - Atmospheric Transmission - Symbols, Units and Nomenclature. June 1963.

#### 4.0 CONCLUSIONS AND RECOMMENDATIONS

A review of this summary report reveals the general level of technology that has been established in each of the critical areas of POLCAT development.

Projectile aerodynamic and structural design has been limited to the problem of converting existing projectiles to the requirements of experimental testing of guidance and control hardware. No serious effort has been made to examine the requirements or the characteristics of an optimum POLCAT airframe suited to tactical requirements.

Results of wind tunnel tests of the test projectile indicate extremely high drag due to bluntness of the nose.

The results of the effort to develop impulse for airframe control have been more substantial. As a result of the design studies and tests that were completed, pulser units capable of delivering 25 lb-sec impulse can be developed in the future. This achievement, however, should be evaluated in light of the impulse required for a tactical system.

The supporting research effort to date has placed great emphasis on the establishment of an understanding of the phenomena associated with semi-active homing as well as developing guidance hardware. There have been significant achievements in this area.

Communication theory techniques to the signal generation and process at the receiver has been applied considering atmospheric effects. For typical optical and scan parameters of the POLCAT seeker, guidance performance was shown to be limited by noise due to scanning the background.

Based on field measurements made with the POLCAT seeker and an



illuminator with a Xenon lamp, the guidance performance against a tank type target is marginal.

The most significant achievement of the program was the successful air gun testing of the POLCAT seeker. These results indicate that the seeker optical-detector design is capable of sustaining the high accelerations of gun launch.

Based on the results of the supporting research program presented herein, the following recommendations for future work are suggested:

- (1) Implementation of the POLCAT concept should be based on the use of a laser illuminator.
- (2) The goal of future pulser development should be the development of units capable of delivering 45 to 55 lb-sec impulse.
- (3) Since the seeker design is capable of sustaining the high accelerations of launch but induces extremely high projectile drag, consideration should be given to obtaining a more suitable design by retaining the basic optical-detector arrangement and reducing aperture to decrease drag.
- (4) A system analysis should be conducted to establish optimum relationships between the various aerodynamic, control, and homing link parameters of a POLCAT system. (Previous analyses of system performance were based on point mass trajectories and did not include the effects of guidance performance.)

Although not directly associated with the supporting research program described herein, an evaluation of the POLCAT concept was made during this period. The evaluation given in "A Study of HAW - Long Range Time Period," BRL MR 1365 by David C. Hardison, considered the application of POLCAT to the requirements of an infantry heavy assault weapon. The results indicated that a POLCAT system was not capable of

fulfilling the specified requirements because (a) overall system weight was too high, (b) time to fire the first round was too long, and (c) the available illuminators did not provide sufficient power. The evaluation did indicate the improvement in performance that could be expected from the development of laser illuminators. Further, the problem of time to fire could be eliminated by utilizing a laser range-finder. However, it is not expected that the weight of a POLCAT system will be substantially reduced in the near future since the major weight penalty lies with the gun tube. Since gun launching is an essential feature of the POLCAT concept, an evaluation of its ultimate worth must consider the trade-off between system weight and system cost. Stringent requirements on system weight can be fulfilled by missile systems but with substantial penalties in cost, complexity, and reliability. The POLCAT concept offers the possibility of providing desired weapon performance (not low weight) for relatively low cost.

# DISTRIBUTION

- |  |  |
|--|--|
| 1 - Commanding Officer<br>U. S. Army Ballistic<br>Research Laboratory<br>Attn: Mr. Chrissman<br>Aberdeen Proving Ground, Md                | 1 - Commanding General<br>U. S. Army Missile Command<br>Redstone Arsenal<br>Attn: Mr. Albert Michetti<br>AMSMI-RFC(CSS)<br>Huntsville, Alabama |
| 1 - Commanding General<br>U. S. Army Weapon Command<br>Rock Island Arsenal<br>Attn: Mr. Biehl<br>AMSWE-RDV<br>Rock Island, Ill.            | 1 - Commanding General<br>U. S. Army Materiel Command<br>Attn: Mobility Branch<br>Washington, D. C. 20315                                      |
| 1 - Commanding General<br>U. S. Army Munitions Command<br>Attn: Mr. Sagarese<br>AMSMU-RE-EG<br>Dover, New Jersey                           | 1 - Attn: Weapons Branch   |
| 1 - Commanding Officer<br>U. S. Army Watervliet Arsenal<br>Attn: Mr. Muzicka<br>Watervliet, New York                                       | 1 - Commanding Officer<br>Harry Diamond Laboratories<br>Washington, D. C. 20438  |
| 1 - Commanding General<br>U. S. Army Tank-Automotive<br>Center<br>Detroit Arsenal<br>Attn: Mr. Wolcott<br>AMCPM-MBT-D5<br>Warren, Michigan | 1 - Commandant<br>Headquarters<br>U. S. Marine Corps<br>Attn: A04F<br>Washington 25, D. C.   |
| 1 - Commanding Officer<br>U. S. Army Munitions Command<br>Picatinny Arsenal<br>Attn: Mr. S. Jacobson<br>Dover, New Jersey                  | 1 - Director<br>Marine Corps Landing Force<br>Development Center<br>Marine Corps Schools<br>Quantico, Virginia                                 |
| 20 - Defense Documentation Center<br>Cameron Station<br>Alexandria, Va.  | 1 - Headquarters<br>Combat Developments Command<br>Fort Belvoir, Va. 22060   |
|  | 1 - USA Artillery CD Agency<br>Fort Sill, Oklahoma 73504   |
|  | 1 - USA Infantry CD Center<br>Fort Benning, Ga. 31905  |

# DISTRIBUTION (Cont'd)

- |  |   |
|--|---|
| 1 - USA Air Defense CD Agency<br>Fort Bliss, Texas   | 1 - Army Research Office<br>3045 Columbia Pike<br>Attn: Mr. Charles Porter<br>Arlington, Va. 22204                                  |
| 1 - USA Armor CD Agency<br>Fort Knox, Kentucky 40121   | 1 - Department of the Air Force<br>Headquarters, U.S.A.F.<br>Washington, D. C. 20330  |
| 1 - USA Combat Developments<br>Experimentation<br>Fort Ord, California   | 1 - Director of Defense Research<br>& Engineering<br>Attn: Mr. Melvin Bell<br>Washington 25, D. C.                                  |
| 1 - Commanding General<br>USA Combined Arms Group<br>Fort Leavenworth, Kansas                                  | 1 - Off. Asst. Secretary Army<br>Research and Development<br>Attn: Mr. C. L. Poor<br>Washington 25, D. C.                           |
| 1 - Director<br>Weapons Systems Evaluation<br>Group<br>Office, Secretary of Defense<br>Washington 25, D. C.    | 1 - Institute for Defense Analysis<br>Research & Engineering Support<br>Division<br>1825 Connecticut Ave<br>Washington, D. C. 20009 |
| 1 - Chief, Bureau of Naval Weapons<br>Department of the Navy<br>Attn: Ad3, Library<br>Washington 25, D. C.     | 1 - Operations Research Office<br>Research Analysis Corp<br>McLean, Va. 22101   |
| 1 - Commander<br>U.S. Naval Ordnance Laboratory<br>Attn: Library<br>White Oak, Silver Spring<br>Maryland 20910 |   |
| 1 - Commander<br>Naval Ordnance Test Station<br>Inyokern, China Lake, Calif                                    |   |
| 1 - U.S. Atomic Energy Commission<br>Sandia Corp<br>Attn: L. Gutierrez<br>Livermore, California                |   |